DAMAGE CHARACTERIZATION OF FIBER REINFORCED COMPOSITE MATERIALS BY MEANS OF MULTIAXIAL TESTING AND DIGITAL IMAGE CORRELATION

by

Joseph Terrance Jette

A thesis submitted in partial fulfillment
of the requirements for the degree

of

Master of Science

in

Mechanical Engineering

MONTANA STATE UNIVERSITY
Bozeman, Montana

August 2017

ACKNOWLEDGEMENTS

There have been many people throughout this process that helped me a great deal. First off, I would like to thank my committee; Dr. Douglas Cairns, Dr. David Miller, and Dr. Michael Edens have been indispensable to my academic success. I would especially like to thank Dr. Douglas Cairns for encouraging me to pursue graduate school, Dr. David Miller for his guidance, and Dr. Michael Edens for countless hours of work in the lab. I would also like to thank Dan Samborsky for his assistance, guidance, and humor that helped me tremendously. I would also like to thank Boeing for their contributions and support of this research.

Many fellow graduate and undergraduate students have also been a tremendous help to me. I would like to highlight Matt Peterson and Tiok Agastra's contributions with finite element modeling in ANSYS. I would also like to acknowledge Mike Voth, Ryan Clarke, Cody Atwood, and Jake Nunemaker for their various contributions and aid.

Finally, I could have never gotten this far without the love and support from family and friends. I would like to thank my mom, my dad, my two sisters, and my lovely wife for their encouragement and support along the way.

TABLE OF CONTENTS

TABLE OF CONTENTS – CONTINUED

LIST OF TABLES

Table Page

LIST OF TABLES – CONTINUED

Table Page

LIST OF FIGURES

Figure Page

LIST OF FIGURES – CONTINUED

Figure Page

LIST OF FIGURES – CONTINUED

Figure Page

LIST OF FIGURES – CONTINUED

Figure Page

LIST OF FIGURES – CONTINUED

Figure Page

ABSTRACT

Composite materials offer a unique quality to improve structural designs. Now, not only can a structure's geometry be designed, composite materials offer the engineer the ability to design the layup of the material and, in turn, control some of its structural properties. While this feature of composite materials is appealing, it also poses issues for all processes involved in its design. One of the primary issues is that characterization of these materials in different orientations is often difficult and expensive. Due to composite materials' anisotropy, heterogeneity, and variability, their constitutive and damage behavior remain poorly understood.

Often due to this misunderstanding, designs that use composite materials undergo a lengthy, difficult, and expensive procedures to produce the final product. Part of these procedures is the finite element modeling and simulation of designed components which requires accurate material response data. As modeling capabilities improve, provided the proper material damage response modeling data, damage models offer the ability to predict the damage response of designs. The ability to accurately predict damage responses in structures is a primary contributor to a design's development time and its overall success.

In this study, multiaxial testing via the Montana State University In-Plane Loader was performed on two carbon fiber epoxy prepreg material systems. This testing was performed to determine the usefulness of digital image correlation and multiaxial testing as a means of characterizing composite materials' damage responses and to produce data capable of informing and validating damage models. The combination of digital image correlation and multiaxial testing provided dense experimental results that may prove useful to qualitatively and quantitatively inform, validate, and enhance computer finite element modeling and analysis.

INTRODUCTION

Introduction to Composite Materials

Materials are a crucial part of any mechanical design. Traditional engineering materials that are well-understood and characterized are carefully sifted through during the design process to ensure the material meets design requirements. Design requirements include properties such as weight-restrictions, stiffness requirements, electrical/ thermal properties, and *especially* material & manufacturing costs. As design requirements are becoming increasingly more stringent, design engineers have more difficulty determining material systems that can meet these strict requirement combinations. Composite materials offer a solution for complex design requirements as their properties can be catered to specific design problems.

Of course, the introduction of a more design-flexible category of materials into the design process is not without its drawbacks. "Composite materials" is a term that encompasses a large range of material systems; however, this document will focus on fiber reinforced polymers (FRPs). FRPs encompasses yet another large range of materials but commonly known types are carbon fiber and fiberglass material systems. Aside from well-known applications such as sporting goods or boat hulls, FRPs are also widely used in both aerospace and wind-energy applications – both of which have been topics of research for the Montana State University's Composite Group and both of which are industries driving research to better understand composites.

A better understanding of composite materials will inevitably push the boundaries of design capabilities, increase performance, and reduce costs. As mentioned above,

composites can be catered to specific applications even on a part-by-part basis. However, a design process seeking the use of composites is inherently more complex as there are several things to consider. Rather than having a design and choosing a suitable material that drives the design geometry, when using a composite material, the design geometry is typically performed in tandem with the design of the material itself. So, although composite materials may produce solutions to some problems their nature inherently complicates the design process. As of now, composites as a whole are not well-understood which can result in over-design, design flaws, and their use can be hinderingly expensive.

Brief History of Composite Materials

Composite materials were beginning to be used as early as the 1940s during an important time for flight technology development. Initial instincts would indicate that high-strength materials were suitable and appropriate for flight components such as wings and rotorcraft blades; however, high-strength materials are typically also brittle. This required an innovation to mix properties of both high-strength and ductile materials. Glass fibers were prevalent during the time as they were being produced in the early 1930s by Owens-Corning and were an ideal choice to be used as the 'high-strength component'. Engineers came to realize that immersing chopped glass fibers in a low-strength polymer resulted in a stronger, stiffer, and lighter-weight polymer-like material [1].

Not long after their introduction, industry began producing and using composites in many different fields. Still in the 1940's the U.S. Navy took advantage of the fiberglass reinforced polymers' (GFRPs) electrical insulation properties for their terminal boards; and the Wright-Patterson Air Force Base launched exploratory projects to begin using these

materials in structural aircraft parts. Not long after research began, in 1946 the first plane with GFRP structural components (the Vultee BT-15) made its first flight [2]. In later years, research and development teams have pushed composite materials farther which resulted in high-performance materials.

In 1957, the Soviet Union successfully launched the Sputnik I satellite and spurred on the space race. Of course, a necessity of such an endeavor is even lighter, stronger materials than GFRPs. Asbestos fibers, phenolic resins, metal matrix composites, carbon/graphite fibers, boron fibers, and other systems were all being developed and used during this time as a means of solving the unique problems posed by the exit and reentrance from a lunar mission. The space race changed everything from politics, economics, and of course engineering problems. The National Aeronautics and Space Administration (NASA) was founded in 1958 and NASA is still at the forefront of not only space travel but engineering innovations such as composite materials and their applications.

Since the space race and space era, the industrialization and commercialization of composite materials has grown immensely. Now, composite materials can be found in nearly everything, from consumer products like golf clubs and tennis rackets to passenger airplanes and spacefaring devices & vehicles. Again, industries like aerospace are pushing research and development to better understand composite materials so that their use in design is appropriate. A better understanding of the materials themselves can assure higher performance, less expensive, and safer designs. To better understand materials, their properties must be measured and understood – not only engineering properties such as moduli and density but their damage characteristics as well.

Composite Material Characterization

It is prudent to define "composite materials" further before continuing. It has already been stated that this document will focus on FRPs which already suggests a mixture somehow between fibers and polymers. A generally accepted definition of "composite material" is a combination of two or more distinct materials to form a new material with enhanced properties [3]. It is also important, from a fundamental standpoint, to know that the combination of distinct materials mentioned above is on the macro-scale and not the micro-scale. This means that the mixture of materials is the mixture of 'larger' structures and not on a molecular level; typically, alloys are not considered composites. Composites are non-homogeneous (heterogeneous) materials.

Knowing this, it can be easily seen how complex the characterization of these materials can be. Traditional engineering materials such as metals have been studied and characterized in depth, some of which for thousands of years. Only in the past approximately 70 years have composites been studied, and herein lies the first difficulty. It is difficult to understand much about a material that is still in its infancy, they have simply not existed long enough. However, the youth of the material isn't even the largest concern.

Of course, just because the material is relatively new compared to traditional engineering materials (e.g. metals) doesn't mean that previous gained knowledge, methods, and technology do not apply to it. However, when applying knowledge such as mechanics of materials and fracture mechanics to metals, it is seemingly infinitely easier than doing so for composites. Metals are expected to behave a certain way under given conditions and variations can be intuitively, analytically, and experimentally rectified. Composites, on the other hand, are not so simple nor easily understood; they pose unique difficulties in

each of those categories: intuitively, analytically, and experimentally. As such, now and over the past 70 years, the effort to better understand composites is a necessity for their use in many design situations.

Materials are characterized by performing several series of tests to obtain pertinent material information. This characterization of the material is then used in the design process for material selection. Typically, when well-understood materials e.g. steels or aluminum alloys are used in a design, the design process is fast and the properties obtained from previous tests applies directly to the final manufactured part. This allows the designer to use analytical and experimental methods to validate the design. However, the use of composites as mentioned above, is much more complex as the material is typically designed in tandem with part geometry. Since the bulk material is being designed with the part, the design process is much slower and far more expensive. MIL-HDBK-17 is a guidance document prepared for departments and agencies of the U.S. Department of Defense which eloquently states:

> "Analysis alone is generally not considered adequate for substantiation of composite structural designs. Instead, the 'building-block approach' to design development testing is used in concert with analysis. This approach is often considered essential to the qualification/certification of composite structures due to the sensitivity of composites to out-of-plane loads, the multiplicity of composite failure modes and the lack of standard analytical methods." [4]

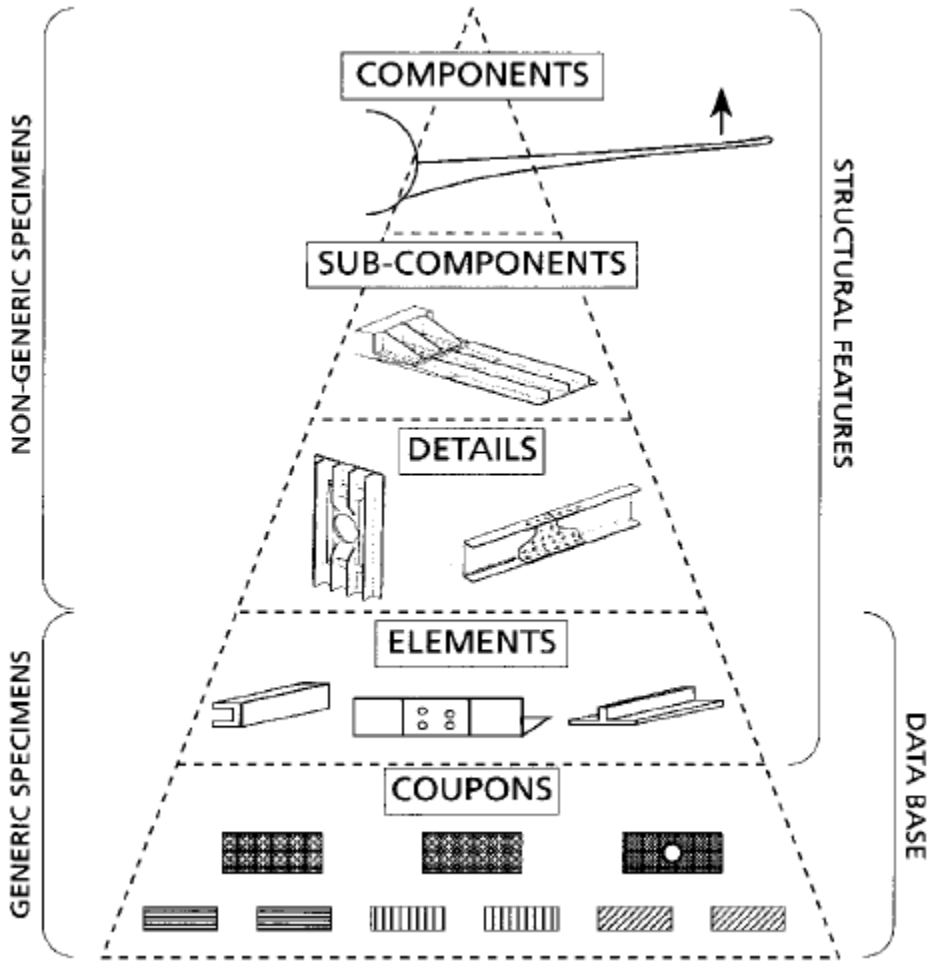

Figure 1. The "building-block approach" schematic as shown in MIL-HDBK-17-1F [4]

The schematic from Figure 1 (above) depicts the complexity of designing especially large components using composites. Not only are tests necessary on the coupon level, the design cannot be validated without substantially more tests up to and including the final component. As knowledge of composite materials is increased, more data from the least expensive (coupons) level can be used while mitigating the expense of component and sub-component tests to validate designs. Furthermore, MIL-HDBK-17 also mentions the complexity of damage in composites as a hindrance to design validation.

Damage and Failure in Composite Materials

During WWII and the space era, a need to better understand material failure drove research further. These research efforts were accelerated during the time that passenger planes, such as the de Havilland Comet, became a growing market and necessitated a better understanding of fatigue-induced damage [5]. Out of the research efforts to understand damage, academic areas like *fracture mechanics* emerged as a means of explaining material damage and failure. Fracture resistance is typically measured in terms of a fracture toughness value (K) or a strain-energy release rate (G_C) for a material. Both ideas originate from the same principles and result in accurate methods of determining damage and failure analytically for traditional homogeneous engineering materials such as steels. However, when applied to composites, these methods become multiplicatively more difficult to apply due to the nature of composite materials.

The heterogeneous nature of composite materials inherently complicates how damage initiates and propagates through the material. Damage is no longer characterized simply as a crack that grows but can consist of many mechanisms. Damage can initiate and progress through a minimum of three unique mediums of the material – the fibers, matrix, and fiber-matrix interface. Figure 2 below depicts some intra-ply damage mechanisms that can occur within a lamina. Already, within only one ply, there are many types of damage that can occur within a composite material during the damage process. However, this does not account for damage that can occur through the thickness of the laminate or inter-ply damage such as delamination of neighboring plies. Although typically not all of these damage modes occur at the same time, their mere existence complicates efforts to understand, model, analyze, and even evaluate damage in composite materials.

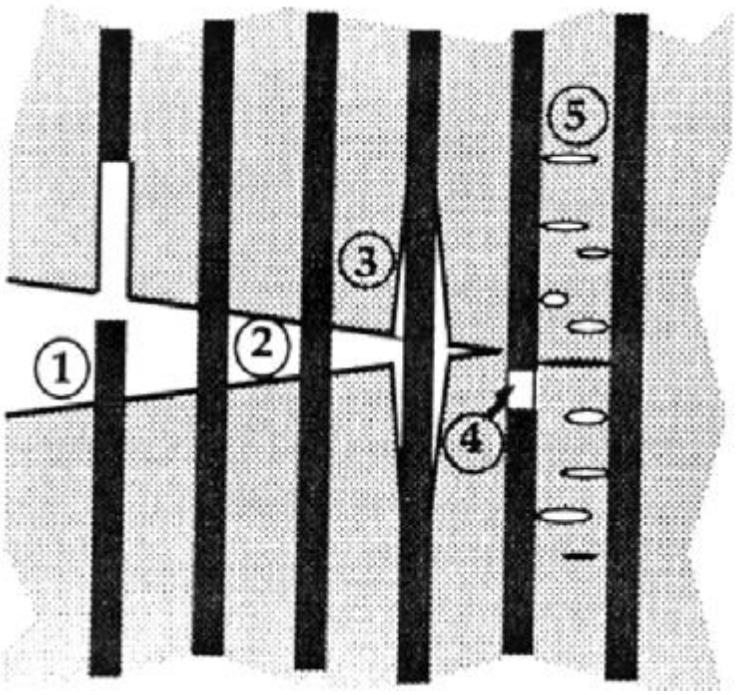

Figure 2. Intra-ply damages in a composite material (by Anderson [6]). (1) Fiber Pull-out. (2) Fiber Bridging. (3) Debonding. (4) Fiber Breakage / Rupture. (5) Matrix Plasticity & Cracking

Even while considering a composite's heterogeneity and some of its damage mechanisms, this simply does not and cannot account for all variables that affect the damage of a composite material. More variables affecting composite materials' damage characteristics include topics such as fiber misalignment & waviness, matrix porosity, creep behavior, moisture content, and many other defects and factors. This complexity necessitates more general methods of investigating damage in composites rather than attempting to completely understand each contributing factor fully; some of these methods include a variety of statistical analyses, energy methods, and even educated guess & check.

It is important to note that damage is not necessarily synonymous with failure and that failure is defined by the application of the material. When a structural member no

longer has the capacity to perform its intended design that member is said to be failed; this allows, in most designs, a degree of damage to accumulate in a component before failure. Certainly, damage and failure are related, but their relation is determined by the design engineer. This further demonstrates the necessity of understanding damage in composite materials – at some point, damage accumulation will cause failure and a better understanding of damage can not only lead to the mitigation of damage by means of better designs but also better damage-tolerant designs*.

Motivation

After being introduced to the complexities of composite materials, it is evident that a better understanding of composites is needed to streamline the design process and produce better designs. Typically, in the design process, finite element models are used to simulate design responses to its application loads and displacements. This mitigates the need for building expensive prototypes and test objects for the validation of a design. Finite element models are improving to the point of predicting damage but are still generally unrepresentative due to the lack of proper damage characterization of the materials and the complexity of the models. This study aims to produce data capable of informing and validating these damage models so that the development and application of damage models is more representative of the final design. If damage models can more accurately predict damage, their use in the design process may reduce design time, design expenses, and ultimately improve the final design.

* Damage Tolerant Designs account for development of damage primarily due to fatigue and ensure, using specific inspection intervals, safe operation up to *at least* the next appointed inspection interval.

THE MONTANA STATE UNIVERISTY IN-PLANE LOADER

The Montana State University In-Plane Loader will be referred to as the "IPL" from this point on. There are many previous theses (to be discussed further later) that sum up the previous works with the IPL. However, for the sake of completeness and to provide information on the current state of the IPL, this chapter will introduce the purpose, conception, previous work, recent changes, and current work with the IPL.

Multiaxial Testing

This section will discuss, in brief, why multiaxial testing can be a powerful asset in the understanding and characterization of composite materials and will ultimately discuss the purpose of the IPL. As mentioned above, materials undergo several series of tests to determine pertinent engineering properties necessary for informed and efficient design. For isotropic materials[†], these tests are not direction-dependent and can therefore be characterized fully without having to account for material orientation. The anisotropy and heterogeneity of composite materials dictates that their characterization undergoes a much more rigorous process accounting for properties in all relevant directions. This can be seen by considering even a single unidirectional ply (or lamina) and even more so with materials involving stacks of plies (or laminates).

Traditional testing such as those performed with uniaxial testing machines can supply information typically in a single direction by means of uniaxial testing. In contrast

[†] Isotropic materials – Materials where the elastic properties are the same in all directions [10]. Traditional engineering materials such as metals are often idealized and treated as isotropic materials.

to composites, isotropic materials have infinitely many planes of material property symmetry, allowing properties to be applied to all directions of the material where few tests can fully characterize the material. This not only applies to properties such as moduli ($E\ or\ G$), but also failure properties such as fracture toughness (K) as mentioned above. However, these uniaxial tests are not sufficient to fully characterize composite materials' stiffness properties and especially failure/strength properties. As a means of justifying the use of multiaxial testing, the examination of both elastic theory and failure theory can be examined individually. However, for the sake of brevity, only failure theory will be explained in depth as it pertains more to this thesis. Before continuing though, it is necessary to explain, on a basic level, elasticity of anisotropic materials.

$$\{\varepsilon\} = [S]\{\sigma\} \tag{1}$$

In general, Hooke's Law states that stress is proportional to strain based on the elastic properties of the material as shown in Equation (1) above. This relationship is typically expressed more simply for isotropic materials where only three elastic constants (E, ν, G) are needed to fully describe the material's elasticity. However, for an anisotropic material with no symmetry whatsoever, the compliance matrix $[S]$ is expressed as a matrix with 81 independent terms. This is then reduced, using material symmetries and other assumptions to produce a more manageable relationship. This resolution for composite laminae is generally expressed in its simplest form as Equation (2) below, where assumptions such as transverse isotropy and plane stress are applied [3].

$$\begin{Bmatrix} \varepsilon_1 \\ \varepsilon_2 \\ \gamma_6 \end{Bmatrix} = \begin{bmatrix} 1/E_1 & -\nu_{21}/E_2 & 0 \\ -\nu_{12}/E_1 & 1/E_2 & 0 \\ 0 & 0 & 1/G_{12} \end{bmatrix} \begin{Bmatrix} \sigma_1 \\ \sigma_2 \\ \sigma_6 \end{Bmatrix} \tag{2}$$

From Equation (2), there exist different properties in different directions for anisotropic materials where subscripts 1, 2, and 6 (also expressed as 12) correspond to the material local coordinates fiber-direction, transverse-direction, and shear on the 1-2 plane respectively. This notation will be used in the following section to express failure criterion.

Failure and Strength of Composites

As discussed above and shown in Figure 2, failure in composites is complex and for this reason, there exists an area dedicated to understanding failure/strength of composites. Generally, there exists three types of failure criterion applied to anisotropic materials namely composites: Maximum Stress Criterion, Maximum Strain Criterion, and Interacting Criteria, the latter of which justifying the use of multiaxial testing. Each of these criteria attempt to predict failure of composites by a means of simple calculations for use during design and analysis. Failure criteria attempt to calculate the limit of a material before its mechanical properties begin to change. These criteria do not attempt to account for physical damage to the material such as microscopic cracking etc. until the coalescence of this physical damage results in material property change (mechanical damage).

It is important to note that the failure criterion introduced in this section have been developed from mature and well-understood principles in mechanics. However, no matter how mature, any failure criterion (even criterion not explicitly stated in this thesis) developed to date has its own pros and cons. This can be demonstrated by the World-Wide Failure Exercises (I & II) [7].

The exercise was the work of several experts to determine the accuracy and validity of 12 different failure criteria. Christensen [8] summarizes the work of the exercise well

in stating that there are very large variabilities in both the failure criteria and the material samples. Many of these failure criteria differ greatly from one another but, for different instances, well-represent experimental data. The true outcome of the exercise was that there exist no reliable failure criteria for fiber reinforced composite materials that are consistently accurate.

Maximum Stress Criterion. Maximum Stress Criterion is expressed by a series of inequalities defining limits on the stress of the material. These strength limits are defined by experiments in both the fiber or 1 direction, and the transverse or 2 direction for both tension and compression cases as well as for shear or 6 deformation.

$$\begin{array}{rll} \sigma_1 > F_{1t} & if & \sigma_1 > 0 \\ |\sigma_1| > F_{1c} & if & \sigma_1 < 0 \\ \sigma_2 > F_{2t} & if & \sigma_2 > 0 \\ |\sigma_2| > F_{2c} & if & \sigma_2 < 0 \\ |\sigma_6| > F_6 & & \end{array} \tag{3}$$

The inequality expressions are shown in Equation (3) above and state that failure of a lamina is predicted when at least one of the stress (σ) in the material coordinates exceeds the corresponding experimental value of strength (F) [3]. Also, as stated by Barbero [3], this criterion proves useful in that it gives information regarding the mode of failure. However, a drawback of this criterion is that it does not provide interaction between stress states and therefore is not conservative for stress states that are not dominated by one component of stress. This criterion is most effective where a single component of stress dominates the stress state of the material.

Maximum Strain Criterion. Maximum Strain Criterion is similar to Maximum Stress Criterion except the limits are no longer stress values but strain values (strain to failure). Again, these limits are defined by experiments in both the fiber direction (1) and the transverse direction (2) for both tension and compression cases as well as for shear (6). This criterion uses the concept of strength ratios and the criterion is shown in Equation (4) below.

$$\begin{array}{ll} R_1 = \varepsilon_{1t}/\varepsilon_1 & if \quad \varepsilon_1 > 0 \\ R_1 = -\varepsilon_{1c}/\varepsilon_1 & if \quad \varepsilon_1 < 0 \\ R_2 = \varepsilon_{2t}/\varepsilon_2 & if \quad \varepsilon_2 > 0 \\ R_2 = -\varepsilon_{2c}/\varepsilon_2 & if \quad \varepsilon_2 < 0 \\ R_6 = \gamma_{6u}/|\varepsilon_6| & \end{array} \tag{4}$$

This criterion states that failure is predicted when at least one of the strain values reaches the experimental strain limit values or when a strength ratio (R) meets or exceeds a value of 1. This criterion is the most popular failure criterion used in industry today per Barbero [3]. This is likely due to the ability to directly measure strain in tests unlike the Maximum Stress Criterion where stress must be computed and, for this reason, may be less reliable. An inherent usefulness of this criterion is that Poisson Effects are included – something Maximum Stress Criterion fails to account for. Also, like Maximum Stress Criterion, Maximum Strain Criterion provides information regarding the mode of failure.

Interacting Criterion. There are several different well-accepted models that fall under interacting criteria as a category. Tsai-Wu is a popular criterion heavily used for polymer matrix composites. Tsai-Hill is often applied to special cases of FRP analysis or materials like ceramic and metal matrix composites. The basis behind all *interacting criteria* is that they account for the *interaction* between different failure modes which the

previously mentioned criteria fail to include. This is more realistic as many modes of failure are not physically justified to be independent from one another. However, to be addressed later, quadratic failure criteria such as Tsai-Wu and Tsai-Hill also pose problems of their own.

The previously discussed criteria (Maximum Stress & Strain) assume that a multiaxial state of stress can be represented as a series of uniaxial states that are independent from one another. If any of the uncoupled, uniaxial states exceed their corresponding strength values, then the material is determined to have failed. For a multiaxial case, the fact that the material is being subjected to combined stresses is ignored. So, when two or more failure modes interact to produce failure, the Max Stress & Strain criteria may result in unrepresentative predictions and ultimately unconservative or over-conservative designs. These interactions can be intuitively seen and further demonstrated by looking at some cases that Barbero [3] describes:

- Transverse tensile $\sigma_2 > 0$ and shear stress σ_6. In this case, both stress states can produce the same type of damage (matrix cracking) and therefore interact with one another detrimentally.
- Transverse compressive $\sigma_2 > 0$ and shear stress σ_6. In this case, interaction is opposite from the previous. Rather than negatively affecting the material, these states of stress oppose one another. Cracks in the matrix produced by shear must overcome the transverse compression stress to propagate in the material.

- Longitudinal compressive $\sigma_1 < 0$ and shear stress σ_6. This case can be detrimental to the material as the shear stress can produce damage and effectively reduce shear modulus G_{12} which, in turn, reduces the longitudinal compressive strength.

Even though interacting criteria attempt to reconcile this interaction between stresses, there are drawbacks to this category of failure criteria [3]. First, many interacting criteria, including Tsai-Wu and Tsai-Hill, force an artificial interaction between matrix and fiber modes of failure. Second, interacting criteria usually do not provide information regarding the mode of failure (matrix or fiber). An example of an interacting criteria, posed by Barbero, is displayed in Equation (5) below.

$$\langle \sigma_1^f / F_{1t} \rangle + \langle -\sigma_1^f / F_{1c} \rangle - 1 = 0$$

$$f_{22}\left(\sigma_2^f\right)^2 + f_{44}\left(\sigma_4^f\right)^2 + f_{55}\left(\sigma_5^f\right)^2 + f_{66}\left(\sigma_6^f\right)^2 + f_2\left(\sigma_2^f\right)^2 - 1 = 0$$

$$f_2 = \frac{1}{F_{2t}} + \frac{1}{F_{2c}} \tag{5}$$

$$f_{22} = \frac{1}{F_{2t}F_{2c}} \;\; ; \;\; f_{66} = \frac{1}{(F_6)^2}$$

$$f_{44} = \frac{1}{(F_4)^2} \;\; ; \;\; f_{55} = \frac{1}{(F_5)^2}$$

Finally, as a result of examining failure criteria, it is evident that the world of composites is in need of a well-informed and reliable failure criterion for fiber reinforced materials. Also, to obtain this criterion, the interaction between stresses must be considered. These interactions must be validated and informed by experimental data and herein lies the purpose and endorsement of multiaxial testing.

Brief History of the IPL

Inspired by work from the Naval Research Laboratory (NRL) [9], the IPL was conceived in 2001 as a senior design project for mechanical engineering undergraduates Eric Booth, Ken Higgins, and Marc Schaff [10]. The first-generation IPL was then fully completed later by several graduate and undergraduate students. Since the first-generation, the IPL has undergone many renovations and been the primary topic of several Master's theses. Each generation of the IPL has improved the hardware, software, and instrumentation reliability of the machine.

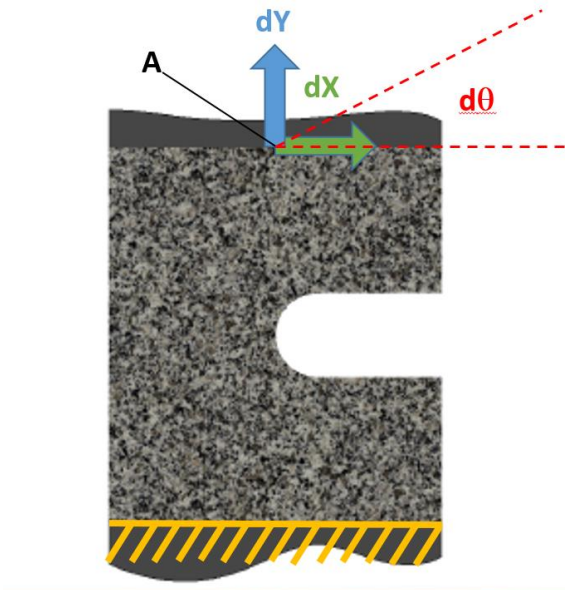

Figure 3. Schematic of possible deformations applied to a coupon in the IPL

The first-generation IPL was laid horizontal on a table as seen in Figure 4. The design utilizes three strategically placed stepper motor-driven ball-screw actuators to deliver displacements and loads to the sample. The actuator configuration allows two

translational components (dx and dy) and a rotational component ($d\theta$) shown above in Figure 3 (this will be discussed further later) to be applied to the sample without the machine binding against itself. Pancake load cells were installed at the end of each actuator to accurately measure each supplied load. Instrumentation and control of the IPL was performed in LabVIEW, Mathematica, and MATLAB software packages [11]. As stated above, this original design has been upgraded several times resulting in the current 'fifth-generation IPL' shown in Figure 5.

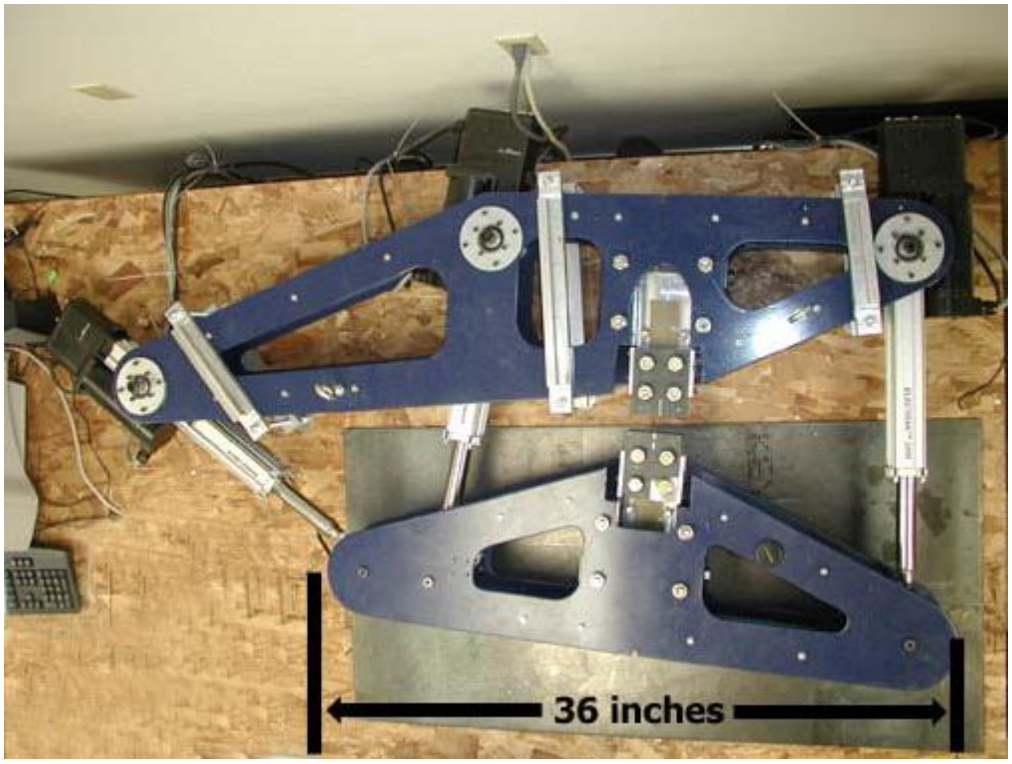

Figure 4. A photograph of the first-generation IPL as shown in Ritter's thesis [12]

Third Generation

The third-generation IPL contributed primarily to Smith's thesis [13]. Improvements made from the first and second generation IPL in this iteration were drastic.

Both Smith and Schmitt [14] summarize the changes made to the IPL in great depth. For completeness, the primary contributions to this generation of IPL are listed below.

- LVDT Position Control – The first-generation IPL relied on encoders in each actuator to control position of the cross-head. This was then changed to be controlled by LVDT's mounted directly to the grips. Schmitt [14] describes the LVDT array used.
- New Gripping Mechanism – The first-generation IPL used knurled grip plates mounted in an assembly which required bolts to clamp the sample. This grip assembly was then replaced by an assembly using hydraulic pistons driving self-centering carbide-textured grip plates to clamp samples in place.
- Upright Mounting – The horizontal configuration of the first-generation IPL proved to be cumbersome when using the new gripping mechanism. Thus, a stand was built to hold the IPL upright so that each side of the grips could be easily accessed.
- Out-of-Plane Constrainer – A bearing plate was mounted directly to one end of each grip half to reduce out-of-plane response during testing. Out-of-plane response occurred when loading a sample due to compliance of the machine itself and off-axis loading of the coupon. This addition was an attempt to mitigate any contribution of out-of-plane displacements applied to the coupon.

This concludes the primary changes made since the first-generation IPL. However, see previous works for a more complete list of changes and Collett [11] for a validation study of the third-generation IPL.

Fourth Generation

As stated in Schmitt's thesis [14], the fourth-generation IPL did not undergo any large changes to mechanical components or software of the system but only the addition of a digital camera to monitor the distortion of the coupon mid-test. This camera system, run via MATLAB, is a digital image correlation (DIC) system designed and implemented by Parker [15]. Since Parker's DIC implementation in 2009, Montana State University has purchased a commercial DIC system to replace Parker's. The commercial DIC used for this research is called GOM ARAMIS. The purpose and application of DIC as it pertains to this research will be thoroughly explained later; for technical inquiries about DIC and its development, refer to Parker [15].

Fifth Generation

The most current generation of the IPL utilizes most of the same components as shown in Figure 4. The ball-screw actuators, pancake load cells, and frame have been changed little since the original design. Even as such, the most current fifth-generation IPL shown in Figure 5 has been the largest redesign of the IPL. Many of the recommendations from previous research were taken into account to improve the reliability and performance of the IPL. The primary concerns and design goals addressed in the redesign were:

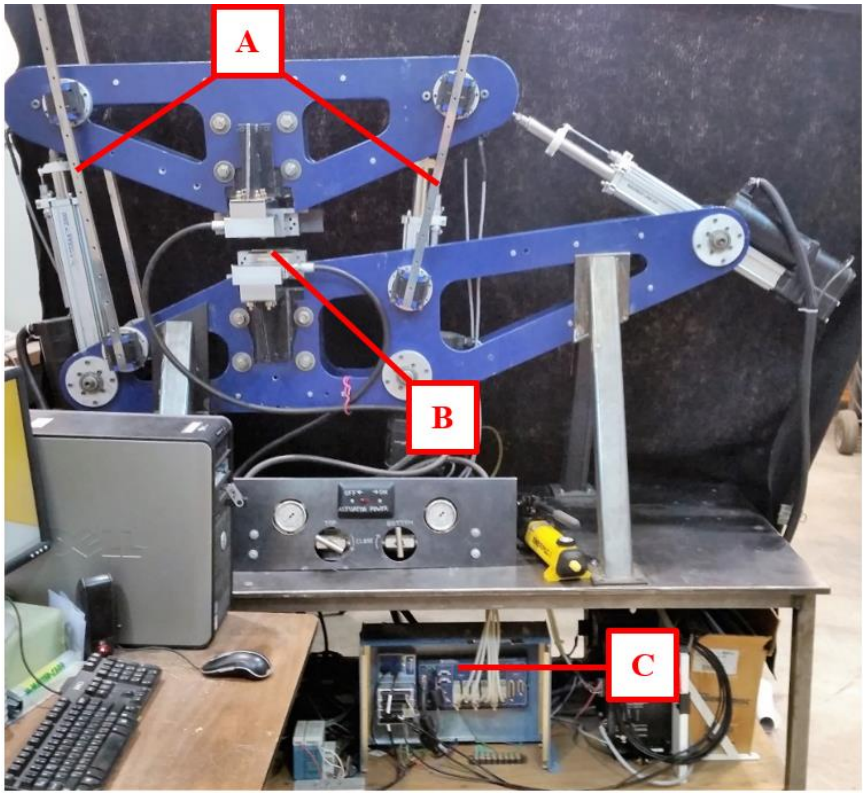

Figure 5. Fifth-generation Montana State University In-Plane Loader. A: Out-of-plane Constrainers (both sides) B: Coupon Loading Location C: Main Electronics

- Coupon Slippage – Slippage of the coupon in the grips during testing (also refered to as grip slippage) remained a problem even after the implementation of the third-generation grip assembly.
- Out-of-plane displacement – Again, even though the out-of-plane constrainer was employed to mitigate this problem, out-of-plane displacement remained an issue during testing. Out-of-plane displacements typically occurred due to high loads especially during damage of the coupon.
- Software Issues – The third-generation IPL employed new position-control code run in LabVIEW that ultimately caused issues due to noise in the LVDT readings and control code feedback loop inefficiencies. The most noteable effect of these

inefficiencies was inconsistent loading during testing (rapid, jerky displacements provided by the actuators).

- GOM ARAMIS Implementation – The implementation of GOM ARAMIS DIC as the primary data acquisition system for both loads and displacment data during testing. Ideally, optical measurement systems such as DIC should be used to control the IPL (see recommendations), but DIC at this point was implemented as data acquisition only.

The resolution of these issues required several hardware changes to be made on the IPL including a new grip assembly, new out-of-plane constrainers, and new electronics. Included with these hardware changes, an entirely new version of IPL control code was written. These changes and a description of the current state of the IPL are discussed below.

A solid model of the fifth generation grip assembly can be seen in Figure 6. The latest grip design was made to grip the coupon not only on the faces but also the edges using the transverse support plates ('C' in Figure 6). These transverse support plates supply little, if any, load to the sides of the coupons and are meant only to restrict coupon movement in the grips during rotations and x-displacements. The grips are still driven closed using the same hydraulic piston (A in Figure 6) supplying a load up to $7800\ lbf$ to the coupon. The new grip plates ('B' in Figure 6) have the same carbide coating applied to the surface but now over a larger effective grip area ($2\ in \times 2\ in$). The new grips no longer have a self-centering mechanism and must be shimmed to maintain in-plane loading. Finally, these grips can support coupons up to $0.5\ in$ thick and $2\ in$ wide which is an

improvement over previous grips. The thinnest allowable coupon with the use of the transverse support plates is $0.125\ in$.

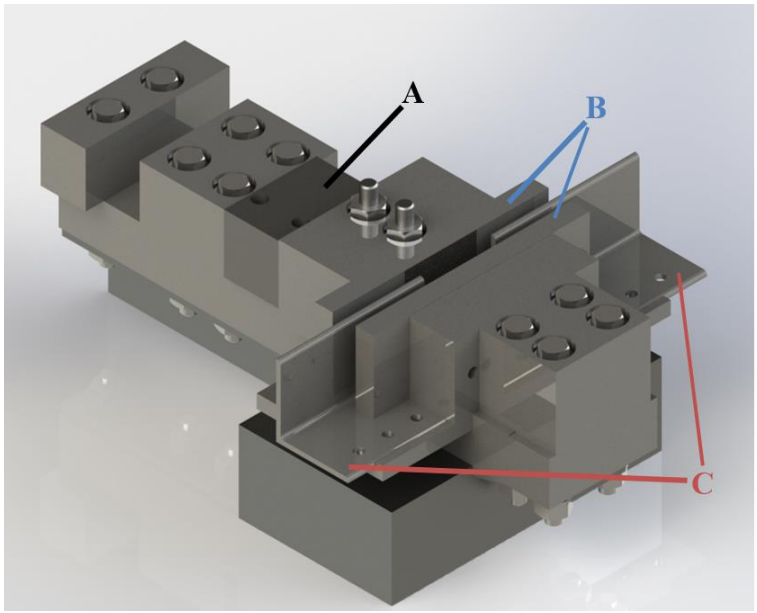

Figure 6. Solid model rendering of the fifth-generation IPL grip assembly. A: Hydraulic Piston B: Carbide-textured Grip Plates C: Transverse Support Plates

The new out-of-plane constrainers are shown as 'A' in Figure 5. Each of the 4 out-of-plane constrainers is made from 2 slewing bearings, 2 linear bearing carriages, and a linear bearing rail. A slewing bearing is mounted directly to the frame (both the base and the cross-head) with a linear bearing carriage mounted directly on top of it. The linear bearing rail then connects the upper and lower assembly and is only allowed to slide in the top assembly. The slewing/ linear bearing configuration allows for translational and rotational displacements in-plane but restricts any out-of-plane displacements of the cross-head. For future modifications, the linear bearing rails were designed so that supports may be mounted to them to supply more rigidity if necessary.

The latest electronic hardware is shown as ‘C’ in Figure 5. These new components consist of an up-to-date data acquisition (DAQ) module and actuator control module. These components bridge the connection between the latest IPL control software and its electrical components. The DAQ serves to gather load cell and LVDT voltages as well as supplying voltages (voltage output) for resolved loads to the ARAMIS DIC. The actuator control module serves as the interface between LabVIEW software and the actuator motor drives.

The latest IPL control software is written using the same basic control scheme by means of a kinematic vector loop solution. The original vector schematic has been updated to follow the schematic shown below in Figure 7 where vector ‘k’ is computed and controlled by changing actuator lengths ‘$L1$’, ‘$L2$’, and ‘$L3$’. Figure 7 depicts vectors that can be controlled as blue and uncontrollable vectors as red. Vector ‘k’ is the gap between the bottom and top grips and controlling this displacement controls the deformation of a sample when loaded in the grips

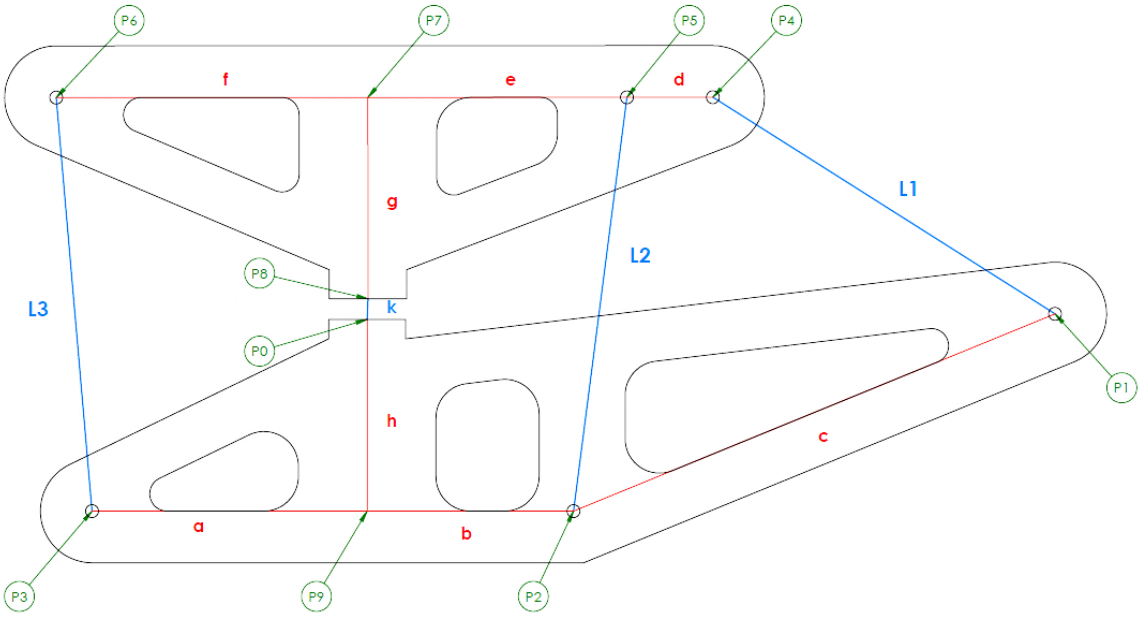

Figure 7. Latest vector loop schematic and nomenclature as used for IPL control software

Aside from a more efficient control scheme, there are two notable changes made to the IPL. First, the LVDT array for position control of the crosshead has been removed and the LVDTs have been repurposed as calibration aids for accurately determining '$L1$', '$L2$', and '$L3$' at any given time. The position control is now based on encoder readouts in the actuators rather than using the LVDT array. This decision was made for several reasons but was mostly due to LVDT noise errors that came from measuring miniscule displacements close to the grips. Second, the new DAQ allowed for resolved load output as voltages to the ARAMIS. This allows the ARAMIS software to be used for all data acquisition from the IPL including optical displacement measurements and load data.

Application of the IPL

Dissipated Energy Density

Introduced with the idea of an In-Plane Loader, dissipated energy density was formally introduced by the NRL in 1995 as a means of quantifying damage in composite materials undergoing multiaxial loading conditions. The full scheme for using dissipated energy density to quantify damage can be seen in the NRL's published paper [9] Ritter's thesis [12], and Schmitt's thesis [14]. The basics of the scheme and the application as it pertains to this research are discussed below.

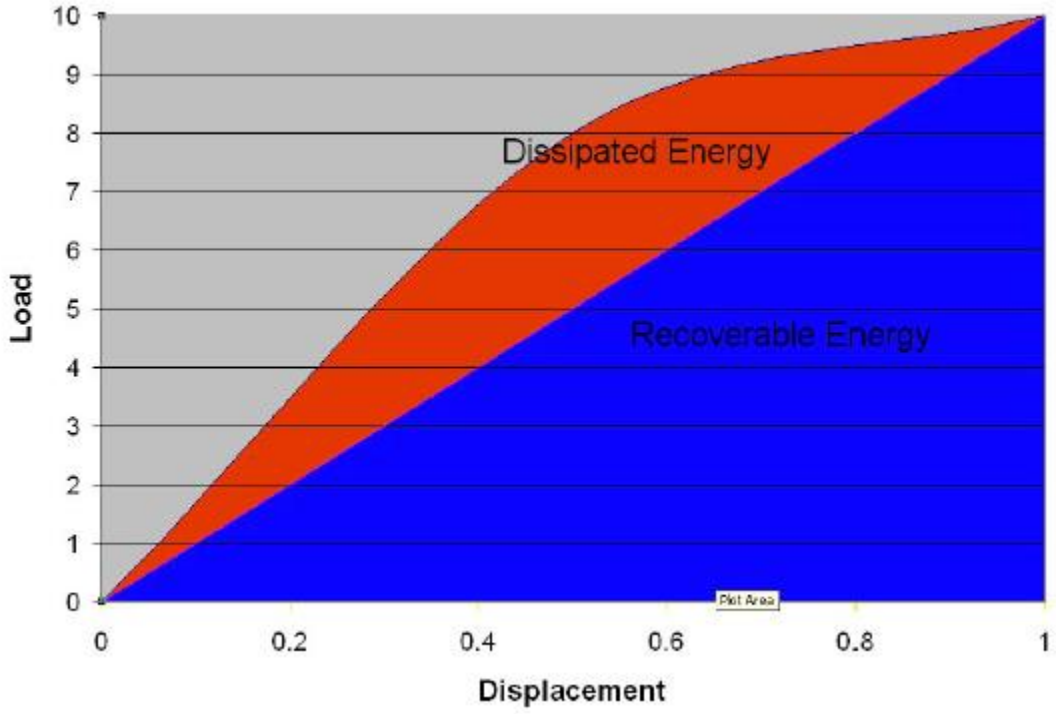

Figure 8. A generic load vs displacement plot as seen in Collett [11]. Only to illustrate dissipated energy

As a material is loaded, there typically exists a linear-elastic response until softening occurs. After softening occurs, the force vs. displacement curve levels off slowly as energy is dissipated. Finally, once the material is failed entirely, the load drops to zero. Ideally, if the material is unloaded at any point during the test the load and displacement will return to zero in a linear fashion – this portion of energy under the curve (bounded by the linear unloading line) is referred to as recoverable elastic energy. The portion of the curve that is not recovered is referred to as the dissipated energy. A graphical representation of this can be seen above in Figure 8. For a composite material, the softening phenomenon discussed above is idealized as contributing entirely to damage within the material. Although this assumption is not entirely accurate due to some typical non-linear elastic response in composite materials, it is a conservative assumption and will be used.

The idea proposed by the NRL was to use calculated dissipated energies at many points within a multiaxial test to determine the damage state of the material. Without too much detail, as in Schmitt [14], the basic steps of using dissipated energy density as a metric for damage is as follows:

1. Multiaxial mechanical testing in the In-Plane Loader
2. Measure boundary displacements and loads from the test
3. Measure experimental dissipated energies at many points throughout the test
4. Recreate test using a finite element model and obtain analytical dissipated energies
5. Minimize the difference between the analytical dissipated energy from step 4 and the experimental dissipated energies from step 3 by controlling the model

6. Once this difference is mitigated, use the finite element model strain values to determine “actual dissipated energy function”
7. This “actual dissipated energy function” is defined completely by in-plane strains and is proposed to act as a material property for quantifying damage.
8. This “actual dissipated energy function” can then be applied to individual elements in a model as a means of creating a functional continuum damage model.
    a. Once critical dissipated energy within an element is reached (based on strains), this element is said to have failed and its properties are altered or the element is broken.

This was a brief outline of the scheme. For more information regarding previous work using this dissipated energy scheme as a metric for damage see NRL’s publication [9].

For several reasons, it was decided for this research to not use dissipated energy density as a metric for quantifying damage during the test. After many publications and research trying to produce accurate progressive damage models using this method, there has never been a well-accepted model produced. This may be due to the “circular logic” of the scheme itself. In a way, a model is created to define damage properties for itself. Boundary conditions and measured dissipated energy are obtained from actual tests, assumed to be accurate, then used to adapt an idealized model. This produces an equation used to control the identical model with hopes of virtually reproducing the experimental test. In a way, this is very accurate but not a rule that generalizes well to many damage modes and states as shown by the work of Schmitt [14] and Smith [13]. Without normalization, these dissipated energy density calculations proved ineffective. This is not

stating that this method does not have merits, only that this research will not use dissipated energy the same way.

As a note, dissipated energy density is not the same as total dissipated energy. Dissipated energy density can be thought of and treated as an extension of strain energy release rate (a fracture mechanics material property). Dissipated energy cannot be treated as a material property but is useful as explained further below.

Dissipated energy as it pertains to this research is much simpler and, in a way, more primitive than dissipated energy density. For each sample, total dissipated energy is calculated only to detect the onset of damage and is never used as a metric to quantify damage accumulation. This will be explained further later; but as an example of a total dissipated energy calculation, see Figure 9 below. The dissipated energy is calculated for each deformation component (x-direction, y-direction, and rotation) independently then summed for “total dissipated energy”.

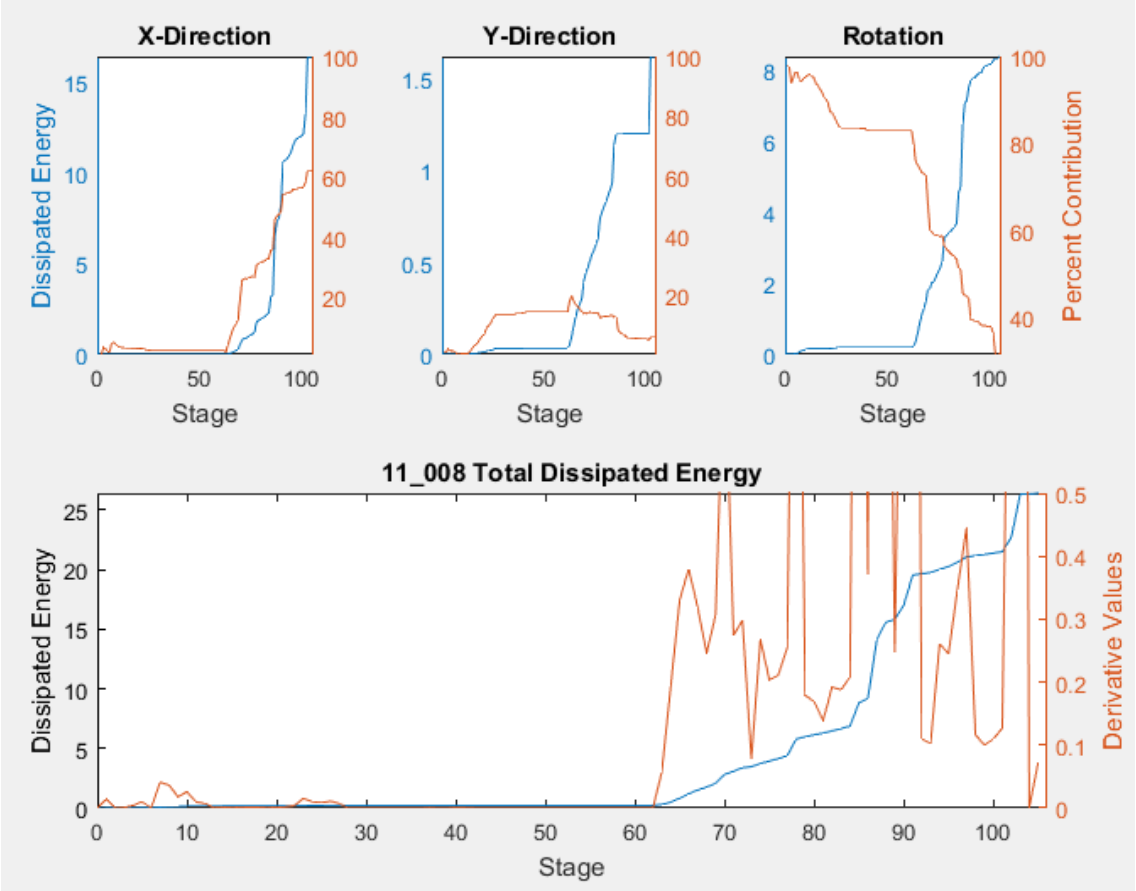

Figure 9. Example dissipated energy calculation for sample 11_008. Dissipated energy is expressed in units of $lbf \cdot in$

It can be easily seen that the dissipated energy 'jumps' at "stage 62". The "stage" axis is the image step for the test. At stage 62, there is in increase in dissipated energy for each deformation component (x, y and θ). Again, assuming all dissipated energy is attributed to damage in the material, the conclusion of the Figure 9 is that damage initiation occurs at stage 62 of the test and continues to progress until ultimate failure at stage 105. The calculation process, purpose, and place in post-processing will be described more fully later.

It is important to note that the method behind this total dissipated energy calculation is the same as shown in previous works. However, even though the calculations are handled the same way, the input displacements are now far more accurate as they are measured directly from the digital image correlation data rather than an assumed displacement taken from the IPL. The primary risk of using the assumed displacement data taken at the grips of the IPL is that it does not account any coupon slippage and assumes a perfect gripping scenario. Using new software and methodology for measuring displacement, the calculation of dissipated energy is more accurate.

Digital Image Correlation

Strain gauges and extensometers are a well-accepted industry standard for measuring strains in quasi-static mechanical tests. However, these two methods of strain measurement are discrete measurements that average strain values over the entire applied area of the test coupon. Therefore, localized strains (at stress concentrations and damage initiation sites) are nearly impossible to capture during a test using these methods. Strain information at stress concentrations and damage initiation sites is grossly determined via analytical methods with applied assumptions. Assuming material properties, including damage characteristics, often produces error since damage characteristics and even constitutive responses of composite materials are not fully understood (this is the data being tested for). So, like other challenges of material testing, this necessitated different methodology in measuring strains.

There are many types of full-field strain measurement methods. However as mentioned previously, due to Parker's work on digital image correlation, a commercial

DIC system (GOM ARAMIS) was purchased to satisfy the need for full-field strain measurement. The use of DIC doesn't only provide full-field strain data but is useful (as seen above) to measure boundary displacements, correlate to finite element models, present data, and much more.

The idea of digital image correlation is simple yet the application of it is difficult. For inquiries about the theory and technicalities of DIC refer to Parker [15] and Hild [16]. The basic premise of DIC is that through a series of non-contact optical measurements and analysis of these images, deformations can be calculated. To do this, DIC recognizes the surface structure of the measured object in digital camera images and allocates coordinates to the images' pixels. As the measured object is deformed, the software can keep track of the surface structure and calculate displacements based on the new images' coordinates. More simply, DIC software tracks the displacements of each speckle on a pixel-level from image to image to calculate the full-field deformation. An example of the stochastic[‡] spray pattern used for DIC can be seen in Figure 10 below.

[‡] Stochastic – A randomly distributed pattern that may be analyzed statistically but not necessarily predicted.

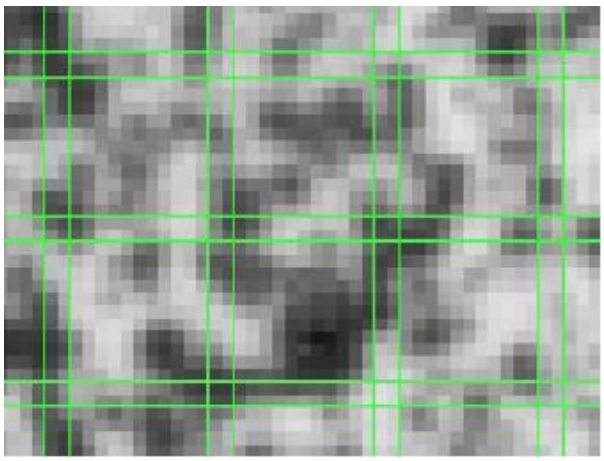

Figure 10. Image of acceptable stochastic pattern with 15×15 facets [17]

The facets represented in the image above are analogous to elements in a finite element model. The smaller the facet, the higher resolution deformation calculations will be but at the cost of increased computation time. Facet boundaries are defined based on unique high-contrast areas of the spray pattern. These areas that define the facet boundary are what the software tracks throughout each image. Deformation of the measuring object, or even a view from another camera, results in a change within the calculated facets as shown in Figure 11 below. For this research, facets with dimensions 15×19 pixels are used to maintain a manageable computation time but have reasonable resolution.

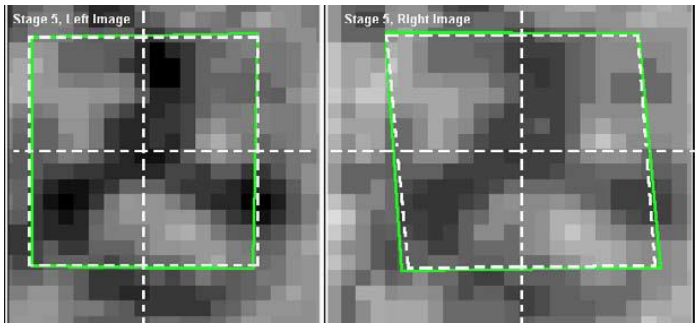

Figure 11. Facet tracking as shown in the ARAMIS manual [17]

An example of a test that has been fully post-processed within ARAMIS can be seen in Figure 12 below. In Figure 12, there are four images displayed. The left-most image shows displacement vectors for each calculated facet. The second, third, and fourth images show computed strains displayed as gradient overlays ($\varepsilon_x, \varepsilon_y, \varepsilon_{xy}$ respectively). There is also additional information shown on the graphs and in the table including load data, frame time, and test rate.

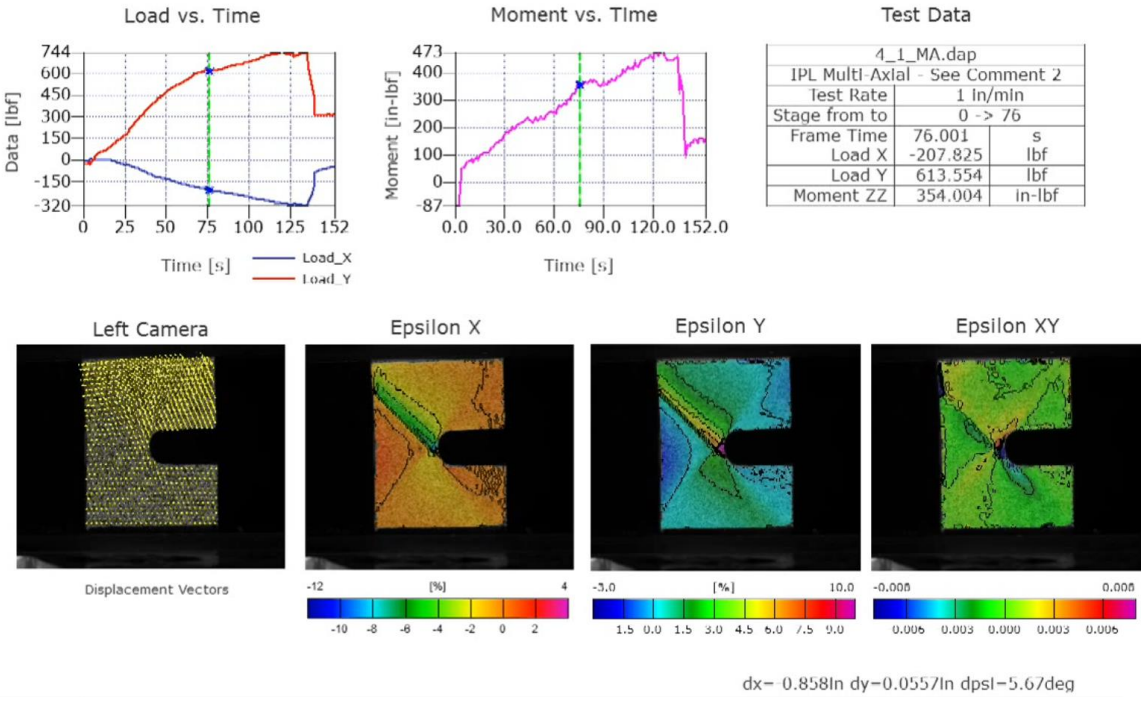

Figure 12. Example of ARAMIS post-processed data and data presentation. (Still image of a video taken just after damage initiation)

The ARAMIS hardware system is composed of a computer, sensor control module (DAQ), and the sensors (cameras). The image shown in Figure 13 below shows the computer and cameras. It is important to note that the cameras are a stereo system, meaning

they observe the measuring object from different angles and allow the calculation of depth (z-axis) deformation. This stereo setup is beneficial for two reasons. First, correlation between the left and right camera images for each stage produces much more accurate results than a single-camera setup. For this setup, average measurement error is consistently computed to be less than $0.00003\ in$. Second, as mentioned, these two cameras allow for the calculation of depth (z-axis) which assures that in-plane tests are in fact in-plane. In practice, local coordinate systems can be created for complex part geometry using these features as well.

Figure 13. GOM ARAMIS hardware as shown in ARAMIS Manual [17]

Test Coupon

Material Systems

Both material systems explored are carbon fiber reinforced polymers (CFRPs). They are unidirectional prepreg[§] systems composed of a single continuous carbon fiber type and a single resin system. This prepreg system allows for the highest industry standard fiber volume fraction, highest quality fiber orientation, and even complex shapes to be produced. The first material system to be explored is a Hexcel 8552 IM7 (also referred to as IM7/8552). The second system is a more brittle and slightly thicker material system produced by Toray. Material properties pertinent to this work are displayed below in Table 1. These material properties will be used to produce a finite element model.

Table 1. Lamina material properties for both material systems. Material properties are specified for material at room temperature and dry (RTD) [18]

Material Property	**IM7/8552 Value**	**Toray Value**
E_1 (msi)	23.51	20.6
E_2 (msi)	1.30	1.13
E_3 (msi)	1.30	1.13
ν_{12}	0.356	0.34
ν_{13}	0.356	0.34
ν_{23}	0.53	0.53
G_{12} (msi)	0.68	0.58
G_{13} (msi)	0.68	0.58
G_{23} (msi)	0.38	0.37

Furthermore, and useful later, is a list of strength properties for IM7/8552 shown below in Table 2. All values for IM7/8552 are from the National Institute for Aviation

[§] Prepreg – a fibrous material preimpregnated with a resin system. The resin system is typically a partially cured epoxy already containing the appropriate curing agent.

Research (NIAR) [18], and all values for the Toray properties were provided. No strength properties were provided for the Toray material system.

Table 2. Strength properties for IM7/8552. Properties are specified for material under quasistatic loading at room temperature and dry (RTD) [18]

Strength Property	IM7/8552 Value (ksi)
F_{1_tu}	371.08
F_{2_tu}	9.29
F_{1_cu}	251.13
F_{2_cu}	41.44
F_{12}	13.22

Several different laminates were provided for each of these material systems. For this research, three different laminates of each material system were tested and analyzed. Stacking sequences and naming convention numbers are displayed in Table 3 below. Each sample is named using the format XX_0YY where the "Layup Number" from Table 3 replaces XX and YY is replaced by the appropriate "Test Number". For example, the name 11_001 would be the first test performed on the $[-45/90/45/0]_s$ layup of the IM7/8552 material system. These numbers are for bookkeeping only and have no significance other than to keep track of tests. For a full list of tests, refer to the test matrices in the appendix.

As a note, the stacking sequences are displayed "as-tested" and are not the stacking sequences "as-manufactured". For example, the stacking sequence $[-45/90/45/0]_s$ is actually manufactured as $[45/90/-45/0]_s$ but measurements were taken from the 'back side' of the coupon. Measurements were decidedly taken from this side of the coupons since the 'back side' of the material was smoother than the 'front' and was a better surface for use with the DIC.

Table 3. Laminate stacking sequence table and layup numbers. Naming convention of tests uses "Layup Number" to replace XX of XX_0YY

Stacking Sequence	**Layup Number**	
	IM7/8552	**Toray**
$[-45/90/45/0]_s$	11	1
$[0/90/0/90]_s$	13	3
$[-45/45/-45/45]_s$	14	4

Geometry

After a compact tension sample study conducted by Ritter [12] in 2005, the "standard" IPL coupon was created to resemble a 'modified compact tension sample'. The most current version of the IPL sample is shown below in Figure 14. The purpose of the notch (also referred to as a strain riser) is to create a stress concentration in the sample as an attempt to force failure to the middle of the gauge section of the coupon rather than near the gauge section boundaries. This geometry was chosen as it produces the desired failure location and proved to be easily reproducible from a manufacturing standpoint.

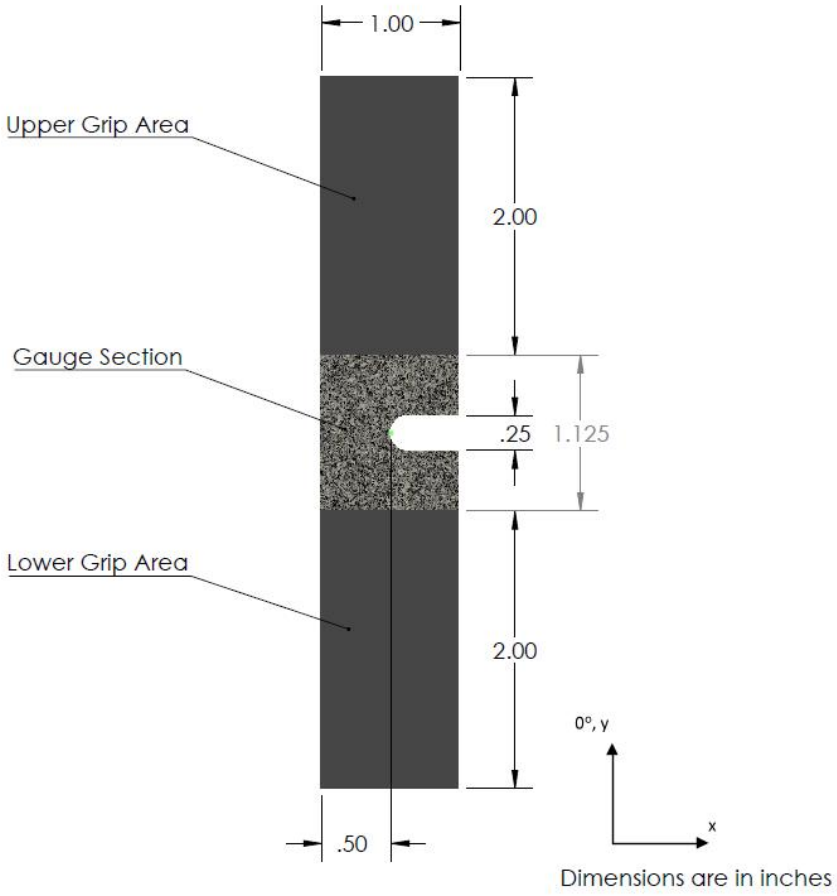

Figure 14. Latest coupon geometry. Identical gauge section to previous samples but larger grip areas. The displayed coordinate system is not displayed at the working origin. Reference below, Figure 20

Manufacturing

Large flat panels were received for each of the above specified material systems. The panels measured $24\ in \times 48\ in$ and needed to be cut down to dimensions shown in Figure 14 for testing. This process took several steps to produce the coupon geometry and is summarized below:

1. The received $24\ in \times 48\ in$ panel was cut down into minimum nominal $10.5\ in$ strips while maintaining and tracking material orientation. This step was only to make manufacturing more manageable.
2. Each $10.5\ in$ strip produced in step 1 was then cut in half lengthwise to produce material strips with the proper $5.125\ in$ sample height.
3. Strips produced in step 2 were then cut slightly larger than the specified $1.00\ in$ width shown in Figure 14. This produced samples $5.125\ in$ tall and just over $1.00\ in$ wide.
4. The edges of the samples produced in step 3 were then sanded carefully to remove edge fibers and reduce the influence of damage introduced from steps 1-3. Resulting sample dimensions were $5.125\ in$ and $1\ in$ (nominal).
5. The samples were then notched using a $0.25\ in$ 3-flute "diamond-like" coated ball end mill shown in Figure 15 below.
    a. This was done for 5 samples at a time and cut as slowly as possible. Typically, a machinist would take multiple passes to produce such a deep cut. However, to prevent the introduction of damage during the notching process, this was done in a single pass.

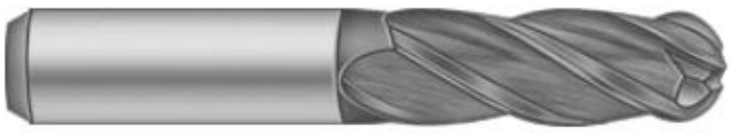

Figure 15. Diamondlike-Coated Carbide End Mill, Ball-End, 4 Flute, 1/4" Mill Diameter, 2-1/2" Overall Length [19]

After the samples were cut to the appropriate dimensions, they were cleaned and dried using only water to remove oils and particulates from the surfaces. Prior to testing, the samples still needed further preparation to use in the IPL and for the use of ARAMIS DIC. Each sample was tabbed, not necessarily to reduce gripping effects but to ensure each sample was thick enough ($0.125\ in$ minimum) so that the transverse support plates in Figure 6 could be used for each test.

Table 4. Statistical values for geometry of all tested coupons. Measured with Mitutoyo digital calipers verified with standardized machinist gauge blocks

Measured Property [spec (in)]	**Statistical Values (in)**	
	Mean	**Std. Dev**
Notch Depth [0.50]	0.5036	0.0050
Notch Width [0.25]	0.2497	0.0013
Coupon Width [1.00]	1.0032	0.0083

Samples were then painted using a flat white and flat black self-etching spray paint. The white spray paint provided a base coat that was then "speckled" with the black paint. This produced a stochastic pattern satisfactory for the DIC software to establish facets for strain and displacement calculations. Self-etching paint was chosen as other paints would chip off the surface of the coupon during deformation due to poor paint-to-coupon bonding. An example end-result of coupon manufacturing and preparation can be seen in Figure 16 below.

Figure 16. Result of manufacturing procedure. *This sample was flawed due to improper tabbing and was therefore not tested. A side-view to show tabs (top). Front view (middle). Inch ruler for scale (bottom)

EXPERIMENTAL DATA – MULTIAXIAL TESTS

The primary purpose of this data is to produce qualitative and quantitative data to inform and validate progressive damage models. Only some of the data produced from these tests can be shown in a document format. Most of the data obtained from these experimental tests is stored as ARAMIS files that may prove useful for direct comparison (in ARAMIS) of progressive damage models and actual tests. Later software versions of ARAMIS allow for the import and direct comparison of analytical data to measured experimental data (these comparisons have not been performed for this research). Experimental data is also exported as video report files like Figure 12 shown previously. These video files may prove useful for qualitative comparisons between analytical models and measured experimental data.

The data that will be shown focuses on damage initiation under multiaxial loads. As discussed previously, composite materials' constitutive responses are not well-understood and their damage characteristics even less so. Providing information regarding damage initiation may be a useful tool as the onset of damage is just as poorly understood as its progression throughout the material.

Testing Procedure

After coupons are fully prepared, they are then ready to be tested. This section will, in little detail, discuss the steps necessary for testing a sample using both the IPL and ARAMIS DIC systems simultaneously. It is important to note, like all other previous works with the MSU IPL, that the IPL has not been optimized for high volumes of tests

and therefore each test requires a minimum of thirty minutes to perform. The basic steps for running a test in the IPL are listed below:

1. Load a fully prepared sample in the IPL grips
    a. Similar to loading a sample in a typical Instron machine, the crosshead is moved into position and the sample is clamped in place.
    b. Clamping the sample is done incrementally. Some load is applied via the hydraulic pump, fasteners tightened, and transverse support plates slid up against the side of the coupon. Doing this incrementally ensures all gripping components are in full contact with the sample.
2. Recalibrate IPL position and initialize test.
    a. IPL position is recalibrated to ensure current configuration is accurately being controlled by the software.
    b. Initialize IPL test speed and begin load output voltages.
3. ARAMIS DIC project file is created and any necessary adjustments (shutter time, lighting, etc.) are made.
4. Proper displacements and data storage location (for .txt file) are chosen on the IPL.
5. ARAMIS DIC is started and begins taking images (stages) and collecting load data. Several stages are taken before starting movement of the IPL.
6. Once the ARAMIS DIC measurement has been confirmed, the IPL is started and the test runs to the prescribed displacements in step 4.
7. Once final failure occurs, or for any reason the test needs to be stopped, ARAMIS is stopped first then the IPL is stopped.

Loading Paths

The theory for testing these samples was similar to the original proposition by the NRL [9]. Through many "arbitrary" combinations of in-plane displacements, a material's damage characteristics may be fully characterized for all displacements encompassed by tested values. The mechanical behavior of the material is understood to depend only on the current internal strain state and to be independent from any particular path. This path independence allows for 'a family of loading paths to be selected solely on the basis of convenience' [9].

NRL's publication goes on to describe and justify their load path selection (Figure 17 below) and state that due to material symmetry 'only the half-space corresponding to positive sliding displacement [x-displacement] need be considered'. However, due to limits of the IPL and the lack of material symmetry of these samples, a different loading path scenario was created for this study.

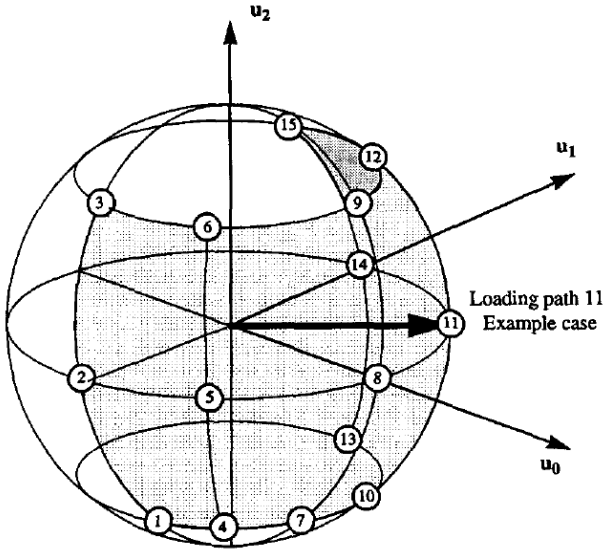

Figure 17. Schematic of NRL's loading path definitions [9]

First, compression tests ($-dy$) are difficult with the MSU IPL. This is due to several reasons but is primarily due to out-of-plane response of the IPL, and buckling due to coupon geometry. Buckling is said to be due to coupon geometry since buckling is geometrically stability driven and not driven by material properties. Several compression tests were carefully performed in the IPL to assess the IPL's ability to perform compression tests. Each compression test that was attempted failed due to an out-of-plane response of the IPL and ultimately buckling of the coupon. Buckling of the coupon could be rectified, in theory, by changing coupon geometry for compression tests and out-of-plane response of the IPL may be rectified by adding stiffeners to the out-of-plane constrainers. However, for this research, buckling tests were omitted as they did not produce reliable in-plane strain data. An example of coupon buckling can be seen in Figure 18 below showing an out of plane displacement of the coupon from $0.494\ mm$ to $-1.081\ mm$, a $0.062\ inch$ out-of-plane displacement of the sample. Again, since the ARAMIS cameras are stereo cameras, they allow for displacement calculations out-of-plane (z-direction) but cannot accurately compute non-planar strains.

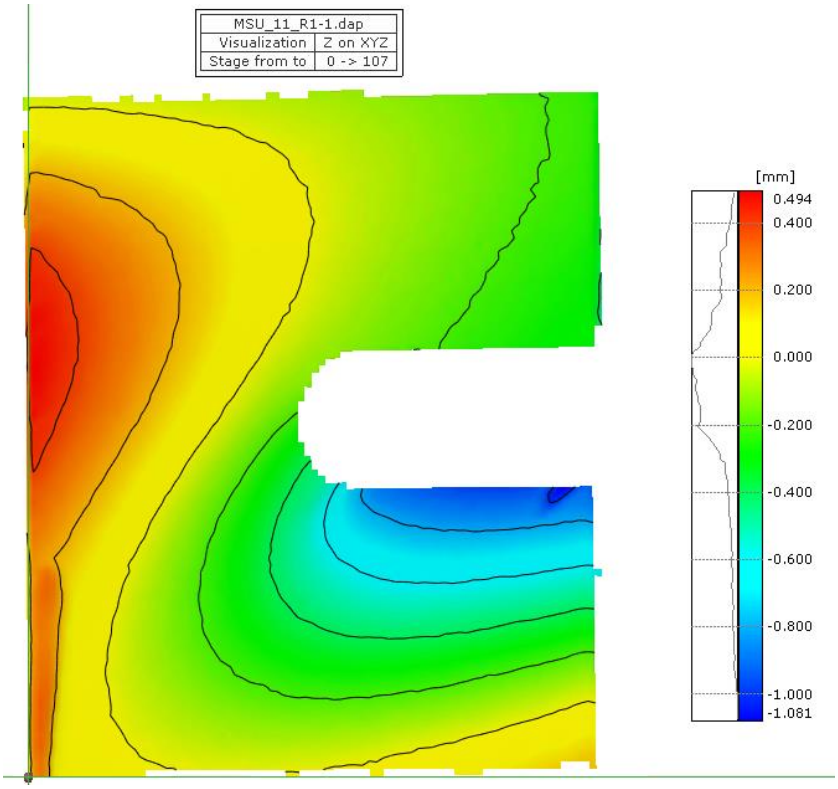

Figure 18. Image of out-of-plane displacements recorded via DIC for a failed compression test

Second, as mentioned above, material symmetry does not exist for off-angle laminates about the x-axis. Therefore, it is important to include both positive and negative x-displacements for the load path selection. The resulting load path selection is similar to NRL's except for these changes and can be seen in below in Figure 19. The load paths included in the figure are only those performed on every laminate. Some laminates have more tests included for the data presented later. For more information on all tests performed, refer to the attached test matrices located in the appendix. Note that displacements recorded in the test matrices are not actual displacement achieved and were

entered as larger-than-necessary values to ensure final failure for each test. For more information regarding tests performed in this study, see the test matrices in APPENDIX A.

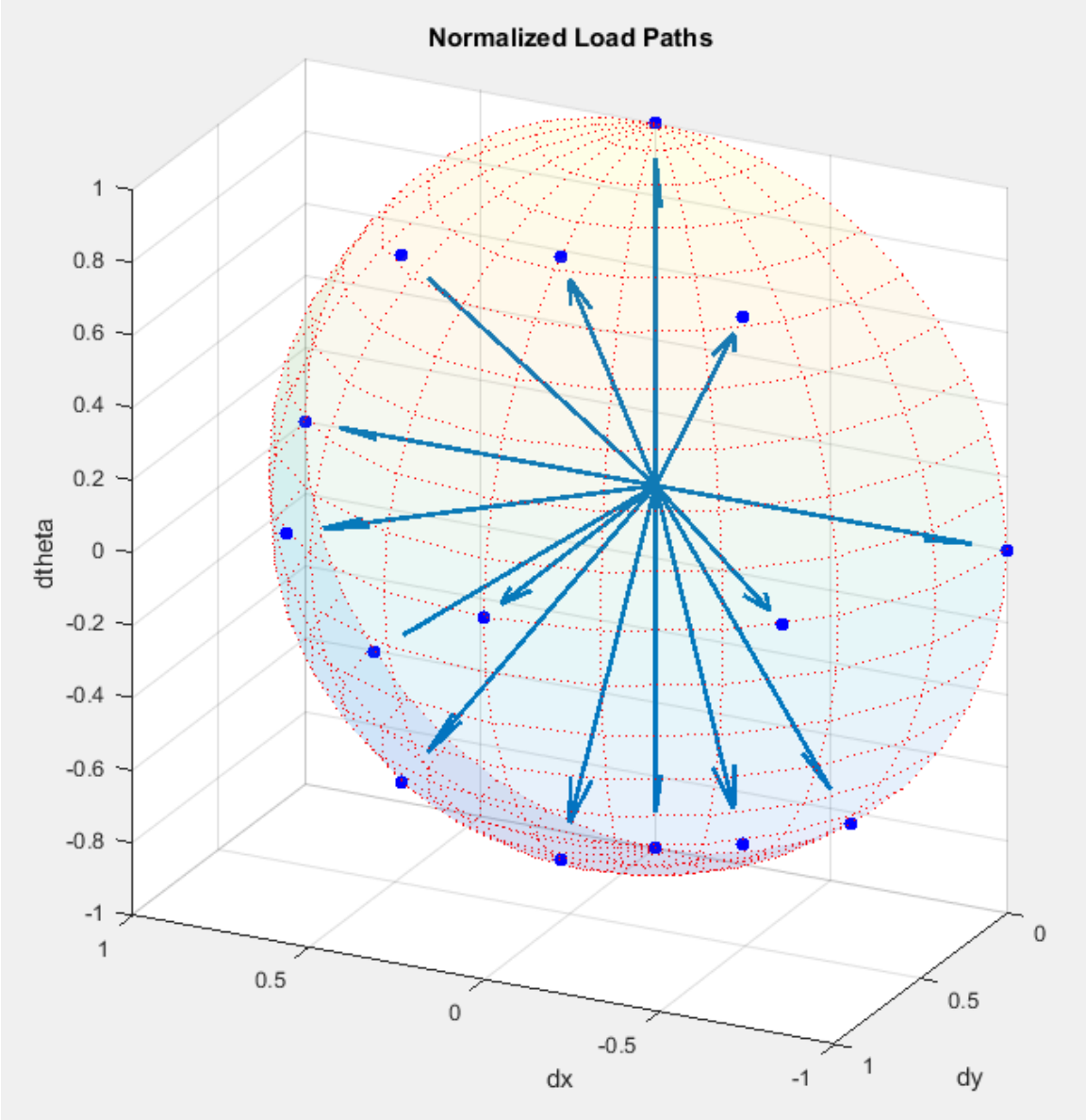

Figure 19. Normalized load paths (displacement paths) performed for every laminate. Vectors shown as unit vectors to display direction only

Data Acquisition

As mentioned before, the ARAMIS system acts as the primary data acquisition for testing. All data collected is stored within ARAMIS software and can be handled in the software as well as exported. Due to the version of the software (v6.3) automation and calculation within ARAMIS is limited and can take more than two hours per sample to fully process. See the recommendations section for more information regarding ARAMIS software restrictions.

Since all the data is handled in ARAMIS but processing within the ARAMIS software is cumbersome, some processing is performed in ARAMIS then exported and passed on to MATLAB for further processing. This section will focus on the how the data is obtained from the IPL to ARAMIS, post-processing within ARAMIS, and export processes.

1. The stereo camera, as described previously is setup such that the entire coupon is within view and will stay within view of both cameras for the duration of the test. Each camera has been focused, and adjusted appropriately such that both camera images are aimed close to the same point on the sample.
2. While the test is run, analog voltage values are collected via typical BNC cable connections like an Instron machine. Three independent voltages are collected with a range of $\pm 10\ V$. These voltages correlate to real-time load data from the IPL and represent loads in each resolved direction (x,y, and θ). This coordinate system is the same as discussed above and below (ex. Figure 3). These voltages are then linearly transformed with independent gain values to convert the raw

voltages to units of lbf for x and y direction loads and $in \cdot lbf$ for the moment about the top center of the coupon.

3. Once a test is completed, data collection in the ARAMIS software is terminated and processing begins. There are several basic steps that must be performed to each test before actual processing begins.
    a. Several "start points" are created on each area of interest on the coupon. A minimum of one start point must be created for each intact part of the gauge section; once cracking occurs, a start point must exist on each side of the crack to process both areas.
    b. After all the desired start points are created, the project is then computed. This step can take up to an hour for each test depending on gauge section size, facet size, and length of the test. For these samples, facets of 15×19 pixels were used and a test length of 150 stages was the desired test length. This was to keep processing time to a minimum but maintain reasonable data density.
4. The "compute" function described in 3b performs most of the necessary large computations for the test. However, there are several additional steps within ARAMIS software before the data can be exported for further post-processing in MATLAB. Each of the listed items below can be seen in Figure 20 below.

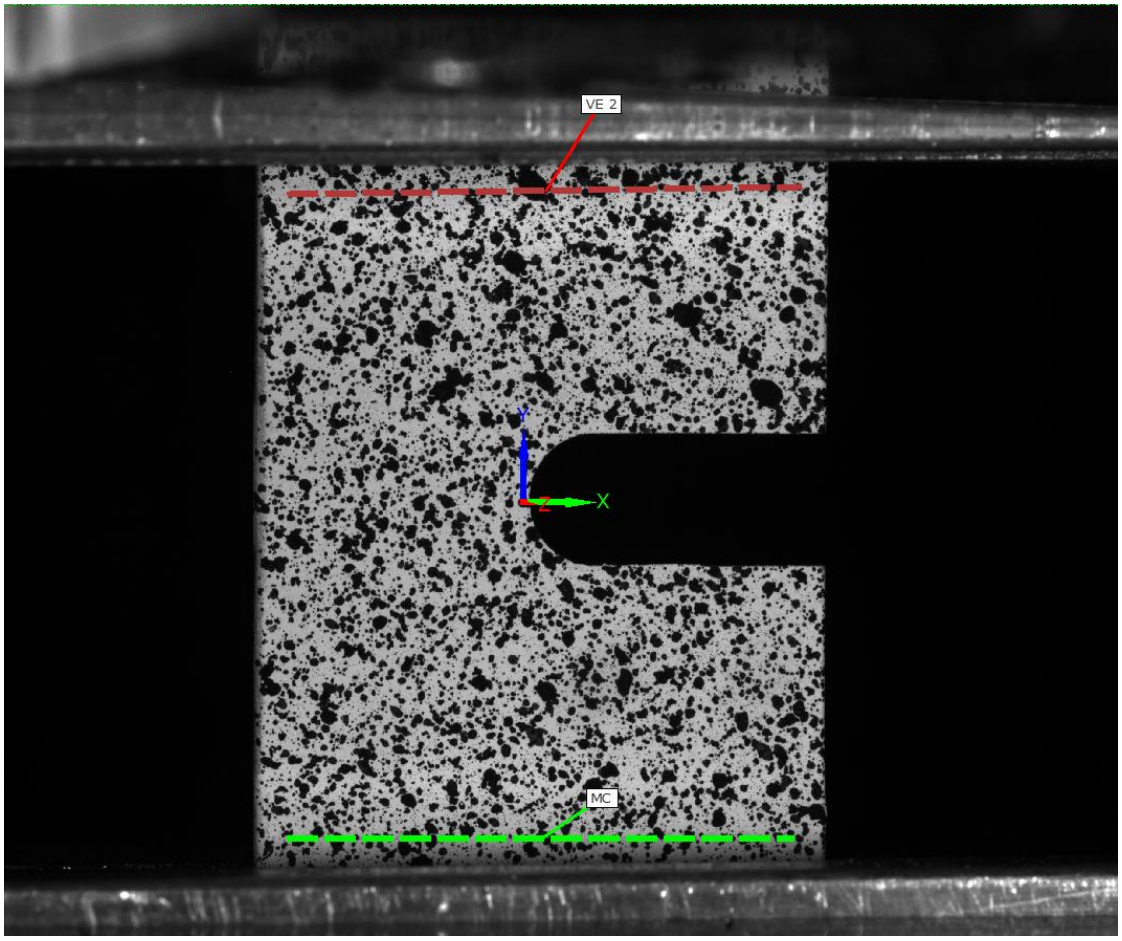

Figure 20. Left image of test 11_024 as a demonstration of ARAMIS image acquisition. (Green line [MC]) shows "movement correction". (Red line [VE 2]) shows “virtual extensometer”. Coordinate system is shown at the notch tip

a. First, the test is corrected for “movement correction” which accounts for rigid body displacements of the sample (grip slippage, light distortions, IPL vibrations, and camera movements can be accounted for). This step “fixes” the bottom boundary of the coupon by creating an artificial *fixed boundary condition* on the coupon for computation purposes.

b. Second, a coordinate transformation is then applied to the coupon. This aligns the coordinate system about the center of the notch tip with the y-axis pointing upward, the x-axis toward the open end of the notch, and the xy-plane aligned with the plane of the sample. This ensures that computed strains are consistent between each sample and correspond directly to the finite element model discussed later.

c. Finally, a "virtual extensometer" is created at the top boundary of the gauge section to directly measure the top boundary displacement of the coupon. Again, the bottom boundary condition is accounted for in step 4a (movement correction).

5. All computed data in ARAMIS may be exported without further processing within the ARAMIS software. For reports, strain images, and other ARAMIS objects, further processing within ARAMIS is required.

Post-Processing in MATLAB

Basic Post-Processing Scheme

For completeness and reproducibility, this section will describe, in fair detail, the post-processing scheme used to further analyze test data. Some of the post-processing is handled directly in the ARAMIS software as described above. However, due to software and automation restrictions, further post-processing of data is handled in MATLAB. The basic post-processing scheme is described below and, for clarity, relative figures will be included in-line with relevant text:

1. Two methods of exporting processed data from ARAMIS to .txt files

a. First, a single text file including displacement data from the 'Virtual Extensometer' created in step 4b above and collected load data for all stages obtained in step 2 above.

b. Second, individual text files for each stage include facet location (deformed and undeformed), and facet strains (deformed).

2. Displacements and loads from the text file created in step 1a are imported to MATLAB to determine dissipated energy.

   a. Numerical integration for each load path (x-displacement, y-displacement, and rotation) to determine dissipated energy developed throughout the duration of the test. This is performed using a standard trapezoidal rule numerical integration scheme shown in Equation (6) as a demonstration of the integration scheme for the x-component.

$$DE_x = \int_o^n F(x)dx \approx \frac{\Delta x}{2}\left[F(x_0) + 2\sum_{i=1}^{n-1} F(x_i) + F(x_n)\right] \quad (6)$$

   b. Calculated dissipated energy determines the stage where damage is initiated during the test. This calculation and result has already been demonstrated in Figure 9.

3. Based on the damage initiation stage determined from 2b, strain data from 1b (for the appropriate stage) is imported and further processed in MATLAB.

   a. Strain data is truncated to exclude "exterior" facet calculations. Facets close to the edge of the sample are typically inaccurate as "boundaries" are not well-defined for these edge facets. All facets lying outside the

inner 90% for each left-to-right and top-to-bottom measurement is discarded. See Figure 21 below for a graphical representation of the acceptable facet location.

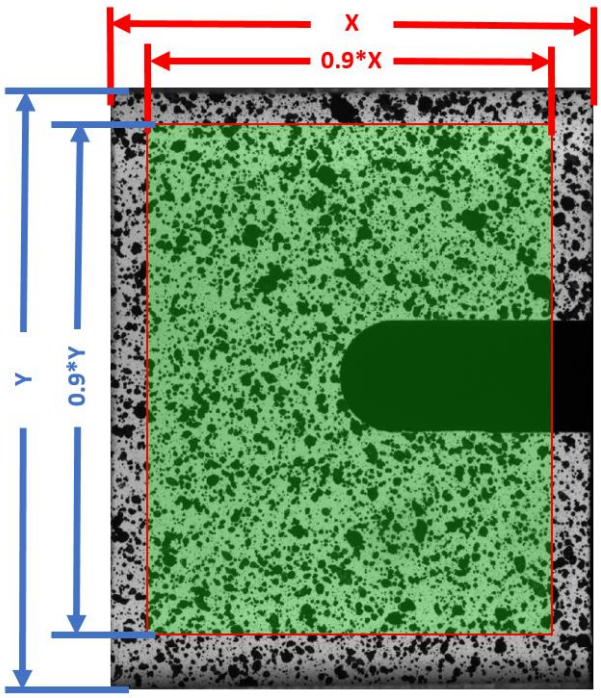

Figure 21. Image of facet truncation. Area enclosed in the green rectangle is the area of accepted facets

b. All truncated strain data for each sample type (each individual laminate) is collected and grouped as a whole.

4. A point cloud is created in 3D strain space for each laminate (all components of in-plane strains). Resultant figures will be displayed in the Results section to follow.
5. Point cloud density is calculated. This is done for every single point in the point cloud – each point is assigned a "weight" based on the point cloud density at

that point. This calculation takes approximately an hour for each laminate but only needs to be performed once per point cloud.

a. The distance is calculated from a single point to every other point in the point cloud. This is done with the simple distance formula shown below in Equation (7) below. As stated, this calculation is performed for every point therefore requires $n \times n$ calculations where n is the number of points in the point cloud.

$$d_i = \sqrt{{x_i}^2 + {y_i}^2 + {z_i}^2} \tag{7}$$

b. For a single point, after each distance is computed, these distances are sorted and compiled into a single value using weights seen in Equation (8) below. The weights applied can be controlled arbitrarily to produce varying results for the next section. The weights displayed below are the values used for the figures produced and shown in this report. Note, these $density$ values are actually distances; therefore, the smaller the $density$ value, the more dense the point cloud at that point.

$$density = C1 \times \delta 1 + C2 \times \delta 2 + C3 \times \delta 3$$

$$\delta 1 = \left(\sum_{i=1}^{50} d_i \right) \Big/ 50$$

$$\delta 2 = \left(\sum_{i=1}^{0.005 \times n} d_i \right) \Big/ (0.005 \times n) \tag{8}$$

$$\delta 3 = \left(\sum_{i=1}^{n} d_i \right) / n$$

i. The average of the smallest 50 distances to the point ($\delta 1$).

ii. The average of the smallest 0.5% of the distances to the point ($\delta 2$). This results in approximately the smallest 2500 distances.

iii. The average of all distances ($\delta 3$)

iv. For these results: $C1 = 2,\ C2 = 2, C3 = 1$. This is to ensure closer points have a greater weight than all points.

c. Finally, this process repeats for every single point in the cloud and assigns a $density$ value to each. This is where the calculation takes most of its time and requires $n \times n$ calculations.

6. Using point location $(\varepsilon_x, \varepsilon_y, \varepsilon_{xy})$ and the $density$ computed in step 5, isosurfaces are created based on the cumulative distribution probability of each point. Using this cumulative distribution probability, the calculated $density$ value has no weight and has no relative significance compared to any other value. The surface can now be controlled entirely based on point density probability, i.e. the surface lies on or contains the densest XX% of all data points.

7. Isosurfaces can then be "sliced" and projected onto planes for easier viewing.

This concludes the primary post-processing performed for this study. Each step was performed on every laminate type tested; selected results will be displayed in the results section. The schematic version of the above post-processing scheme is displayed in Figure 22 below.

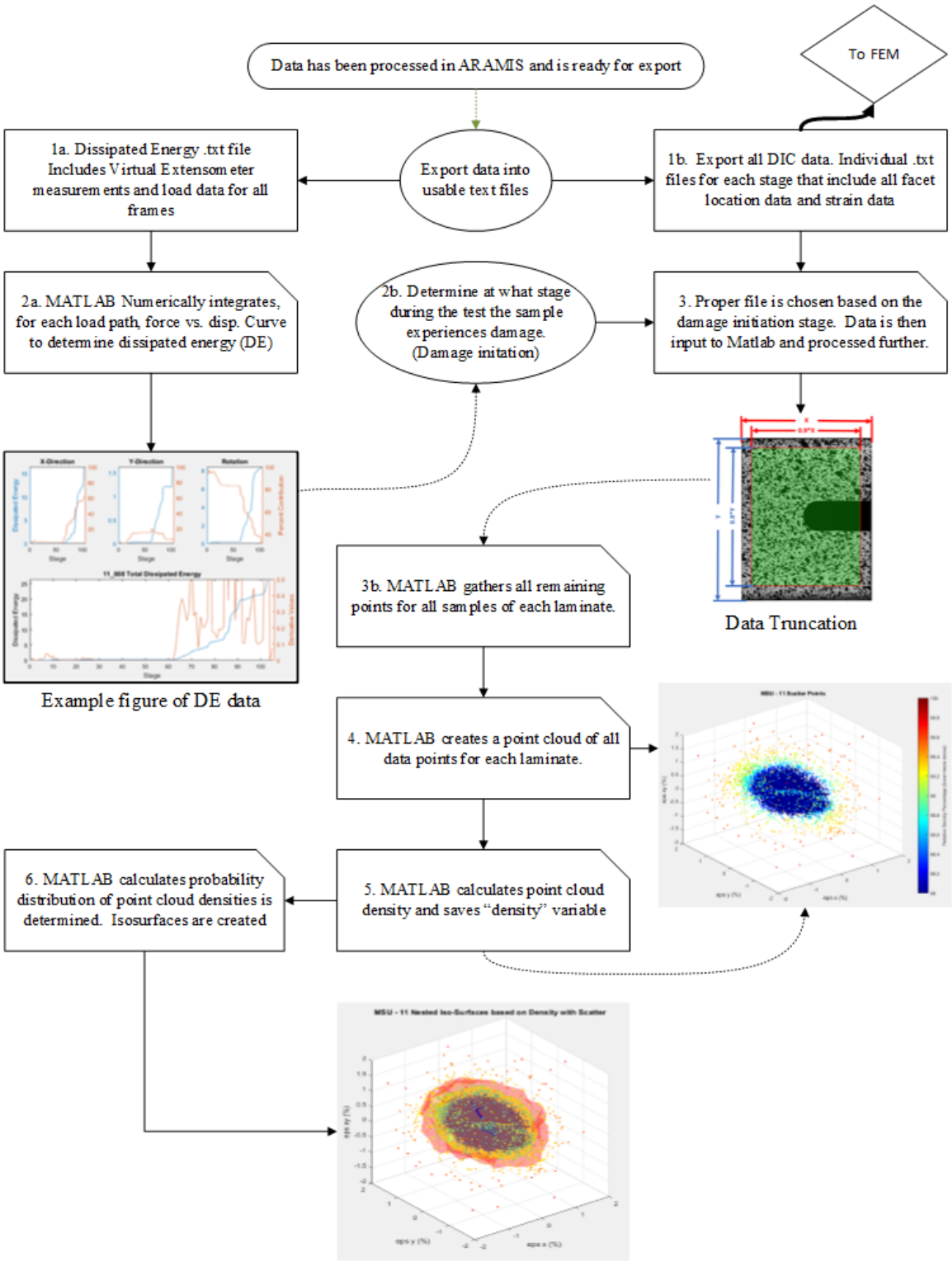

Figure 22. Schematic view of the post-processing scheme used to further process ARAMIS data via MATLAB. For more detail about each step, refer to the section above

The strain data for all laminates of a single material can then be computed and shown; this is a step in the post-processing that is not displayed in the schematic above. The global coordinate strain data can then be transformed into each ply and then displayed as a "ply property" with axes 1, 2, 12 in-plane strains. This may prove to be more useful from a modeling perspective but, requires manipulation of the data and assumptions to resolve.

- First, the assumption used to produce this ply-level data is that strains are constant through the thickness of the sample. This is not necessarily true and may produce unrealistic results.
- Second, and simply, this requires a simple coordinate transformation of the measured surface strain data onto each other laminate. For example, the quasi-isotropic laminate would need 4 strain transformations to account for each layer because the layup is $[-45/90/45/0]s$. This transformation can be seen by the simple linear transformation of the strain vectors shown in Equation (9). θ represents the angle of rotation from the global x-axis to the fiber direction of the respective ply.

$$\begin{Bmatrix} \varepsilon_1 \\ \varepsilon_2 \\ \varepsilon_{12} \end{Bmatrix} = \begin{bmatrix} c^2 & s^2 & -2cs \\ s^2 & c^2 & 2cs \\ cs & -cs & c^2 - s^2 \end{bmatrix} \begin{Bmatrix} \varepsilon_x \\ \varepsilon_y \\ \varepsilon_{xy} \end{Bmatrix} \tag{9}$$

Where $c = cos(\theta)$ & $s = sin(\theta)$

After each ply-level strain has been determined for every ply within every laminate, all ply data is gathered together as either IM7/8552 or Toray ply-level strains (whichever the ply belongs to). This data is now much larger than any one laminate and cannot be processed the exact same way; but it is processed similarly.

Results and Discussion

Again, results from experimental tests are to produce data that informs and validates progressive damage models. As such, this data is qualitative and quantitative. Examples of the qualitative data can be seen below that may be useful for side-by-side comparison to finite element models. Results like those produced by the post-processing scheme above, are quantitative and could be useful for informing progressive damage models in different ways. Progressive damage models including discrete damage models[**] but, particularly continuum damage models[††] require a failure criterion to determine when the element experiences damage. As discussed previously, existing analytical failure criterion are not necessarily representative of how the material experiences damage; the failure criterion developed in this study and described below is *entirely* based on experimental data.

Failed Coupons

First, a lot of information can be obtained by inspecting failed coupons. Fracture surfaces are often observed in metal materials to better understand how fracture occurred; the same can be done for composites. Images of some of the most interesting failed coupons can be seen in Figure 23, Figure 24, and Figure 25 below. Failure modes are typically consistent between laminates and do not drastically vary between ply materials. For this reason, two images Figure 23 and Figure 24 are for the IM7/8552 material and

[**] Discrete Damage Models – Models that attempt to discretely model damage in the material. Done by "breaking" elements. These models can be particularly accurate on a small scale as they may model damage directly but require the most computational expense to solve.

[††] Continuum Damage Models – Damage prediction models that model damage by a means of "degrading" material properties of damage elements. In practice, these models are the most efficient from a computational standpoint but the least accurate in material representation especially on a small-scale.

Figure 25 for the Toray material system. These figures do encompass all layup orientations included in this study.

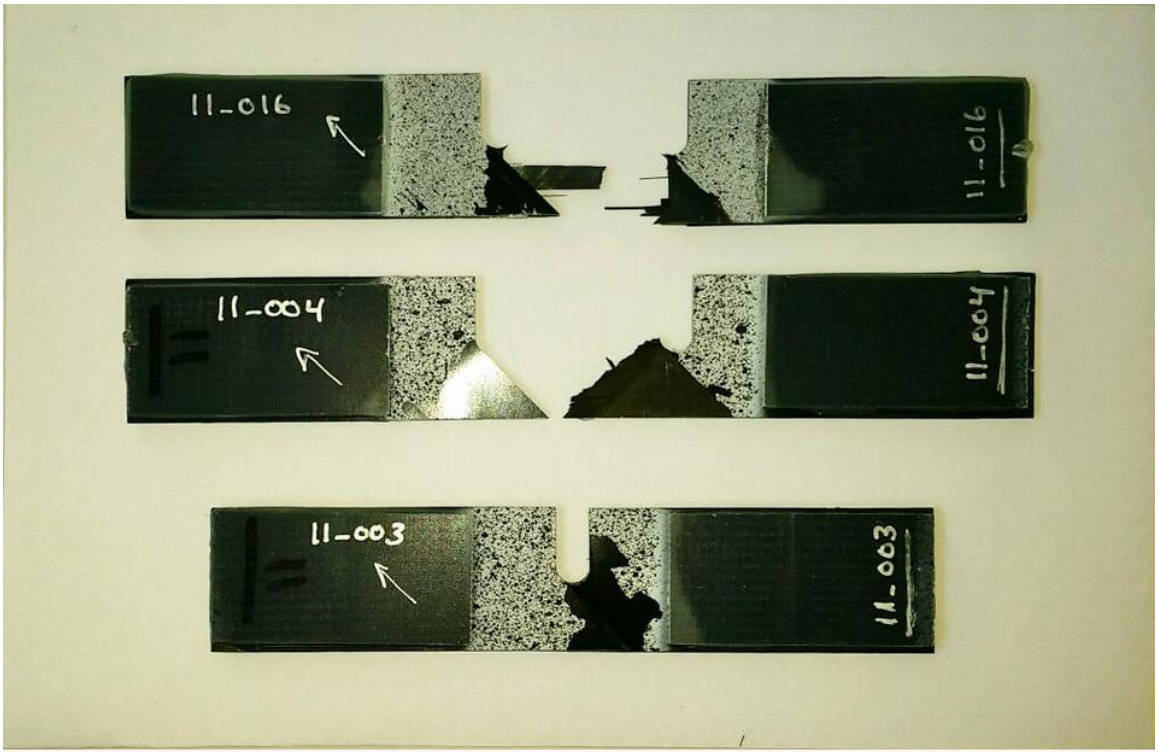

Figure 23. Laminate 11 interesting failures. Written labels correspond directly to the test matrix. For scale, coupon widths are 1 inch or refer to Figure 14 above

Figure 23, above, displays interesting failures of the IM7/8552 quasi-isotropic laminate [-45/90/45/0]s. Since this laminate is composed of 4 different layers, many damage modes can be seen. The 3 selected coupons demonstrate, in different ways, some of these failures. The top coupon shows the most failure modes including fiber rupture seen in the 0° plies, matrix cracking in every ply, and delamination. The middle coupon is interesting as there is clear fiber rupture in the $-45°$ plies. The bottom coupon, although

it is difficult to see, has not failed entirely yet and is held together by the intact 0° plies. Again, this image provides interesting data into many failure types.

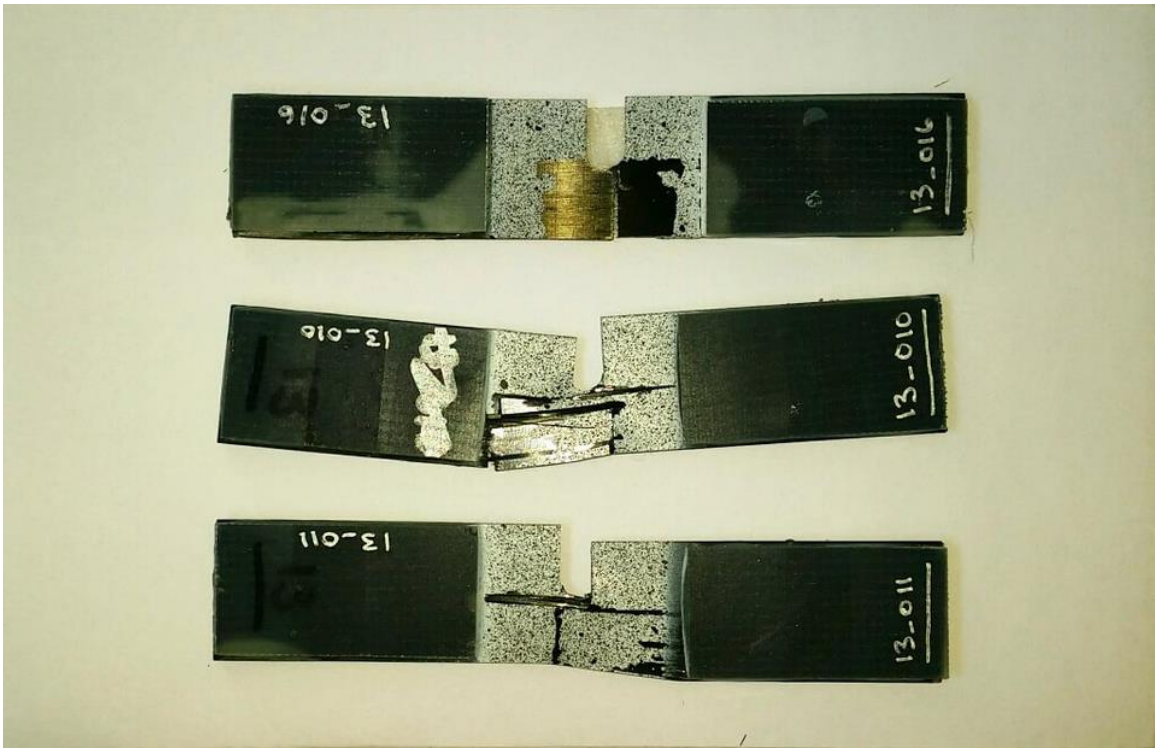

Figure 24. Laminate 13 interesting failures. Written labels correspond directly to the test matrix. For scale, coupon widths are 1 inch or refer to Figure 14 above

Figure 24, above, displays interesting failures of the IM7/8552 specially orthotropic laminate [0/90/0/90]s. This laminate is composed of only two types of layers, 0° plies and 90° plies. Due to this, the failure modes are limited. Matrix cracking usually occurs in the 0° plies at the notch tip; this is expected as there are large shear stresses occurring on these plies, in this location during any kind of tension. Each coupon shoes failures in different ways. Fiber rupture and matrix cracking between fibers are evident on every sample. As These samples typically experience fiber ruptures in large clusters of fibers at the same

location. This is likely due to transverse cracking in the 90° plies progressing into the 0° plies and causing a weakened area. When fibers rupture, stored energy must be distributed and often causes catastrophic failure of the surrounding area.

Figure 25. Laminate 4 interesting failures. Written labels correspond directly to the test matrix. For scale, coupon widths are 1 inch or refer to Figure 14 above

Figure 25 displays several of the interesting failures experienced by the Toray material system's [-45/45/-45/45]s laminate. The top coupon displays a case where the $-45°$ plies experienced fiber rupture. The middle coupon displays large amounts of matrix cracking along the fibers and delamination. Finally, the bottom coupon displays an interesting kink-band looking failure of the $-45°$ plies. Typically kink-band formation is associated with compression; this coupon did, in fact, experience compression due to the

rotational component of the load path. From these images, some information regarding damage propagation and especially final failure can be determined. Furthermore, closer examination such as optical microscopy may be performed to provide more insight.

Digital Image Correlation Results

These results depict only several of many images that may help to inform and, in particular, validate progressive damage models. These images are only still frames from videos which cannot be displayed in this document format. These videos provide data such as test time, loads, displacements, and strains throughout the duration of the test. This duration is the entire test from the start, through damage initiation and propagation, and including final failure if the sample experienced final failure. Even a single image from every sample would prove to be too much to display in this document format and, for this reason, a selected few images from several samples that show interesting damage are displayed.

First, as an example of a single test, there will be three images shown from a single test. These images will include the stage of damage initiation (Figure 26), an intermittent stage of depicting progressed damage (Figure 27), and a stage right before final failure showing damage in its most developed state (Figure 28). The sample that was chosen to demonstrate this was an IM7/8552 quasi-isotropic laminate [-45/90/45/0]s (as tested). Each image will be a report image of the “Major Strain” or maximum principal strain.

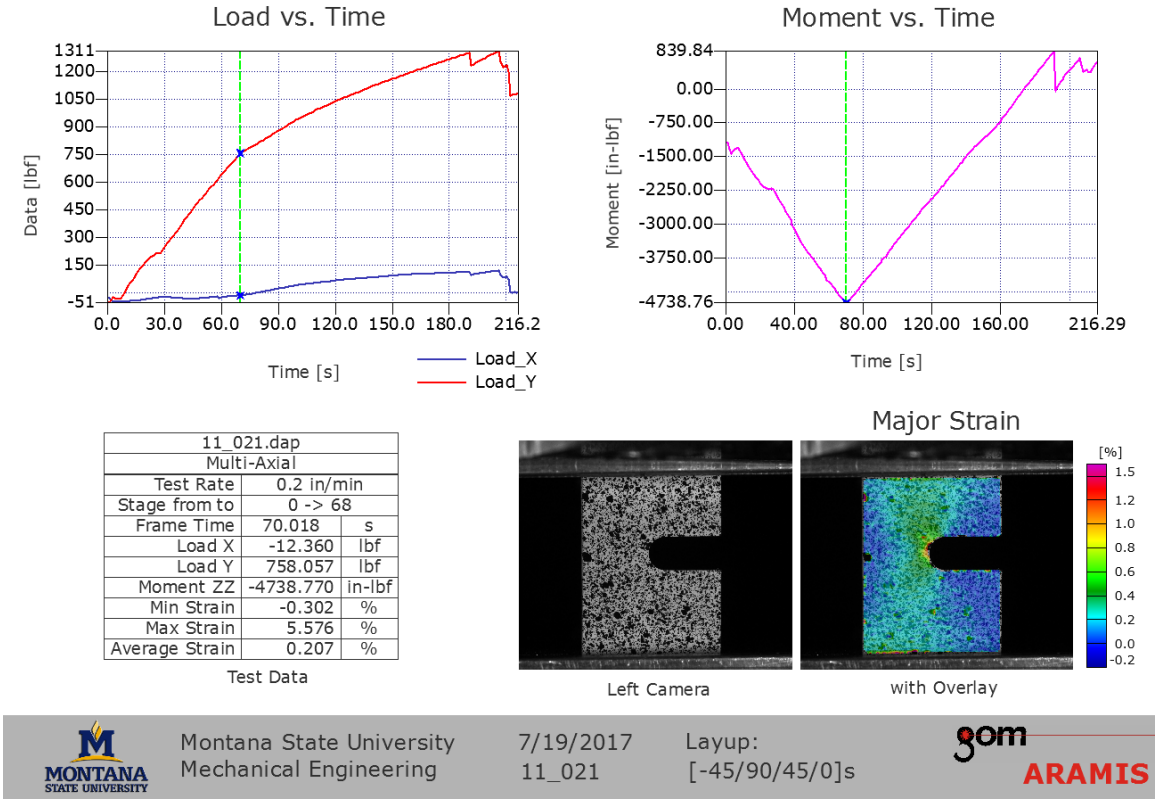

Figure 26. Test 11_021 image of Major Strain report at damage initiation

From Figure 26 above, the major strain clearly shows a higher strain development near the notch tip. From this figure alone, a side-by-side comparison to a model may validate the model if the model produces similar principal strains in the same locations created by the same loads. Not only would this validate the damage initiation of the material but also the constitutive response and the properties input to the model. Furthermore, additional information may be conveyed using the same report format such as $\varepsilon_x, \varepsilon_y,$ or ε_{xy}. Along with this, nearly any information can be conveyed in this format from ARAMIS as long as it is measured by ARAMIS and is not a calculation.

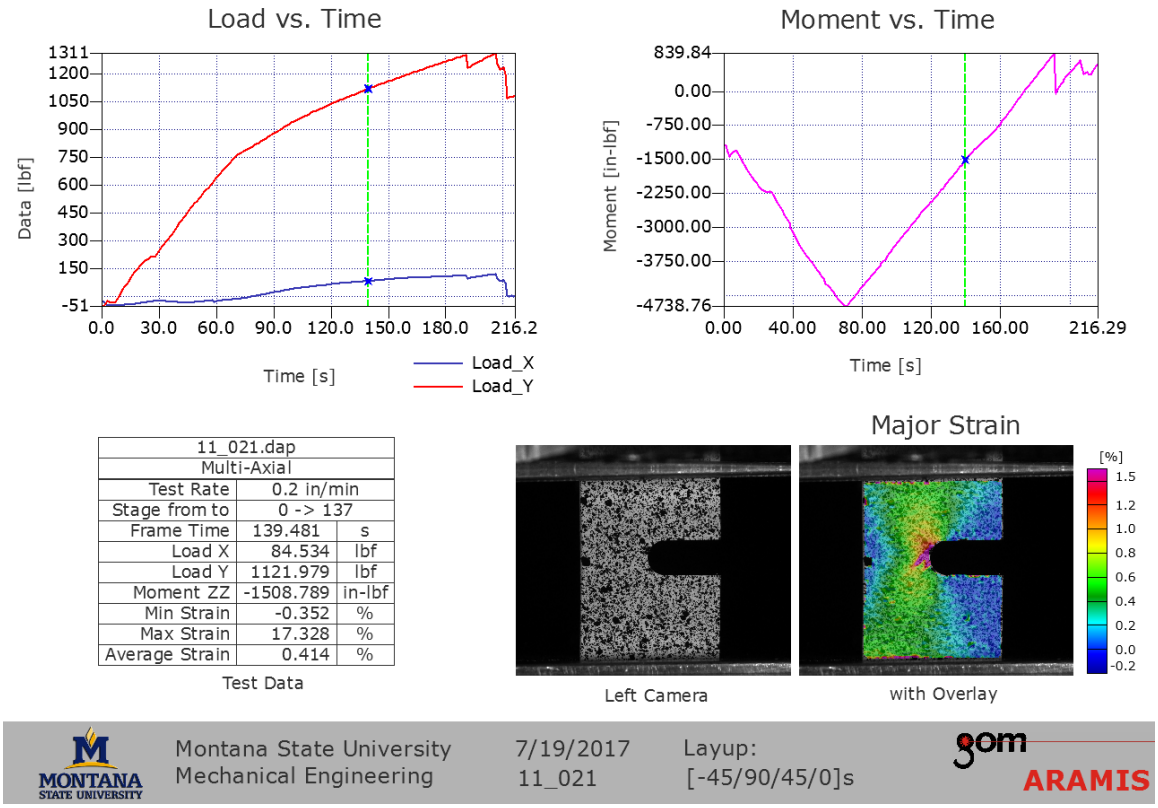

Figure 27. Test 11_021 image of Major Strain report at an arbitrary intermediate damaged state

Obviously, this is an arbitrary intermittent damaged state of the coupon somewhere between damage initiation and final failure. It is clear from the figure that cracking is starting to form on the outside $-45°$ ply and this will become more evident in the next images. Also from this image, where the outside crack is progressing, another high-strain region depicts a crack forming – this is likely due to cracking forming in the 3rd layer in ($+45°$ ply). It *may* also be *assumed* that transverse cracking is occurring in the 90° plies at the same location and that potential delamination has begun. Of course, these images may fail to provide exact failure mode but for the validation and comparison to a finite element model, these may prove satisfactory.

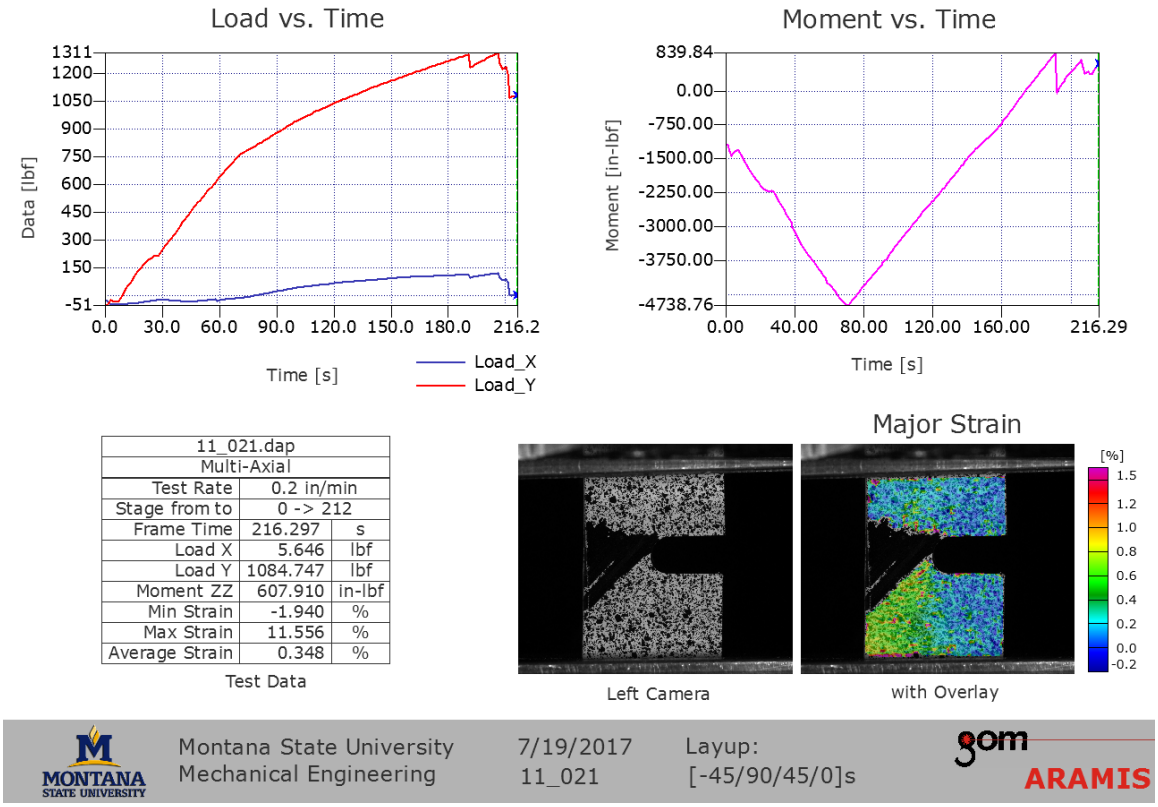

Figure 28. Test 11_021 image of Major Strain report at the stage before final failure

Thirdly, and finally for this example, the coupon has failed. The specimens typically lose paint from the outside surface due to the damage of the coupon itself. This makes for difficult strain measurements on and near this region. However, these images may not be entirely useless as the final failure mode may be evident from this image and much of the data collected to this point provides information regarding when, where, and how damage is working its way through the material. Progressive damage tables such as that shown in Table 5 below are developed from the above ARAMIS images. Complete tables for each laminate and every test are displayed in APPENDIX C.

Table 5. Snippet of progressive damage table as developed from the images above. For the full table and for each laminate, refer to APPENDIX C

Test	Damage initiation			Intermittent Stage			Final Failure		
Name	stage	ply	mode	stage	ply	mode	stage	ply	mode
11_003	101	-45	MC - LNT	128	All	DL	143	0	FR - LNT
11_004	72	90	MC - LNT	84	45	MC - LNT	125	0	FR - LNT
11_005	90	-45	MC - LNT	95	90	MC	107	All	DL
11_006	42	-45	MC - LNT	61	90	MC	153	0	FR - LNT
11_007	58	0	MC	85	-45	MC - LNT	112	All	DL
11_008	62	90	MC - LNT	86	OA	MC - LNT	105	All	DL
11_009	58	45	MC	148	-45	DL	283	All	DL

Each damage mode labeled in Table 5 above is determined solely based on ARAMIS calculations such as major strain (maximum principal strain) direction and the observation of failed samples. The data was then interpreted analytically using the finite element model, which will be described further later. All damage modes included are only damage modes that could be directly observed from the data. For this reason, some listed failure modes were broad and not specifically defined. Abbreviations for the interpretation of the table are as follows:

- MC – Matrix Cracking
    - Cracks begin in the matrix, propagates, and leaves fibers intact. Typically observed as the first damage. High strains and maximum principal strain directions provide information regarding this type of damage. Further details into this mode of failure (such as shear or tension) are not easily determined and therefore not included in the resultant tables.
- DL – Delamination

    - Often interpreted from out-of-plane displacements calculated by the DIC. This failure typically causes final failure for tests with large rotation components as fiber failure is observed for these displacements less often.

- FR – Fiber Rupture
    - Fibers incur damage directly causing fiber breakage. Typically, the "last straw" as stored energy suddenly released into the sample causes catastrophic failure.
- OA – Off Angle Plies
    - All non-zero and non-90 degree plies.
- LNT – Localized at Notch Tip
    - Damage location is confined primarily to the notch tip. If not specified, damage occurs multiple places.
- TG|BG – Top Grip or Bottom Grip
    - Damage is occurring locally at the top grip or bottom grip.

It is important to note, that although digital image correlation may measure and return computed strains, that strain measurements may be inaccurate for representing the entire sample especially through its thickness.

Failure Surfaces

The primary quantitative results of this study are shown below. Again, like the qualitative results, all quantitative results can simply not be shown as there is simply far too much data. As a note, in-plane shear strain values are displayed in figures as percentages. This is unconventional but was performed for visualization purposes and does not have a physical meaning like the normal strains in the x and y directions.

Importantly, the results will undergo a lengthy discussion describing their origins and how they can be interpreted. As seen in the post-processing section, these results are generally displayed as a probabilistic view of strain data. This strain data, again, is taken from an experimental test result at the determined damage initiation stage. This stage is where mechanical damage (material softening) is determined to have started during the test. The DIC processing creates facets over the face of the gauge section and can be treated like elements in a finite element model where each facet has a determined strain state $(\varepsilon_x, \varepsilon_y, \varepsilon_{xy})$. This multiaxial strain state (in-plane strain state) makes up the axes of the figures depicted. An example of an individual facet's strain state is shown below in Figure 29. This data is shown for all facets of all tests of a certain laminate at damage initiation.

As a note, before displaying these results, the displayed failure surfaces are not geometry dependent and may be treated as material 'damage' properties. Even though the coupon geometry was consistent in the creation of these surfaces, the measured data (strains) do not depend on geometry. This is useful as the determined failure surfaces may be useful in the validation or qualification of complex structures that utilize the appropriate laminate-level and perhaps ply-level materials.

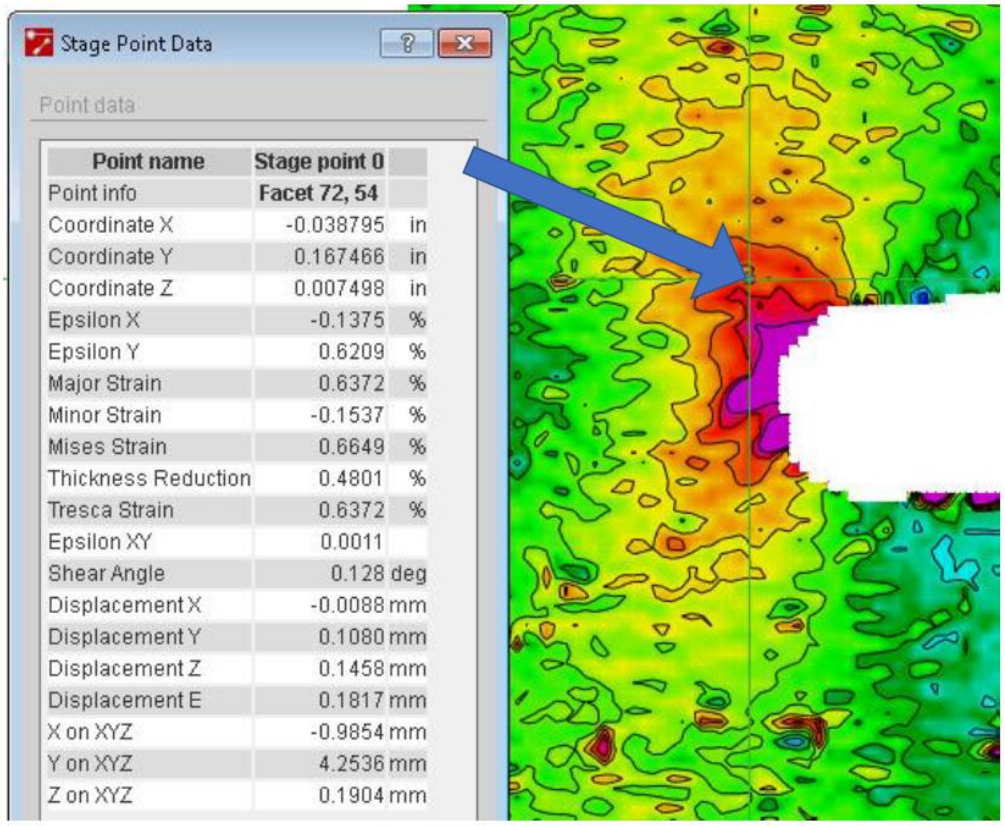

Figure 29. Image depicting a selected facet from an arbitrary test as seen in ARAMIS. "Stage Point Data" displays all facet properties

It has been briefly displayed in the post-processing scheme that a point cloud is created with all of the data for every test of a particular laminate. The stage used from the test data is the stage of damage initiation as determined by dissipated energy calculations. Dissipated energy calculations can detect only mechanical damage and cannot detect physical damage. For this reason, the failure surfaces computed from this point cloud can be treated like the other failure criterion mentioned previously that predict the onset of mechanical damage/ material softening. However, since these calculations only account for mechanical change, it is important to note that other methods must be used if an understanding of physical damage is desired.

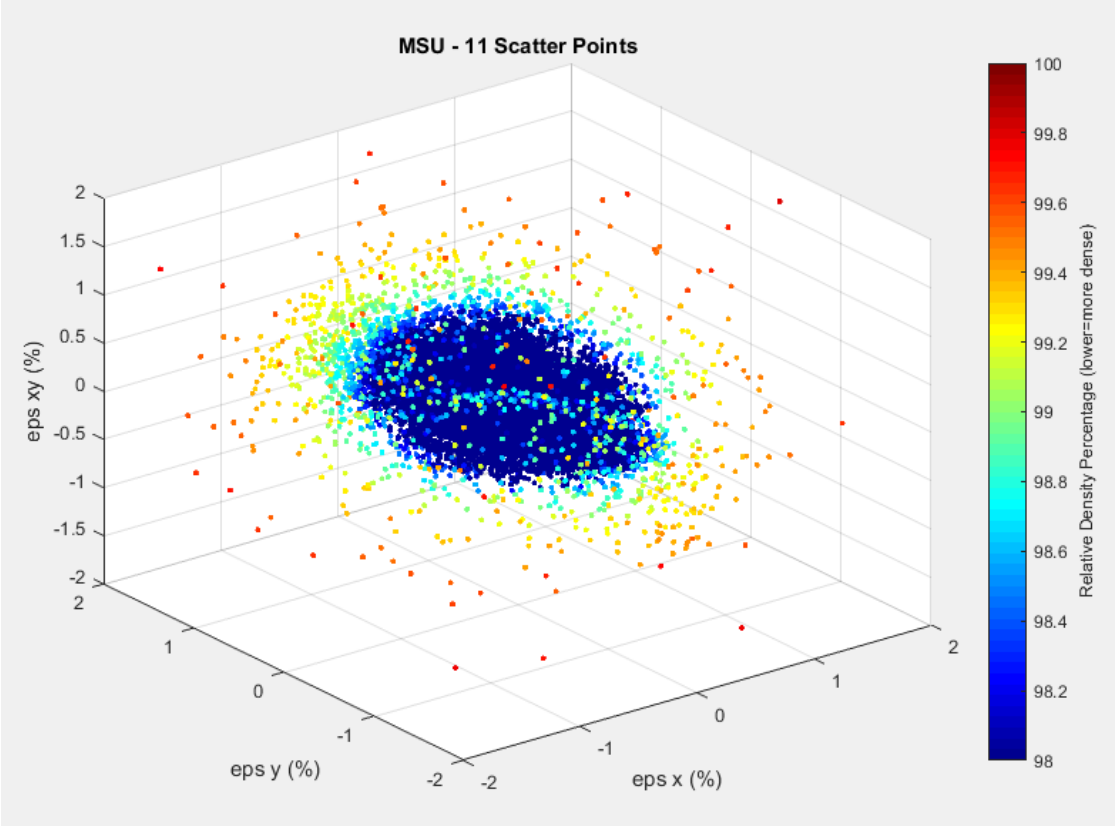

Figure 30. All in-plane strain data points collected for MSU - 11 tests. This includes all tests displayed in the test matrices

Figure 30 above is a demonstration of what the point-cloud looks like. This was shown briefly in the post-processing scheme but is more clear by itself. There are three axes defined by the in-plane strain $(\varepsilon_x, \varepsilon_y, \varepsilon_{xy})$ of each individual facet. After going through much of the post-processing scheme, these data points can be shown based on their where they lie in the cumulative probability distribution. From this, isosurfaces can be created and shown based on these assigned values (shown as colors above). Notice the color bar scale ranges from 98% to 100% and the inner-most points are packed so tightly that approximately 98% of the data is not worth showing relative densities. The isosurfaces created from this figure are shown below in Figure 31.

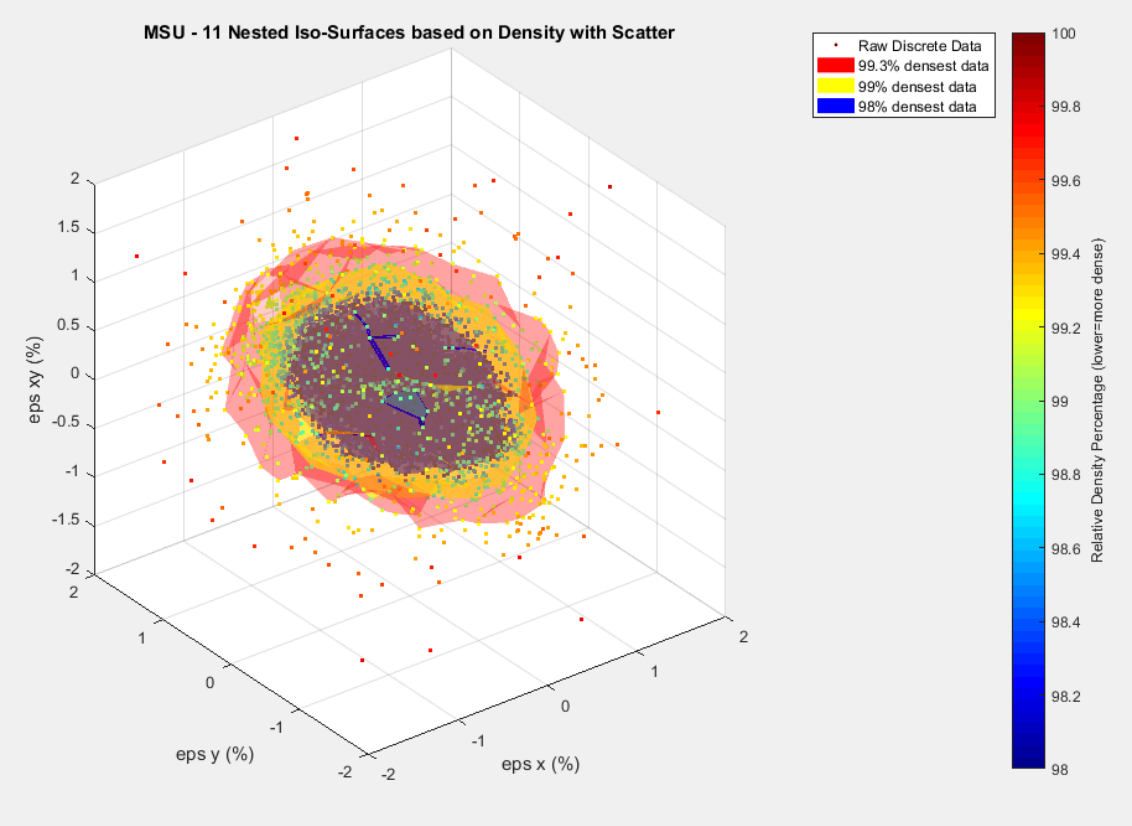

Figure 31. MSU - 11 nested isosurfaces defined by data density. Scatter points are also shown for reference

From Figure 31, it can be further seen that data density increases drastically. Three separate isosurfaces have been created and displayed; as an example, the red isosurfaces labeled '99.3% densest data' in the legend means that 99.3% of all MSU-11 strain data lies on or within this enclosed surface. This is useful to create "failure surfaces" analogous to failure criterion but, again, are based on experimental data. All failure surfaces displayed are defined by the onset of damage, not final failure. Since these are truly measured data from experimental tests, the material has experienced these strains without accumulating

mechanical damage[‡‡]. Probabilities are used to define these nested isosurfaces to isolate outliers caused by error in digital image correlation measurements as well as create different "layers" that offer different levels of conservativeness.

These nested isosurfaces can then be displayed based on how they look on each primary plane. For the sake of brevity, only Figure 32 below will be shown in detail and the remaining "slices" will be displayed at once in Figure 33. This is only an example for the IM7/8552 quasi-isotropic laminate (MSU – 11). These "sliced" views are similar to existing failure criteria but do not have any reliance on analytical assumptions. The three nested "levels" are shown to illustrate the different levels of conservative criteria.

Since these surfaces are analogous to failure criteria, different levels of conservativeness will be described in terms of failure criteria. As shown previously, interacting criteria are typically more conservative than maximum stress and maximum strain criteria in areas where combinations of stresses occur. This is due to the "rounded" shape of the interacting criteria. Like these criteria, the different levels of isosurfaces are displayed for the sake of conservativeness/ conservation. The blue inner surface displays the most conservative surface based on the densest data and the smallest failure volume. The red outer surface displays the least conservative surface as it allows less dense data to define a larger failure volume. The smaller the volume in strain space, as displayed, the more conservative the failure surface. This will be discussed further in the conclusions portion to follow.

[‡‡] Mechanical Damage – There are generally two types of damage: physical and mechanical. Physical damage is typically damage like micro-cracking that does not affect mechanical properties of the material. As physical damage develops further, larger cracks are formed that affect mechanical properties of the material – this is mechanical damage.

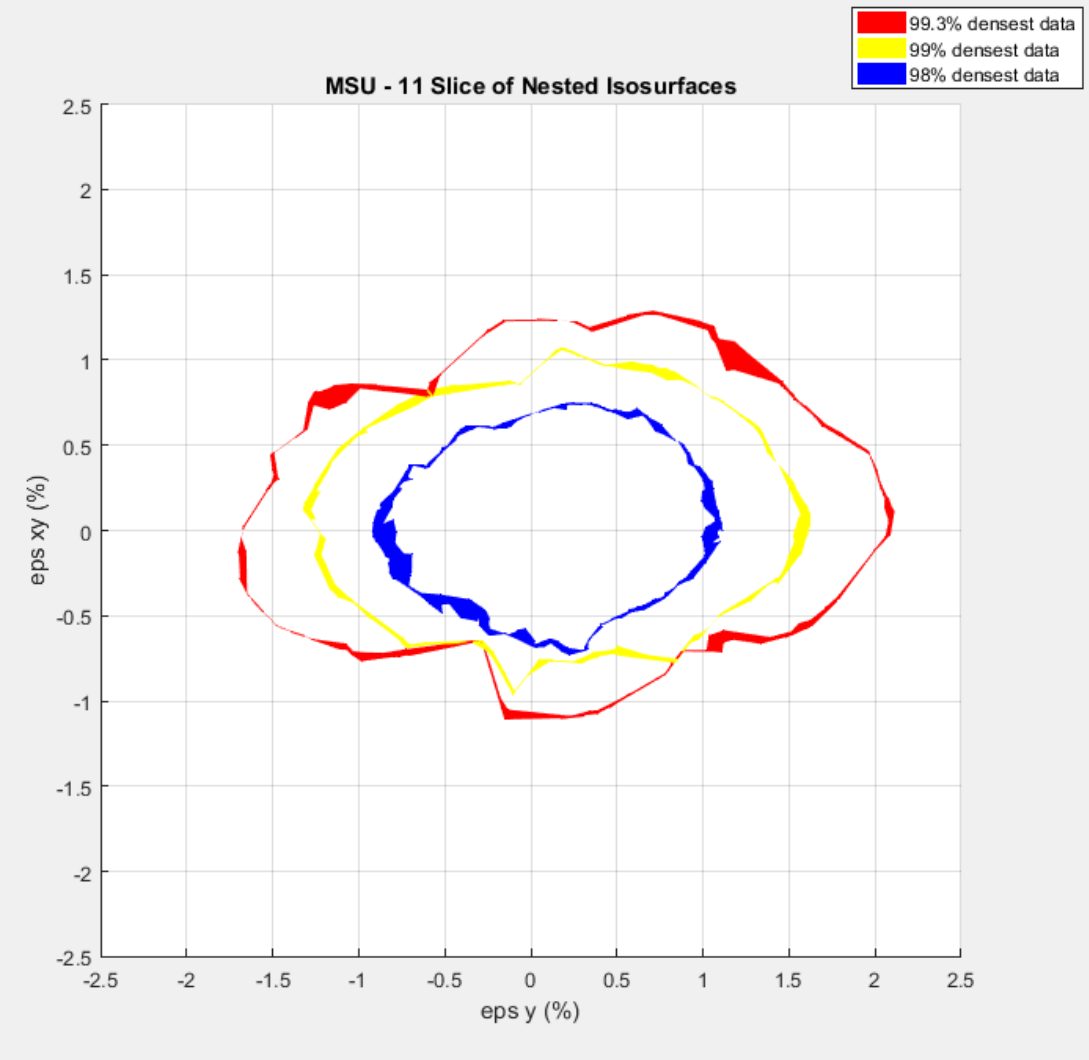

Figure 32. Example of nested isosurfaces displayed on the eps x = 0 primary plane

To reiterate, as described in the post-processing scheme, these surfaces are generated based on measured strain states of mechanically undamaged coupons (where no mechanical damage has occurred). The data used to define these surfaces is taken at the last undamaged state of the material during the test. In theory, disregarding outliers of digital image correlation error, the material can experience these strains without incurring mechanical damage.

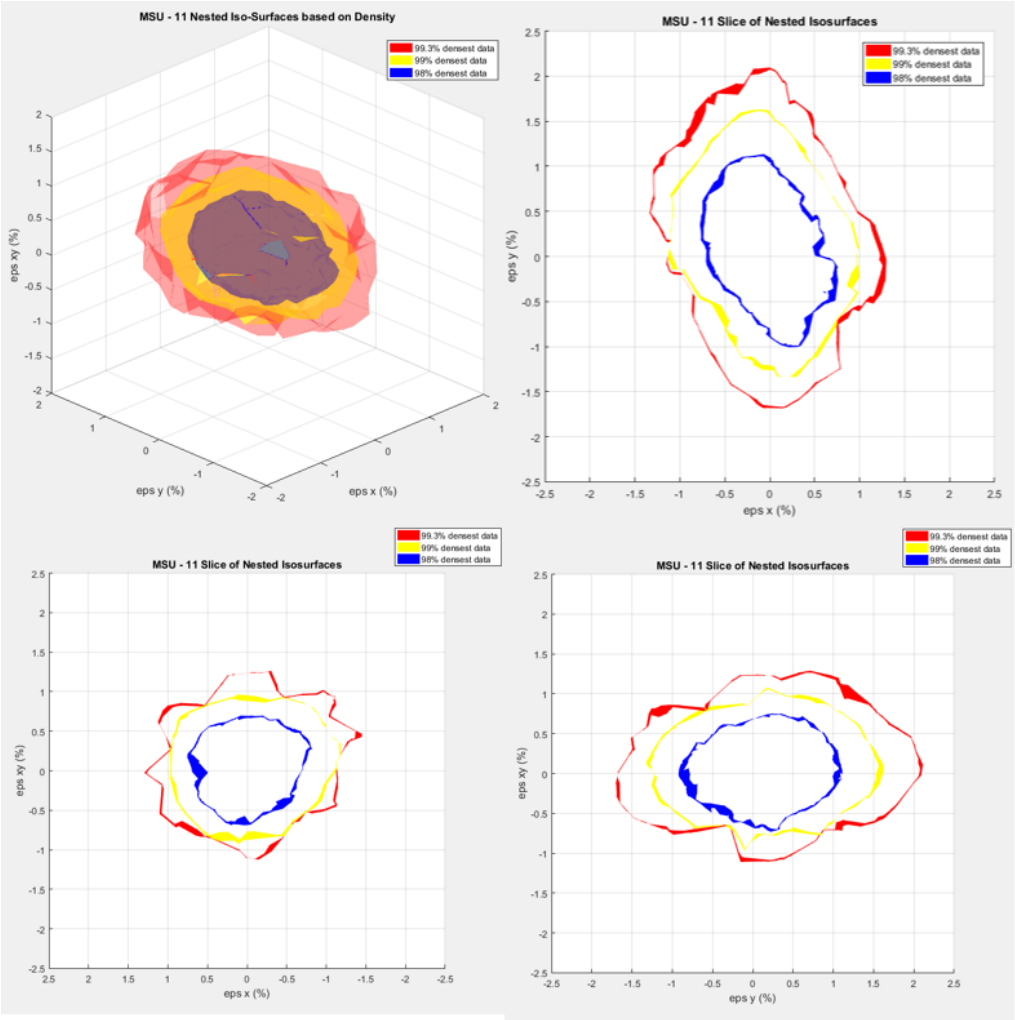

Figure 33. Nested isosurfaces for MSU - 11 displayed on each primary plane. Original nested isosurfaces (top-left). Primary plane eps xy = 0 (top-right). Primary plane eps y = 0 (bottom-left). Primary plane eps x = 0 (bottom-right)

As shown, these surfaces are material failure predictive surfaces with different levels of conservation. The results above only pertain to the laminate as a whole and should not be considered representative of any laminate other than the IM7/8552 quasi-isotropic laminate it was derived from. Also, these surfaces should not be considered representative of individual ply properties on the described 1, 2 and 12 planes. These figures have been generated for every laminate in this study.

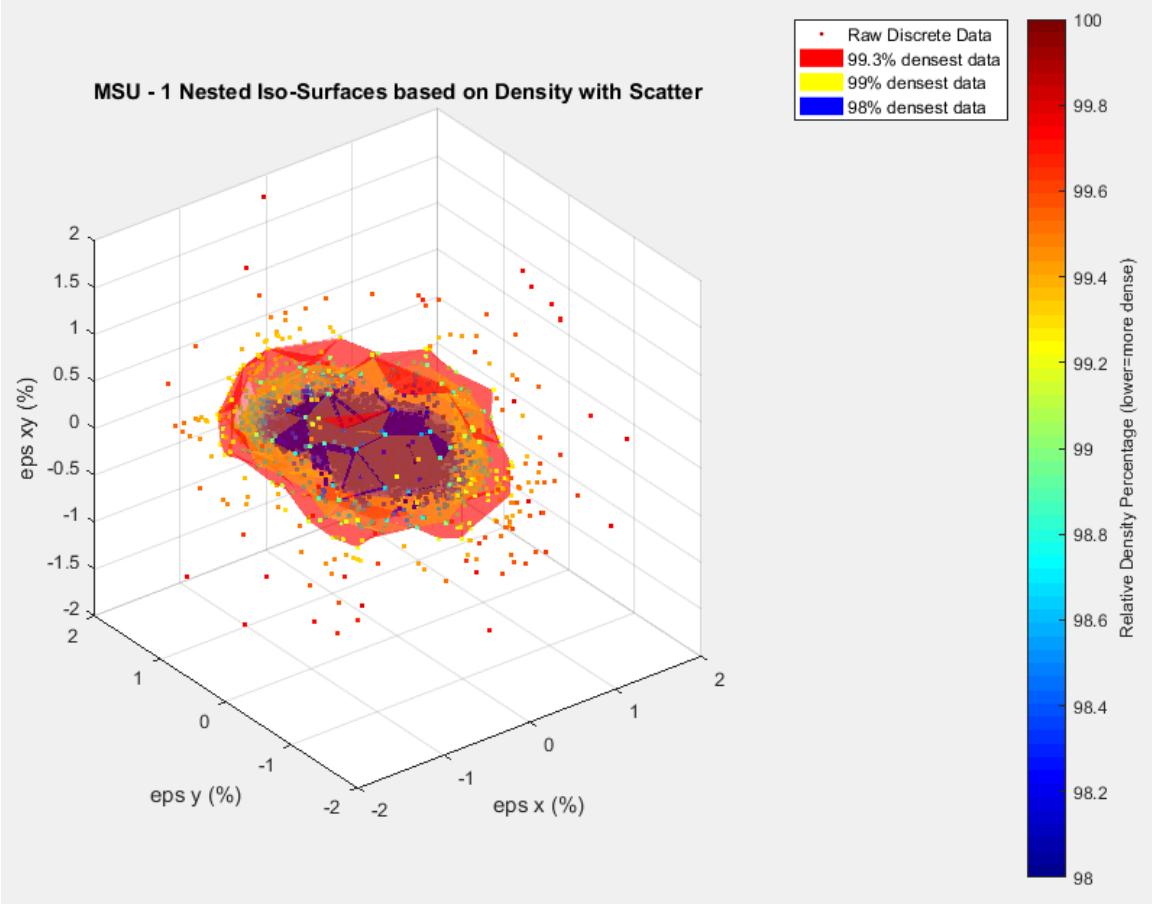

Figure 34. MSU - 1 nested isosurfaces defined by data density. Scatter points are also shown for reference

To aid in demonstrating the differences between the two material systems, Figure 34 above displays the result for the Toray material system's quasi-isotropic laminate. This figure was created with nearly as many tests as the IM7/8552 material system as well as the same test load paths. This figure is to be compared to Figure 31 above (the IM7/8552 version of the laminate). As shown in Table 3, these laminates share the same stacking sequence but are composed of different ply materials.

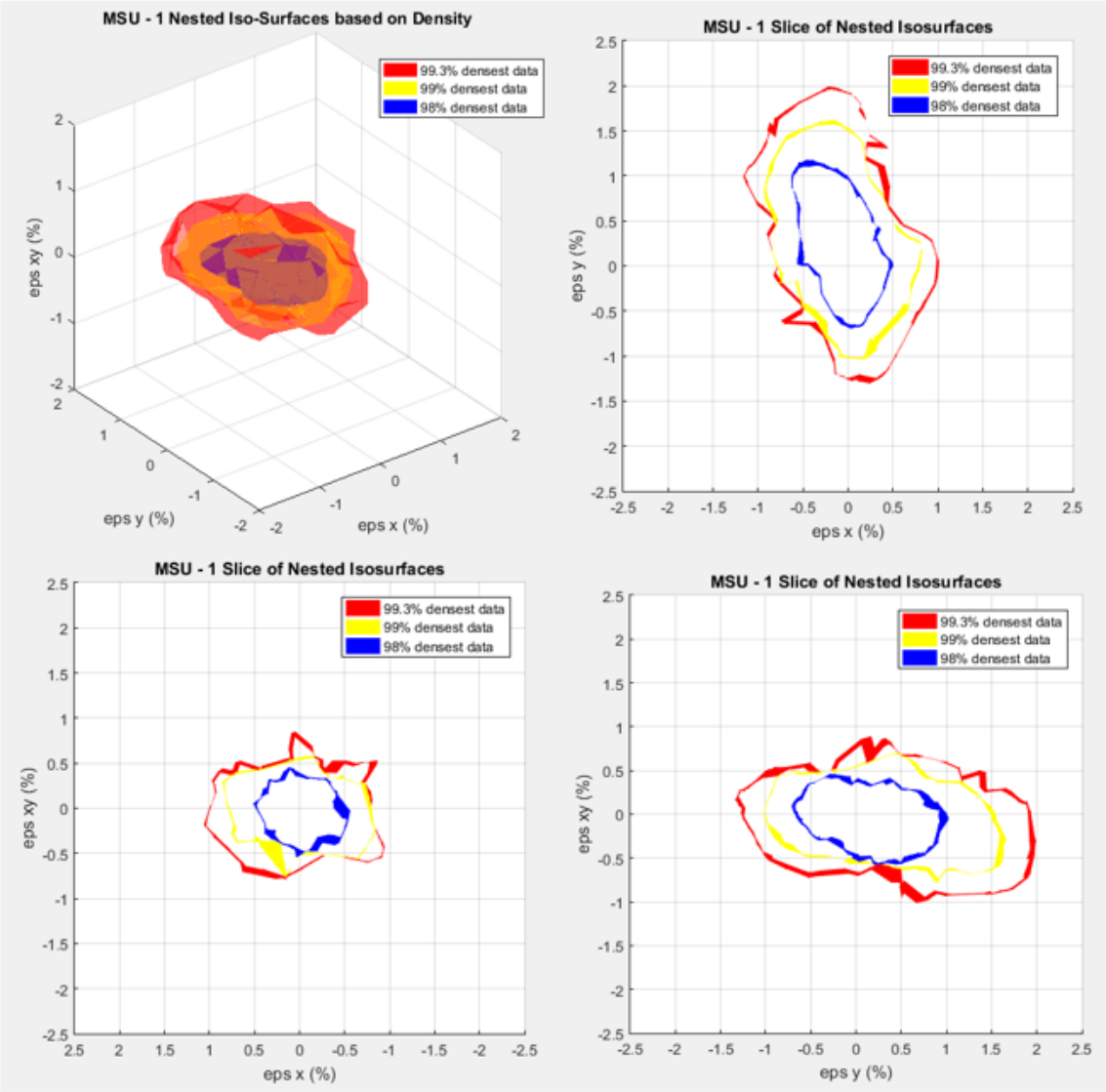

Figure 35. Nested isosurfaces for MSU - 1 displayed on each primary plane. Original nested isosurfaces (top-left). Primary plane $\varepsilon_{xy} = 0$ (top-right). Primary plane $\varepsilon_y = 0$ (bottom-left). Primary plane $\varepsilon_x = 0$ (bottom-right)

Furthermore, these isosurfaces can be compared with each other side-by-side based on how the surfaces intersect the primary planes. Figure 35 above shows the Toray material system's quasi-isotropic laminate isosurfaces "sliced" and viewed on each plane. This figure is to be compared to Figure 33 above which, again, where the same image for the

IM7/8552 material system is shown. Furthermore, Figure 36 below shows this comparison further. The difference between the two material systems is evident by the isosurfaces displayed. It is understood that the Toray material system is more brittle than the IM7/8552 material system and this is evident from comparing the experimental failure surfaces created. The Toray material system results in a smaller overall volume and the isosurfaces do not extend as far as the IM7/8552 system's. This demonstrates that the Toray material system, in general for this laminate, does not reach as high of strains before the material experiences failure.

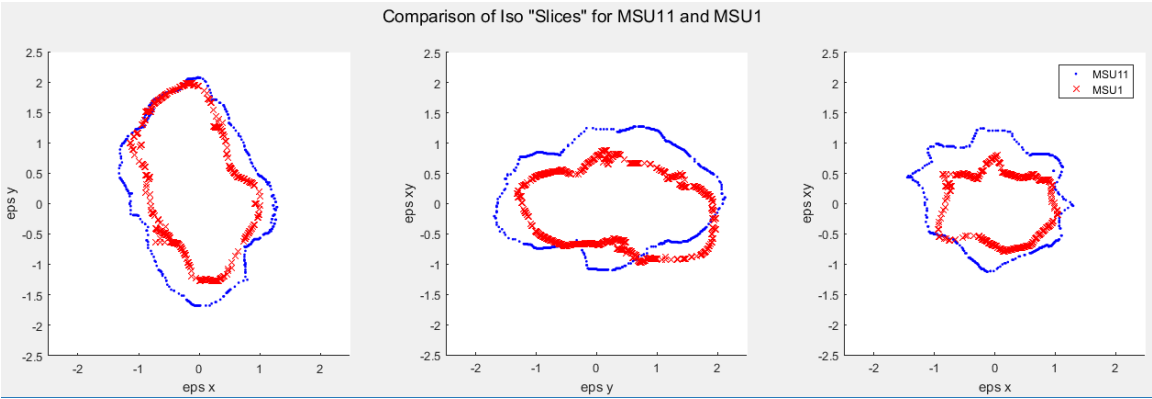

Figure 36. Direct comparison of MSU - 11 tests (Figure 33) shown in blue and MSU - 1 tests (Figure 35) shown in red

As discussed at the end of the post-processing scheme section, data was then transformed into local ply coordinates. This produces strain results that pertain to each material system ply-level. Before displaying results, it is important to reiterate that the following results may have errors due to the assumption discussed in the post-processing section. Figure 37 and Figure 38, below, show the ply-level results for the Hexcel IM7/8552 material system and the Toray material system respectively.

As a note, the results obviously differ from the results provided above for the laminate-level failure surfaces. This is mostly due to the size of the data after it was transformed and collected for each material. The resultant data set was so large that it would take approximately 70 hours to process each. So, as a result, the “raw” point cloud is shown without weights in the top left of each figure which doesn’t provide much insight about the material without, again, taking these “slices”. The “slices” are also displayed in each figure with a slightly different format than previously shown but equally as useful.

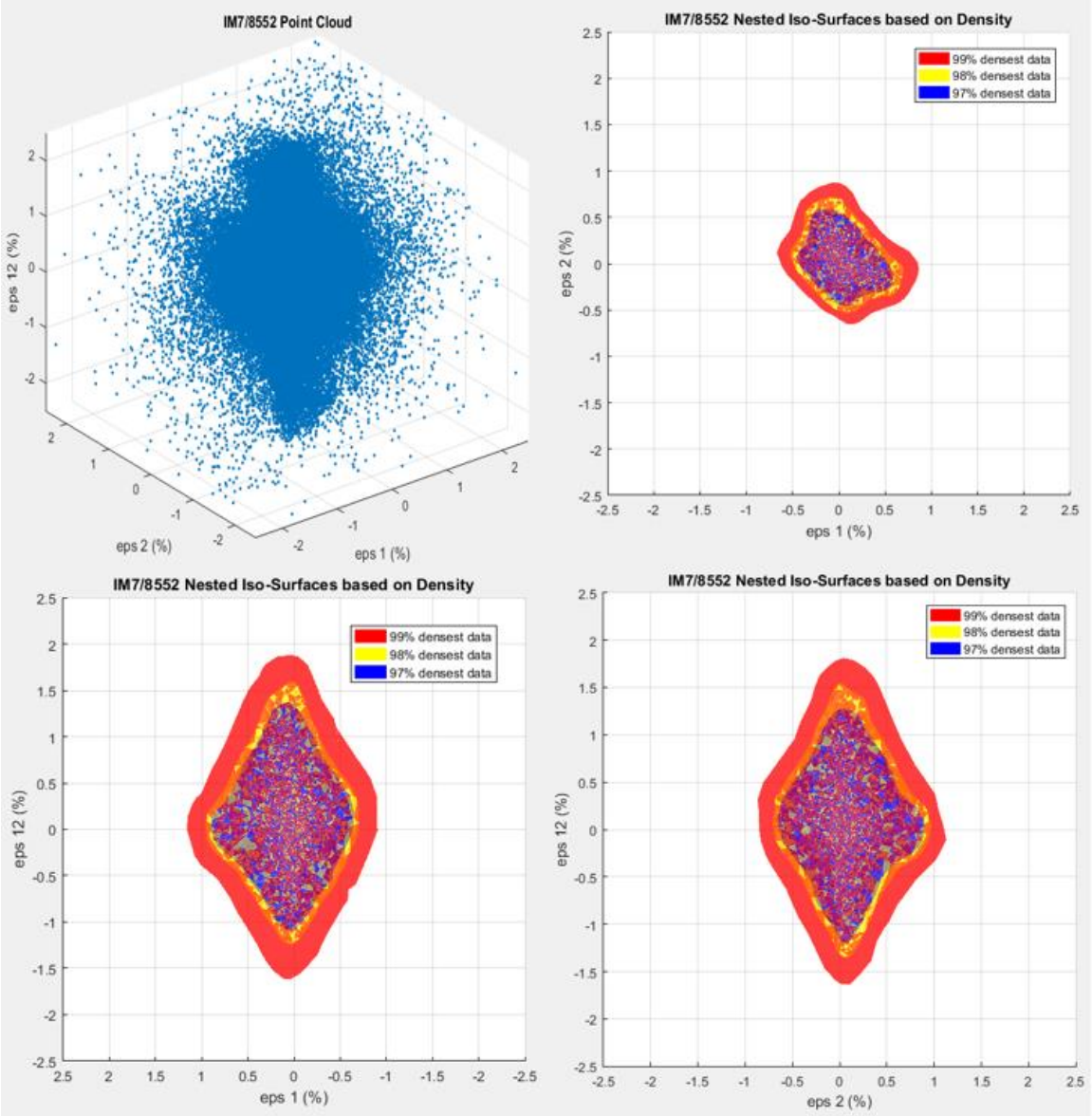

Figure 37. Ply-level "failure surfaces" produced from original point cloud of the Hexcel IM7/8552 material system transformed and resolved into each ply's local coordinate system. Original point cloud (top-left). Primary plane $\varepsilon_{12} = 0$ (top-right). Primary plane $\varepsilon_1 = 0$ (bottom-left). Primary plane $\varepsilon_2 = 0$ (bottom-right)

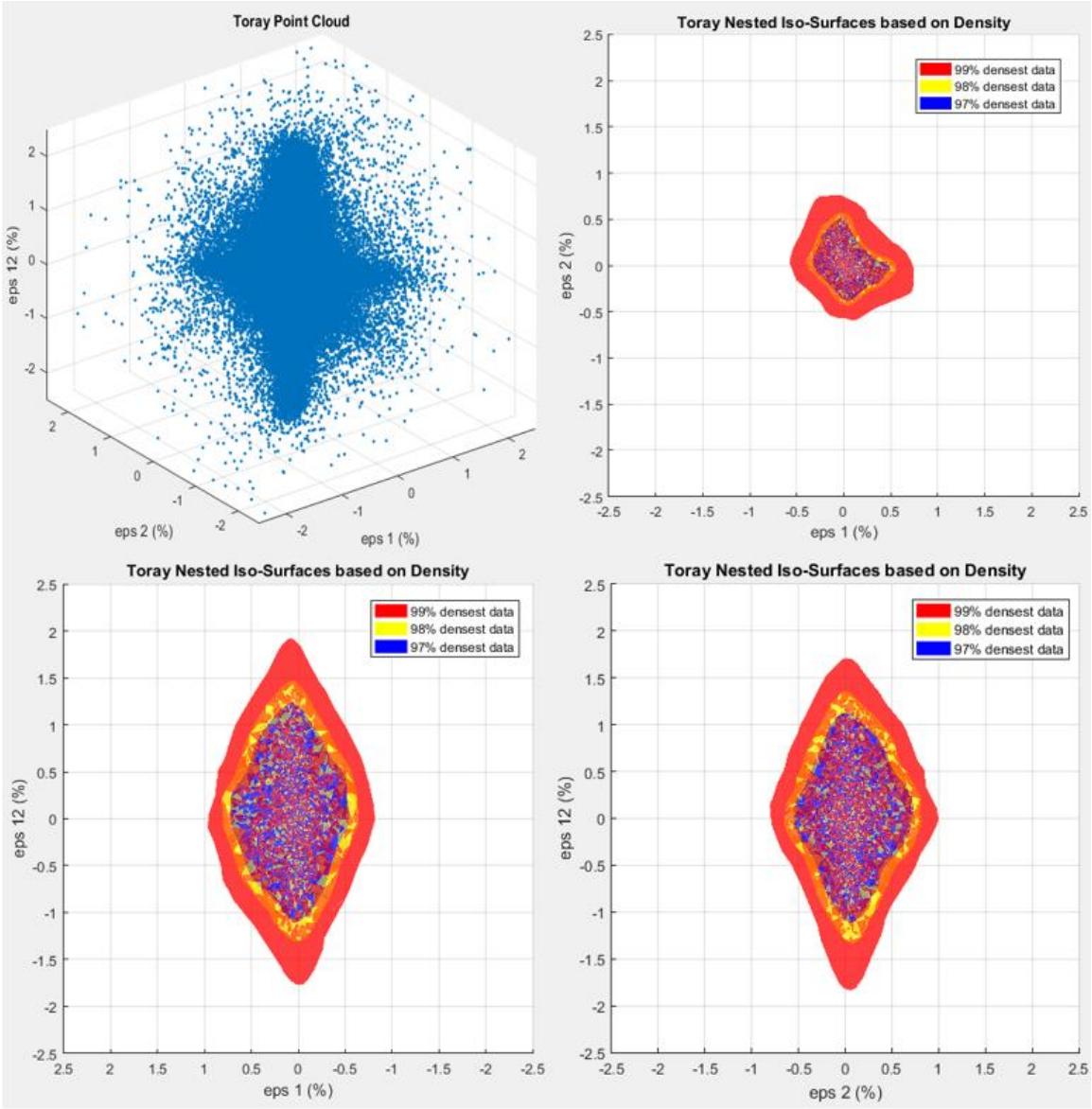

Figure 38. Ply-level "failure surfaces" produced from original point cloud of the Toray material system transformed and resolved into each ply's local coordinate system

FINITE ELEMENT MODEL

Model Definition

This section will focus on the definition of the finite element model developed using ANSYS Workbench. It is important to note that although the data from this research is to inform and validate progressive damage models, the following model is not a progressive damage model. The model to be described is a linear elastic model created only to aid in experimental data interpretation. This model is important for two reasons. First, if a linear elastic model can produce results resembling a test up to damage initiation then the next step can be taken to produce a model that can compute damage. Without first confirming a simpler model, attempting to model more complex behavior would be moot. Second, and to be discussed further later, the following model will act as a supplement to experimental data where the ARAMIS DIC falls short.

As discussed briefly in the Experimental Data section, edge facets computed by DIC are often inaccurate or impossible to calculate. This is due to the lack of boundary definitions for these edge facet (again, similar to elements). Without accurate references to define these "element" boundary conditions, the displacements, and therefore strains, are impossible to accurately compute. So, as stated above, this finite element model supplements digital image correlation data by allowing a representative model accurately compute strains of elements close to edges. Data processed further will include all strains at node locations which allows for strain "measurements" on the edges of the model. Also, for this reason, the model has been created with smaller elements around the notch tip to provide higher-resolution information near this area of interest.

Model and Layup Setup

ANSYS Workbench is actually just a graphical user interface to ANSYS APDL that provides extra tools and "modules" to be applied to the model. Therefore, logically the workflow of Workbench operates the same way as APDL. This can be shown graphically from the top-level view of Workbench shown in Figure 39 below. Each module included in the model design tree serves a different purpose. ANSYS Workbench was chosen as it provides all features available in APDL as well as tools not included directly in APDL. Workbench also offers robust automation ability which is useful for replicating many tests using identical input and output formats. Again, for the sake of completeness, each module will be discussed in detail below.

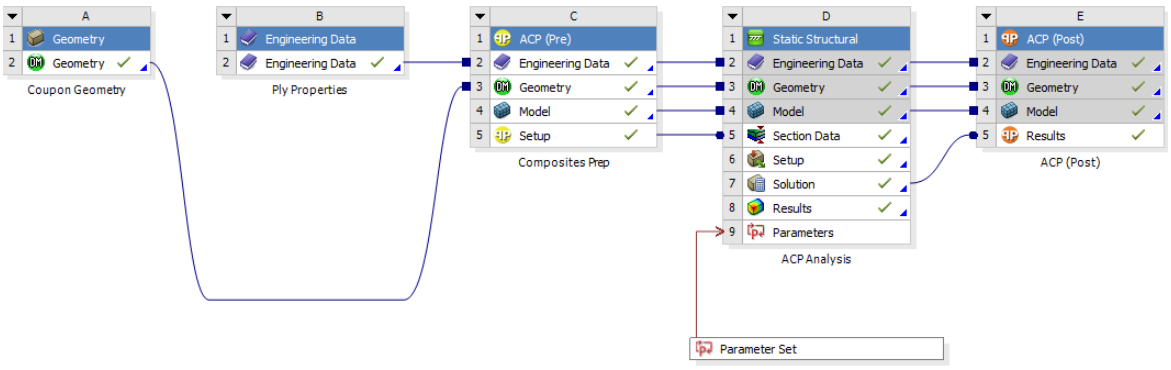

Figure 39. Top-level view of ANSYS Workbench model

Module A. Geometry. The geometry construction of the model is made to mimic geometry of experimental coupons minus the grip areas. Therefore, only the gauge section was modeled as this was the area of interest. The model geometry and mesh result can be seen in Figure 40 below. The mesh is refined around the notch to provide higher resolution

data as the notch is the primary area of interest. The coordinate system displayed matches the coordinate system applied to each experimental sample within ARAMIS software; this is to maintain continuity between the model and experimental data.

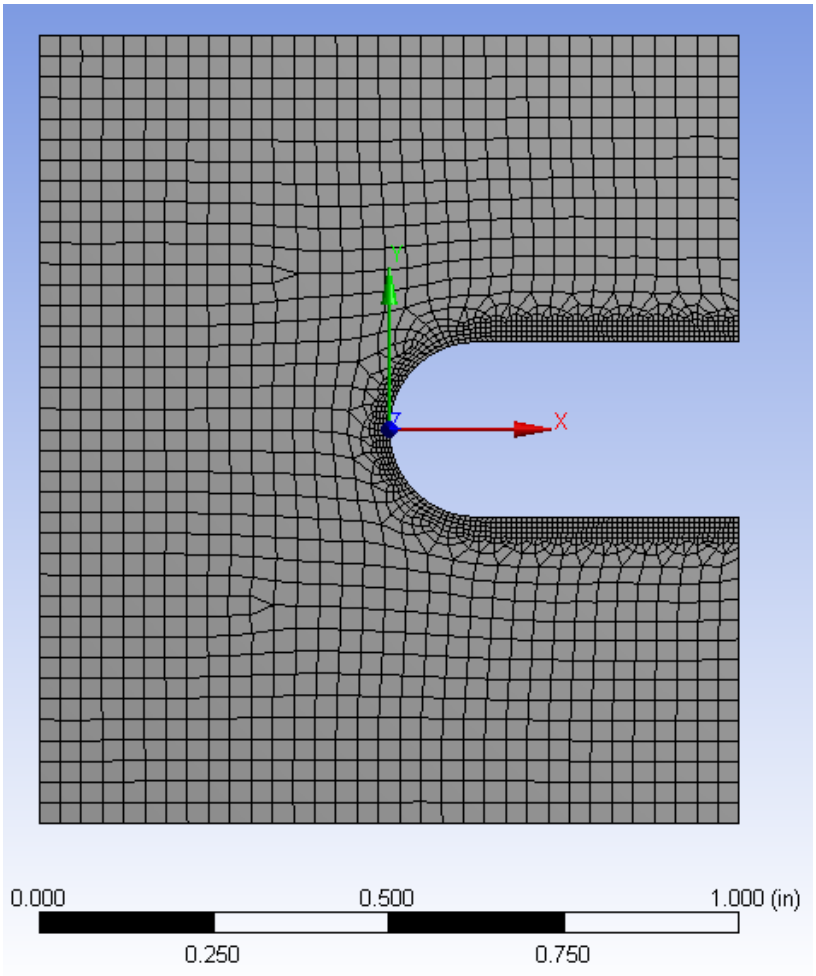

Figure 40. Model mesh definition with coordinate system shown

Module B. Engineering Data. The engineering data module supplies material property data to the model. Here is where the properties displayed in Table 1 and Table 2 (shown previously on page 48 and 49 respectively) are applied to the model. The next

module uses the material properties of individual plies to create each ply of the coupon separately. Unlike some linear elastic mechanical models of composites, this method does not require so-called “smeared properties” to be applied and is more robust as each ply is handled separately.

Module C. ACP (Prep). As mentioned above, each ply (layer) is handled separately within ACP (Prep). This allows for the creation of shell elements representing individual plies rather than solid elements with smeared properties that may be less accurate. Figure 41 below shows the distinction of individual ply elements applied to the geometry. Most of the basic functions ACP (Prep) offers were used in the creation of this model including the ability to define ply orientation, material thickness, coupling properties, strength properties, and element set definitions.

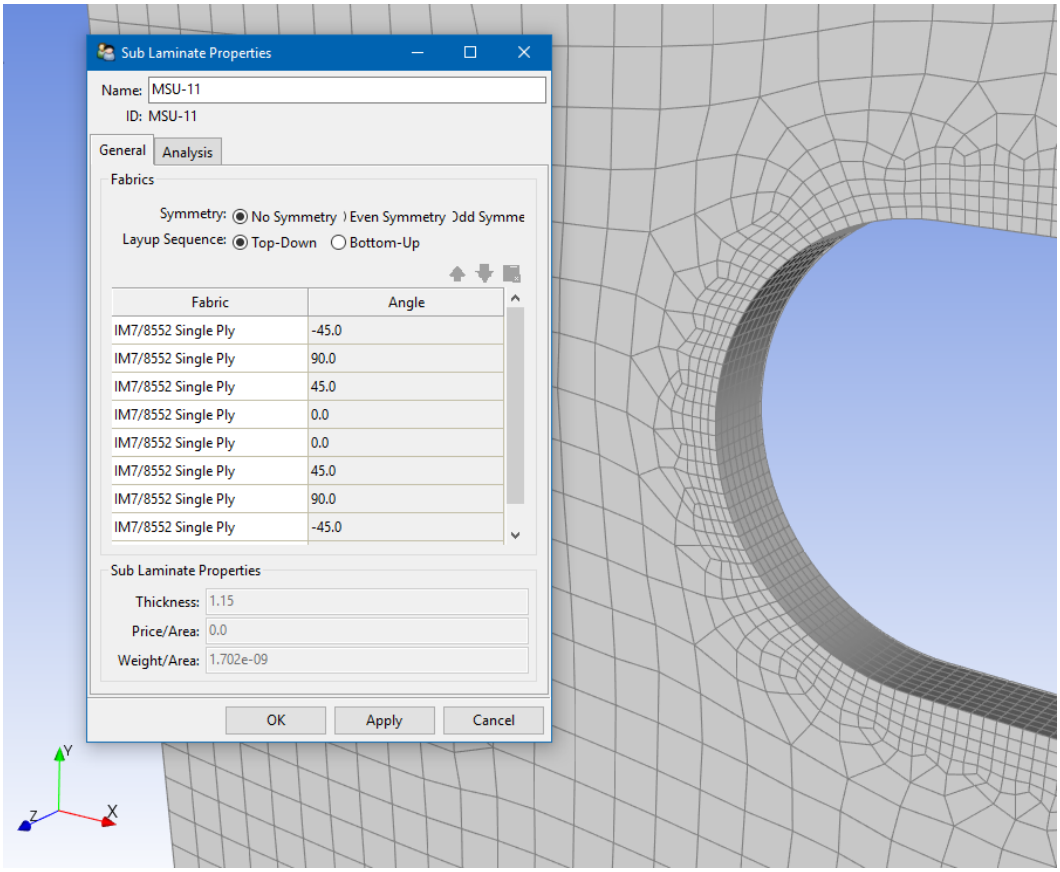

Figure 41. ACP (Prep) figure showing ply layer definition, coordinate system, and distinction of elements through the model thickness

Although not used in this model, ACP (Prep) also allows the creation of composites comprised of many materials in any configuration, e.g. foam-core box beams or wind turbine blades. Another advantageous feature is the definition of ply-drops and draping coefficients for complex structures.

Module D. Static Structural. This is the main module that handles boundary condition setup, solution and result information. This module gathers all inputs from previous modules, inputs them into APDL, continues APDL setup, and finally solves the

APDL code. At any point in the design tree of 'Static Structural', manually edited APDL code such as element definitions and export scripts can be added.

To solve a file in 'Static Structural', boundary conditions must be applied, and desired solution information must be defined. The boundary condition setup is identical to the schematic shown previously in Figure 3. Boundary conditions applied to the model and the assumptions made are explained fully below.

Solution and results information can be displayed on a nodal or elemental basis for nearly any desired result. Solution result sets for this model are handled outside of ANSYS and are exported as text file. The process for the use of solution information from the model is described further below.

Module E. ACP (Post). Appropriately named, ACP (Post) is the post-processor side of ACP. ACP (Post) imports solution information from the 'Static Structural' module and makes further calculations. This module does not model damage in any way but may be a useful tool for preliminary failure calculations. Elements are analyzed individually in ACP (Post) and user-defined or built-in failure criteria can be applied to each element. For example, Maximum Strain failure criterion can be applied to the model and each element's "failure prediction" based on the applied criterion can be displayed. The image shown in Figure 42 is an example of Maximum Strain applied to an arbitrary simulation. This module was used in the aid of producing data displayed in the APPENDIX B.

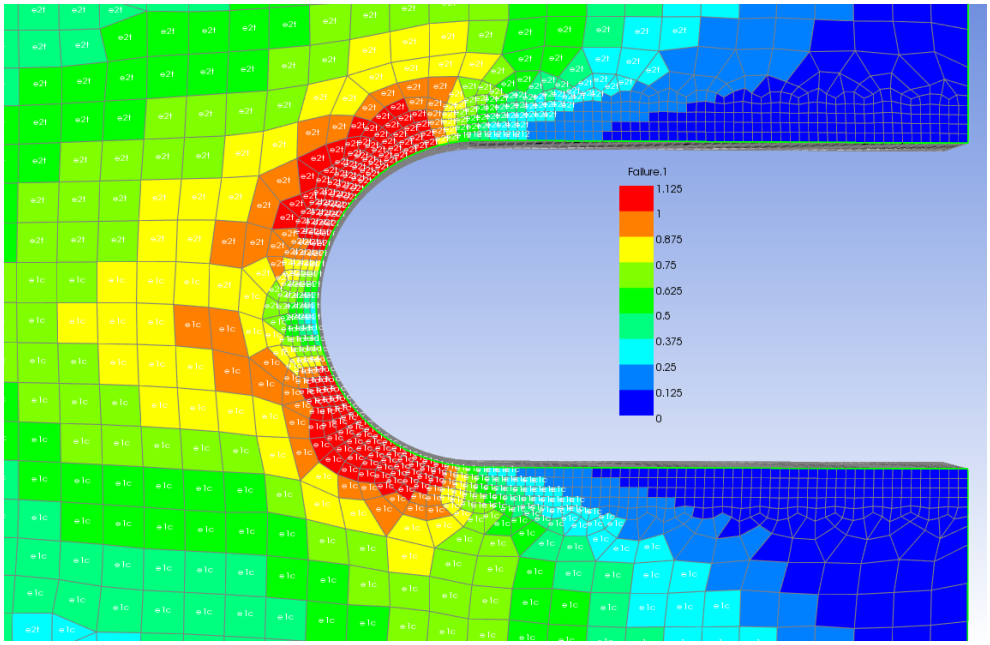

Figure 42. ACP (Post) example of failure display using Maximum Strain criterion of an arbitrary simulation. Image only displays predicted failure for selected layer (surface layer)

Parameter Set. The parameter set module provides a means of accessing and changing numerical or script variables within 'Static Structural' without the need to access the full 'Static Structural' module. This feature was used for automation purposes and will be explained more below.

Boundary Conditions

As mentioned above, boundary conditions are applied in the 'Static Structural' Module. The bottom boundary is defined as a 'fixed-rigid' boundary condition. The top boundary is defined as rigid but allows for both x and y component displacements and rotation "about z". The rotation component is applied to the centroid of the boundary and therefore rotation is defined to rotate in the x-y plane about the top-center of the coupon.

Rigid behavior for each boundary condition simply restricts deformation of the boundary it is applied to but allows rigid body displacement. Figure 43 shows an example of "pure" mode displacements applied to the top of the coupon.

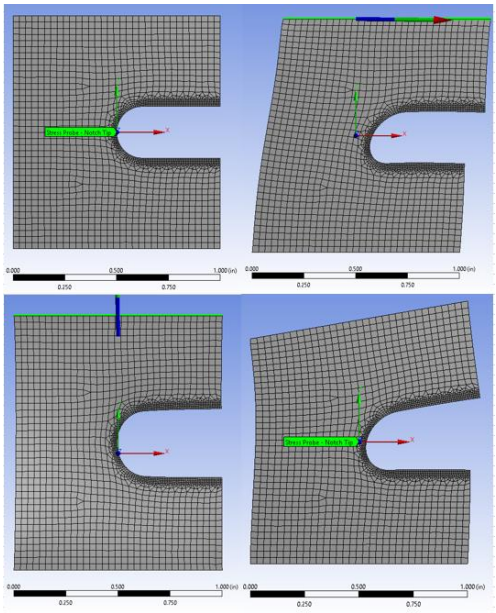

Figure 43. Example of Displacements applied to top boundary condition in ANSYS finite element model. Undeformed (top left), Positive x-displacement (top right), Positive y-displacement (bottom left), Positive rotation (bottom right)

Model Assumptions

There are several assumptions made in the model that must be addressed. Assumptions are made to simplify complex systems to a point that they can be understood; but, as a result, these simplifications are often not realistic and may cause errors in calculations and ultimately errors in understanding. In a way, finite element models are by nature an assumption and should be treated as such. To avoid irrelevant and improper conclusions from this work, the primary assumptions of the finite element model are listed and briefly discussed below.

- Linear Elasticity – Discussed briefly above, the model used is a linear elastic model and may not "well" represent the material. It is generally accepted that CFRPs are not linear elastic in nature especially after damage initiation [9]. However, there is evidence to support that there is a non-linear elastic response prior to damage initiation [3]. Without "exact" material constitutive properties, non-linearity included, models may stray from good representation of their experimental counterpart.
- Constant Strain through the Thickness – This assumption is also made for the experimental data up to but not after damage initiation. It is assumed strains on the surface of the sample are representative of the strains through the thickness (each ply experiences the same strains). This is applied in the model by tying nodes together. This assumption was made since it simplifies, reduces degrees of freedom within the model, and ultimately reduces computation time required to solve the model.
- Rigid Boundary Conditions – This is assumed for the model and is a reasonably realistic assumption. Schmitt [14] explored whether or not rigid boundary conditions were appropriate to apply and concluded that there was no significant change in the solution between the two methods. Physically, if this assumption were to be applied to an experimental test, it would mean that the sample is perfectly gripped.

Processing

This section will briefly describe the processing procedure of the finite element modeling data. This post-processing scheme is nearly identical to the procedure described in the experimental data portion of this report and will therefore be summarized with primary differences elaborated. However, making the model resemble a real-life test requires much setup aside from the model-definition setup. This is described briefly below:

1. Data is exported from ARAMIS into usable files. This is the same as step 1b from the experimental post-processing scheme. Files are stored for each individual stage and include undeformed and deformed facet displacement data as well as strain data.
2. From these files, created in step 1, boundary conditions are directly measured from the sample's face via ARAMIS calculations. This step ensures that boundary conditions applied to the model are, in fact, boundary conditions measured directly from the sample during the test. It is only necessary to reproduce the test as soon as damage initiates and this process will use this stage.
    a. Results data is imported to MATLAB and is filtered for the top boundary condition and bottom boundary condition facets based on facet location in the undeformed configuration. An example of these facets can be seen in Figure 44. This step accounts for any coupon-slippage during the test and ensures the model boundary conditions are as close to exact measured displacements as possible.

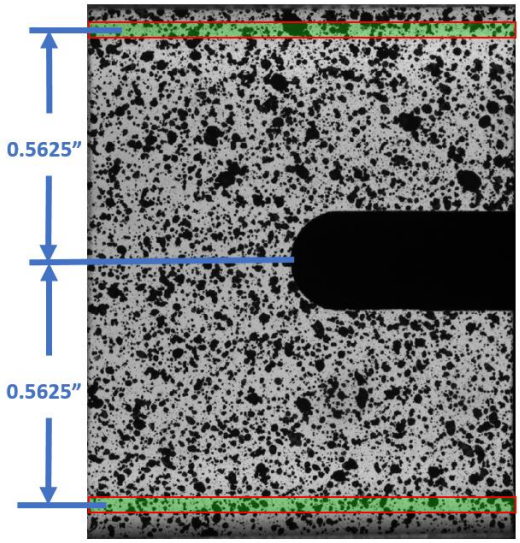

Figure 44. Example of the facets chosen for step 2 to determine boundary conditions for the ANSYS model

b. After the facets have been isolated in the undeformed configuration, a line is fit to them and their undeformed location is noted.

c. These facets' locations are then found (via the .txt file) and a line is fit to them with their deformed location noted.

d. MATLAB then calculates displacements necessary to reproduce the test in ANSYS (dx, dy and $d\theta$).

3. After the boundary conditions are determined, a properly formatted Python script is created via MATLAB to automatically run ANSYS Workbench to reproduce tests based on the boundary conditions determined in step 2d.

4. Desired strain values are stored in .txt file from ANSYS for all simulated tests.

The strain values obtained from the simulation (step 4) are treated identically to the values from the experimental portion of this study. Even though these values obtained

from the simulation are not measured values from a test, they do provide more insight about what happens to the sample close to the notch tip. Again, this is due the fact that DIC lacks the ability to accurately measure boundary displacements of facets created on the edge of the sample. There are large discrepancies between the model and the experimental data that will be discussed further in the next section.

Results and Discussion

The finite element model does not provide as much "weight" in supporting progressive damage models as experimental results. The results shown below are not to be treated on the same level as the experimental data previously displayed since the analytical model has been built based on the assumptions discussed above. Nonetheless, the finite element model for this study has possibly produced relevant data to supplement the experimental data. These results can be seen in several of the figures displayed below.

Just like an actual test performed with DIC, full-field strain calculations can be demonstrated as a "temperature plot" on the surface of the elements. This is useful as a model can be compared side-by-side to the actual data. The ability, from a qualitative standpoint, of the model to reproduce tests accurately is shown in Figure 45 below.

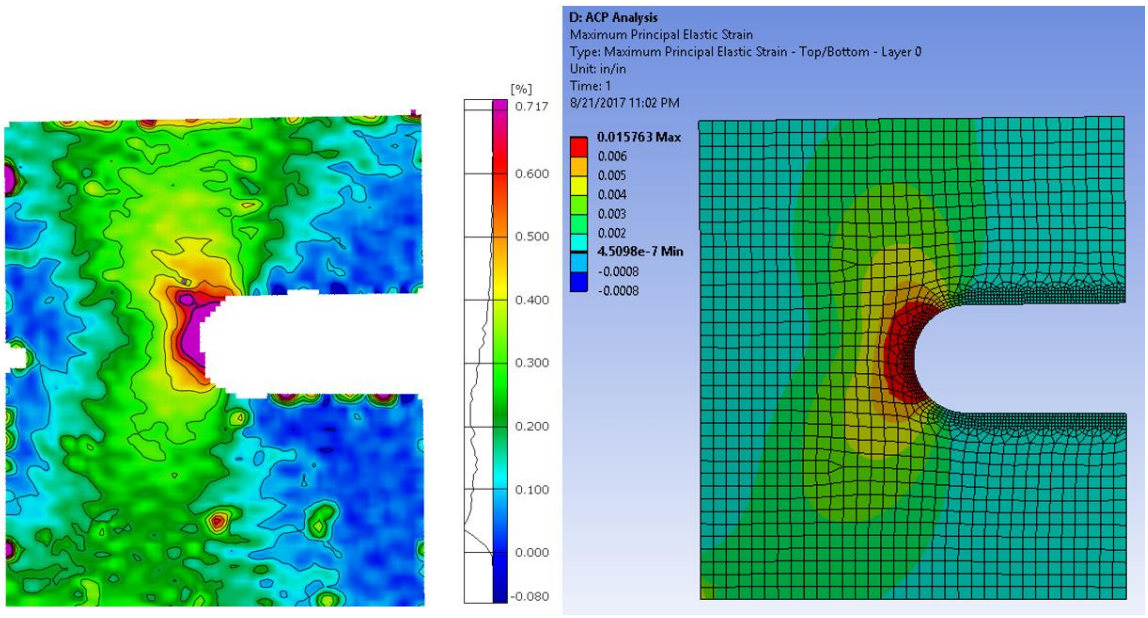

Figure 45. An arbitrarily chosen sample (11_021) results compared between experimental results and the finite element model. Maximum principal strain displayed

The figure displays the maximum principal strain of a sample. Boundary conditions were double checked; displacements were identical. As explained by the processing scheme, the model was controlled based on measured displacements from the experimental test. Boundary load responses were also checked between both results with an error of 12% for the load in the x-direction where the load was small and an error of 8.7% for the load in the y-direction which dominates the loading of this sample. The results are displayed with similar color scales for direct comparison and show reasonably similar strain distributions. The highest strained areas are identical with matching values. However, there does seem to be a discrepancy as the experimental data may include higher strains due to what appears to be transverse cracking underneath the surface of the sample. This cracking was determined, via dissipated energy (as discussed above), to not affect the mechanical response of the sample at the stage the image was taken.

Also, for comparison of experimental data to the finite element model, Figure 46 below shows the same sample (at the same stage) but with shear elastic strain displayed. This is to compare another strain measurement for the same sample. Again, the shear prediction from the model qualitatively matches the measured data of the test. The strain distributions, again, match and show the high-strain regions in the same locations as well as very similar values. These qualitative results are useful for the interpretation of experimental data as digital image correlation only provides information about the measured surface and nothing underneath.

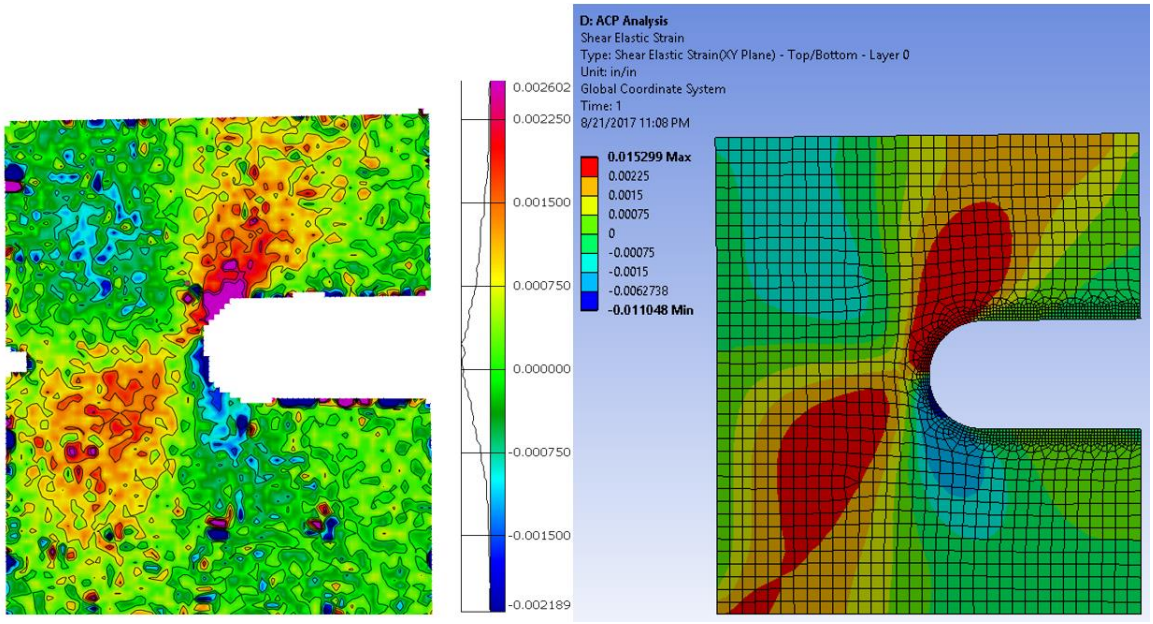

Figure 46. The same sample shown in Figure 45 (11_021) results compared between experimental results and the finite element model. Shear elastic strain displayed

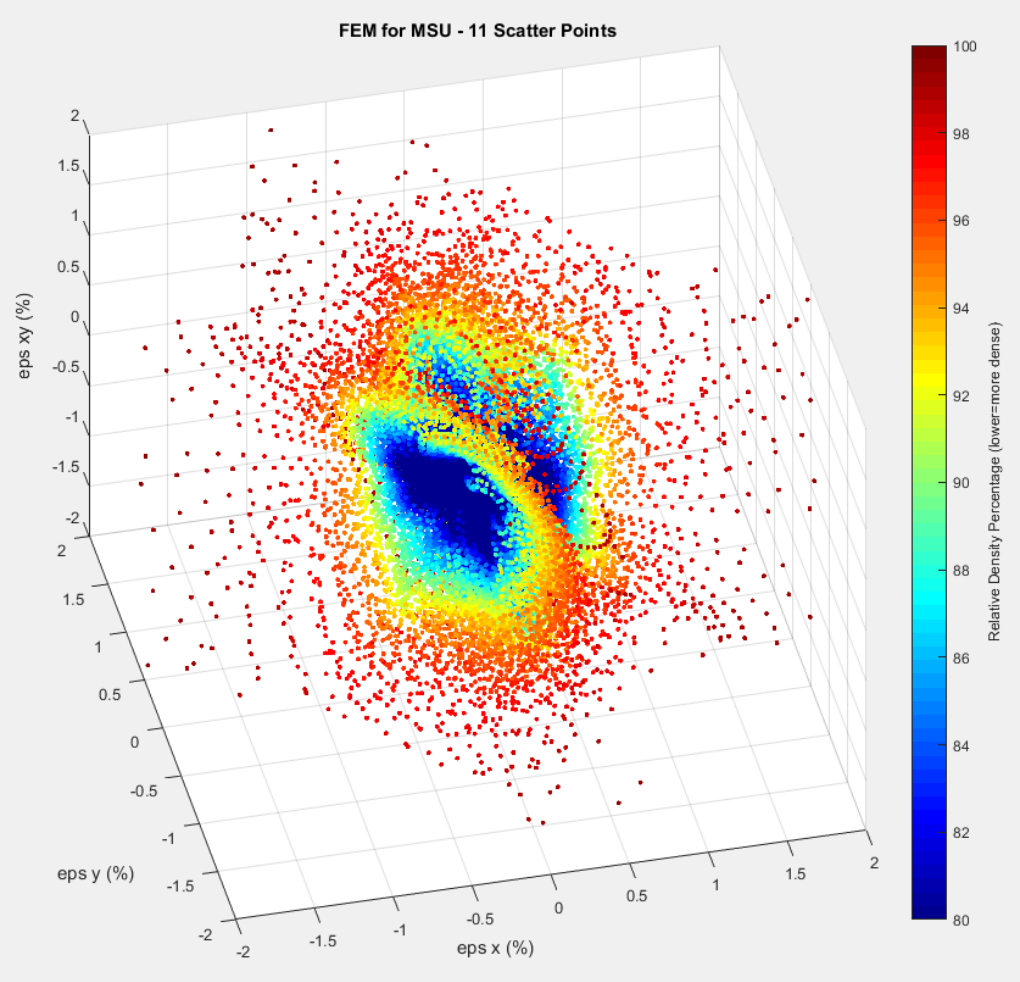

Figure 47. Point cloud developed from modeling all MSU - 11 tests and extracting strain data. Displayed as before

Furthermore, point clouds may be created the same way as the experimental data provided. The color formatting of the points also remains the same and is based on the probability distribution of calculated point densities. An example of a point cloud is shown in Figure 47 which represents the MSU-11 tests reproduced in the finite element model. Even though the model reproduces tests well, as shown in Figure 45 and Figure 46 above, there are obvious discrepancies between the experimental point cloud and the finite element model point cloud.

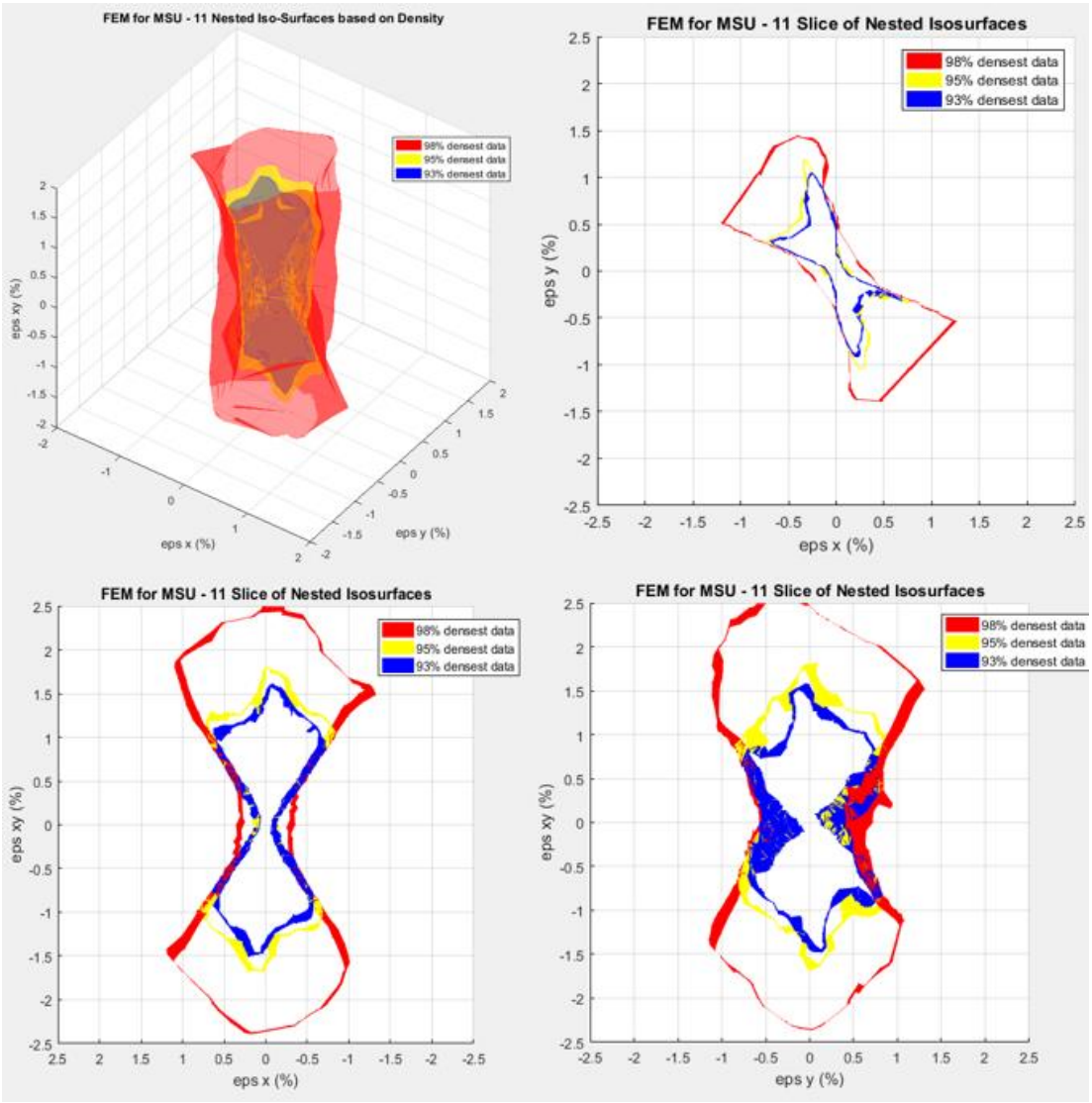

Figure 48. Nested isosurfaces for FEM - 11 displayed on each primary plane. Original nested isosurfaces (top-left). Primary plane $\varepsilon_{xy} = 0$ (top-right). Primary plane $\varepsilon_{y} = 0$ (bottom-left). Primary plane $\varepsilon_{x} = 0$ (bottom-right)

Obviously, due to assumptions of the model (listed above in the "Model Definition" section) and error in experimental data (primarily digital image correlation measurement errors as discussed previously), the point cloud created by a model will not match the point cloud generated by experimental data shown in Figure 30 and Figure 32 previously. An

explanation as to why the point clouds appear so different is that the model is truly an idealized ("perfect") version of the test. Figure 48, above, shows the nested isosurfaces and their respective "slices" as similarly demonstrated with the experimental data. It is easily seen from this image that the point cloud truly is concave primarily where ($\varepsilon_x < 0$ & $\varepsilon_y < 0$) as well as the region where ($\varepsilon_x > 0$ & $\varepsilon_y > 0$). This makes logical and physical sense as the model does not allow for tension-tension and compression-compression of an element due to the idealized Poisson effect[§§].

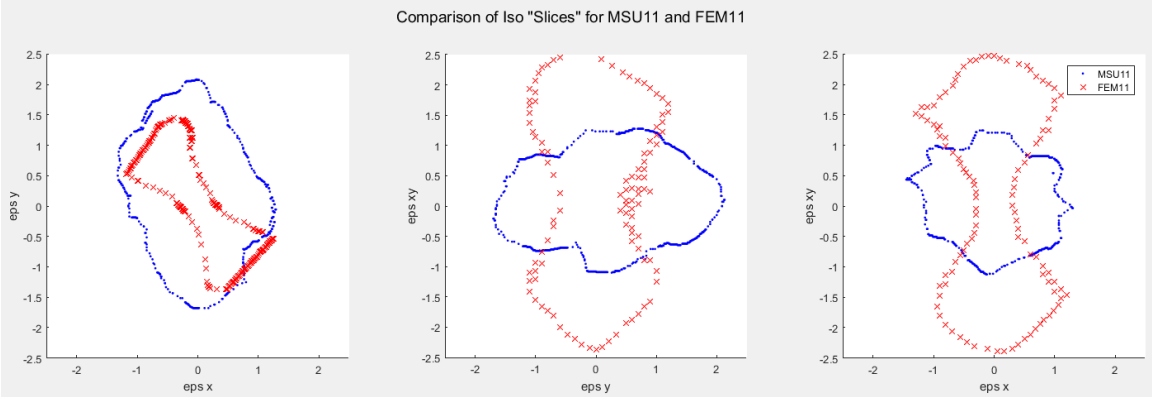

Figure 49. Direct comparison of "sliced" isosurfaces of MSU - 11 tests (Figure 33Figure 35) in blue and the FEM of MSU - 11 (Figure 48) in red

The experimental point cloud data, on the other hand, obviously does not have the "empty" regions where ($\varepsilon_x < 0$ & $\varepsilon_y < 0$) and ($\varepsilon_x > 0$ & $\varepsilon_y > 0$). This means that calculated facets in experimental tests did, in fact, experience strains of dilatational expansion and contraction. This discrepancy may be explained by ply interactions that are simply not accounted for in the model. In the model assumptions section above, constant

[§§] Poisson Effect – The phenomenon where a material experiences contraction in directions transverse to the direction of applied tension and vice versa.

strain though the material's thickness is explained; this assumption ties together elements in the z-direction. This simplifies the model for computation time and development by reducing the degrees of freedom within the model but with the now-obvious cost of accuracy. Ply interactions in the experimental tests could include physical damage occurring in mid-layer plies and inter-ply shear effects.

As mentioned above, this model was primarily used for supplementing and interpreting experimental data. The primary process used was identifying damage modes predicted by analytical failure criteria discussed above in the Multiaxial Testing section. This provided analytical insight about the failure mode expected during the test and was used to aid in the population of the progressive damage models displayed in APPENDIX C.

CONCLUSIONS

First, to recap, the purpose of this research is to inform and validate progressive damage models for their use with composite materials. Progressive damage models are becoming more prevalent for use in designs and can provide crucial information about the function and performance of a developing design. The ability to predict damage in any material, especially composites has proven to be difficult and nearly impossible to do accurately. There exist many analytical failure prediction models that have their own strengths and weaknesses. To better understand the drawbacks of these analytical methods, a large amount of test data is required. Furthermore, to inform and validate any model, particularly progressive failure models, this requirement stands and experimentally obtained data is crucial for their development and use.

Many of the analytical failure criteria combine mixed modes of loading in attempt to predict damage. However, the validation of these mixed mode combinations remains largely uncharacterized due to the inability for mixed mode testing. Typical mechanical testing of materials includes tension, compression, shear, and many others but rarely incorporates combinations such as biaxial tests. The Montana State University's In-Plane Loader poses a solution to this problem as it can apply combinations of displacements that are atypical to standard mechanical tests. This study aimed to test composite materials in many displacement combinations as an attempt to see how well multiaxial testing can produce mixed-mode responses in the material.

In combination with mixed-mode testing, the use of digital image correlation for full-field strain measurements was explored. The benefits of digital image correlation

rather than traditional strain measurement techniques, is that high resolution and low error strain measurements can be collected for the full length of the test. Digital image correlation is also helpful for the direct comparison, as mentioned several times, between an experimental test and an analytical finite element model.

Experimental Conclusions

A lot of information can be gathered from the experimental data in this study. Even though many of the results simply cannot be displayed in this document format, many of them can provide the information desired to both qualitatively and quantitatively inform and validate progressive damage models.

As described in the "Loading Paths" section, many different combinations of displacements are applied to each set of coupons. This was done in attempt to fully characterize the materials for many different loading cases. However, due to many factors, a total of only one hundred and eleven (111) samples were used for this study to characterize 6 independent laminates. This number of samples took a lot of time to test and process, and for this reason, no more were attempted. Even with this number of samples, the number of load paths was limited; for full characterization of a material, many more tests should be performed. Furthermore, many tests of the same load path should be run from a reliability standpoint and to increase the statistical significance of the data. For further recommendations regarding experimental tests, refer to the recommendations portion of this document.

Perhaps the two most useful results from this study are the qualitative video reports created in ARAMIS and the failure surfaces for each laminate. First, the ARAMIS reports

offer the ability to compare, side by side, an experimental test and a finite element model simulation of that test. This would primarily be used for the validation of a progressive damage models and allow the user to determine if the model is accurately predicting damage. Second, the failure surfaces produced may directly inform progressive damage models as they provide experimental insight about when damage is predicted to occur rather than various, and possibly inaccurate, analytical failure criteria.

The idea of producing experimental failure surfaces is simple. The strains measured on a sample prior to damage are "acceptable" strains and do not cause failure. However, when these strains exceed a limit, damage occurs. With digital image correlation, the strains are collected in situ and the strains that cause failure can be isolated. These strains are then displayed graphically in point clouds and a data density program determines how reliable each individual point is. Regions that have many points are determined to be "safe strains" where the material has repeatedly experienced these strains without damage occurring. At some point, away from the cluster, the material is more likely to experience damage; this is determined by the "empty" regions in the point cloud as the material has never experienced strains of that magnitude without damaging.

The failure surfaces produced in this study "nest" several different calculated surfaces which resemble levels of conservativeness. If the largest failure surface (red) is chosen, it is obviously less conservative than the smallest failure surface (blue). A design is less likely to incur damage when experiencing strains bounded by smaller surface than the larger. Ultimately, these failure surfaces may be used to control damage models and provide validation of existing and developing designs.

Since damage models typically require damage initiation criteria to function accurately, these experimentally determined failure surfaces could be used to inform the model as to when damage initiates. This likely would need to be done using a mathematical representation of the failure surface rather than the amorphous experimental envelope. This will be discussed further in the recommendations section to follow.

Furthermore, the failure surfaces produced may be useful for the validation/ qualification of existing designs. This may be done analytically or experimentally. Analytically, the failure surface may be used to inform a model or be otherwise applied in order to theoretical/ analytically determine strains of a design. Experimentally, measured strains from a design incorporating the appropriate material may be compared to surface. Strain data, whether measured or otherwise determined, that surpasses the boundaries of the surface is predicted to have caused damage in the material. Using this information, proper decisions can be made whether this means decommissioning an existing part, increasing inspection intervals, repairing components, or redesigning the part.

Finally, the produced failure surfaces may be useful for the comparison of different material systems. As displayed in Figure 36 above, different materials' strain limits (and stress limits) can be directly compared with each other. This may result in a useful tool for the selection of materials in designs. If a material is selected, used in design, and analytically/ experimentally determined to incur damage during service, a replacement for the original material with better damage properties may be selected.

Finite Element Model Conclusions

Overall, the results produced from the model were determined to not suffice as a method of informing and validating progressive damage models. Even though the model was determined to not suffice in the primary purpose of this study, it did aid in the interpretation of experimental results. There are several factors that contribute to this.

- Direct modeling of experimental tests.
    - The method described above allows for the reproduction of experimental data within a FEM with little error.
    - Models are controlled by "exact" measurements determined by DIC.
- Digital image correlation has limits.
    - Calculations of material responses under the outermost surface of the coupon cannot be made with DIC. An FEM allows for inspection, on a theoretical level, of material responses within each ply.
    - Calculations cannot be defined on edges of a sample via DIC. FEMs can produce results on these boundaries to supplement the experimental data.
    - Although not used in this study, some FEMs (particularly damage models) may provide insight about damage progressing through the material. DIC typically produces large errors when examining a damaged sample.
- Applying analytical failure criteria.
    - With the idealized reproduction of an experimental test, this data can be analyzed further by applying analytical failure criteria. The model allows for rapid adjustments within the model that apply many different failure

criteria with ease. This analysis would be lengthy and cumbersome without features from the model.

- Analytical failure criteria, although perhaps inaccurate as described previously, provide additional perspective on damage modes within a sample.

It is going to be emphasized one last time that the model presented in this study is not a progressive damage model. Even though this model incorporates a tool for applying established failure criteria, the model does not attempt to reconcile damage prediction by modeling the damage itself. The results of the model, discussed above, allow for several conclusions to be made regarding this type of work and finite element models.

- Finite element models are useful for experimental data interpretation.
  - Finite element models, no matter how idealized, may provide useful analytical insight as to what occurs during an experimental test. Useful interpretation tools could be:
    - The application of analytical failure criteria to understand damage.
    - To simulate the response of materials where data can simply not be collected during an experimental test e.g. edges of a sample via digital image correlation.
    - To determine how experimental results may stray from an idealized analytical version.
- Finite element models are exactly that… models.

- Models require, on some level, assumptions to be made. As an example, constitutive and damage responses characterizations never reduce into the scalars that are used in models; variability always exists.
- The assumptions made in any model, no matter how complex, do not and cannot fully describe what occurs in reality. These tools can certainly be refined and honed to become more accurate but they should be treated as the models that they are. Structures that utilize models in their design process must be validated and substantiated by experimental results.

FUTURE WORK

High Strain-Rate Multiaxial Testing

Very briefly, a new exploratory research project using the IPL to test materials under high strain rates is being performed by Chris Stroili. This research is similar to the study described in this document except that it focuses the use of multiaxial testing and digital image correlation for the testing of isotropic materials. As the concept of multiaxial testing is understood but rarely performed, this research focuses on discovering the merits of high strain-rate multiaxial testing and its capabilities to produce data useful for modeling and analysis.

Multiaxial Testing Recommendations

This portion will discuss the recommendations pertaining specifically to multiaxial testing. A review of previous theses' recommendations for the IPL clearly demonstrates that the IPL is a "work in progress" and will likely remain as such. However, as problems continue to be resolved, the requirements, justification, and utility for multiaxial testing becomes more apparent.

Data Processing

There are many options that were not explored in this study to increase the usefulness of this data. The topics below discuss a couple of the primary ideas for further processing of the data.

- Comparison of experimental data to existing failure criteria

- The comparison of existing failure criteria and the experimentally determined failure surfaces would not be to validate the experimental data. This would only provide insight about how data should be interpreted and used.

- Mathematical "fit" to experimental data
  - An ellipsoidal (3-dimensional quadratic) fit program was written for this study but ultimately not executed. The approximate run time for the script was estimated in MATLAB to be over 50 hours.
    - This MATLAB script employs a power least squares fit that weights "outliers" less than highly dense data.
  - Any mathematical (not necessarily quadratic) expression, may be useful for the application of this data into a finite element software. Finite element software can easily operate under mathematical parameters and the use of the amorphous experimental envelope may prove impossible in a finite element code.

Furthermore, in addition to ideas that may produce useful data, this short portion will discuss recommendations about processing data in general. First, the data processed in this study is dense and, to process, it requires a lot of computer resources. For this reason, once data is processed, *all* variables should be saved so that their retrieval is easy. If adjustments need to be made, existing variables can be used which will reduce processing time. Second, as much processing as possible should be performed within ARAMIS software before exporting. ARAMIS, especially newer versions, allow for calculations to

be made within the software. Any calculations that can be handled by ARAMIS should be used and may even prove useful for creating additional qualitative reports like Figure 26 shown previously.

IPL Compliance

As discussed much in Smith's thesis [13], the IPL compliance remains an issue even up to the fifth generation of the IPL. Future work should determine a way to account for the compliance in the IPL and/or increase its rigidity. In a perfect testing situation, the machine used to provide loads to the coupon should be infinitely rigid or at least far more rigid than the sample being tested. The IPL was designed sufficiently to handle loads from the actuators through bearings, load cells, frame, fastener joints, and grips without expecting permanent deformation of any sort to the IPL. However, even though the IPL is designed sufficiently for strength, the components of the IPL act as springs and store elastic energy that can then be transmitted to the coupon – particularly during damage. This poses problems primarily from a control standpoint.

The IPL is a position controlled machine, as mentioned in its introduction. Since the IPL acts as a spring and stores energy, this poses two primary problems for control of the machine. First, an input for displacements is entered and the software tracks the encoders on the actuators to ensure the prescribed displacement is achieved at the proper rate, but the coupon doesn't experience the prescribed displacement due to the deflection of the IPL itself. This makes it difficult to achieve specific displacement states to the coupon. Second, as the coupon experiences damage up to a *critical value*, the stored energy in the IPL abruptly damages the coupon further. This is the primary issue caused by IPL

compliance as data over the abrupt damage period is nearly impossible to measure accurately with the current equipment.

Automation of the IPL

Again, as mentioned in Smith's thesis [13], tests require a substantial amount of time investment. Previously, Smith mentions that tests take about a half hour to complete, this remains to be the case due to the manual nature of the machine and data collection necessary for each test. This does not include setup, intermittent calibrations, or teardown of equipment. As mentioned earlier, it is necessary to have as many tests as possible to produce statistically significant results. For this reason, it is recommended that future work with the IPL be automated as much as possible – any reduction to test time would be extremely beneficial. Furthermore, it is also recommended that future multiaxial testing machine designs consider automation, specifically coupon loading and testing, as a design priority.

IPL Software and Control

Although the software has been much improved due to the hard work of Dr. Michael Edens, improvements could still be made. First, load control is currently being pursued as an option of IPL control. Load control would consist of prescribing a load state and running a PID (proportional, integral, and differential) control loop determining, in real-time, necessary actuator displacements to achieve such a state. This would potentially mitigate the rapid damage noted in the previous section and provide more versatility in testing. Second, a more robust method of returning the IPL to a "home" position should be considered. A faster "reset" between samples would cut down on test and setup time.

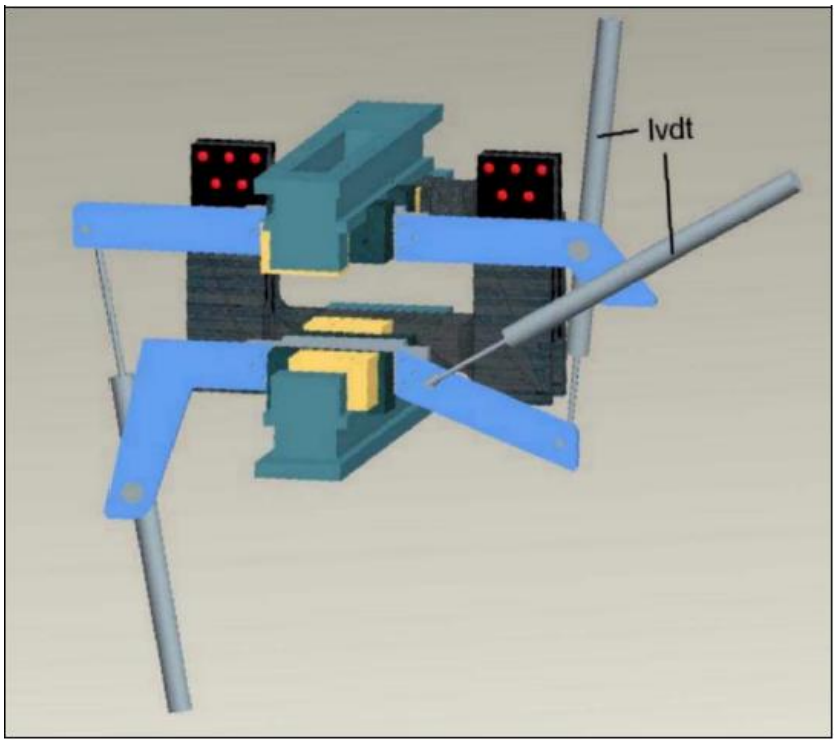

Figure 50. Third and Fourth generation IPL grip assembly as shown in Collett [11]. LVDTs are used for the displacement control software

If the previously mentioned compliance issues remain uncorrected, a way of potentially solving the resulting problems may be to instrument the IPL closer to the grips for position control or feedback. Figure 50 shows a configuration of grip position data acquisition that was used in the third and fourth generation IPL but was removed due to signal noise issues in the LVDTs. The LVDTs were then, as mentioned before, appointed for use as a means of quick calibration for the IPL position kinematics. Collett also identified the position data acquisition at the grips to be inaccurate and proposed a change in LVDT configuration like NRL's in-plane loader. A new design should be implemented for better control and validation of the IPL displacements whether a new, more accurate

LVDT setup such as that suggested by Collett or another form of accurate displacement measurement technology (maybe even real-time DIC-IPL control).

Long-Term Suggestions

Whether employing a new multiaxial testing system entirely or considering major retrofits to the existing IPL, here are several suggestions that are not discussed above. First, consider hydraulic, servo-motor, or another form of high-speed actuation. Another functionality of multiaxial testing could be fatigue testing or high strain rate testing for multiaxial states which would require much faster and responsive actuation than the existing stepper-motor actuators. An actuator retrofit to the existing IPL may be unfeasible but for later versions of multiaxial testing machines, this should be a consideration.

Second, consider adding a dedicated third-party camera fixed to the IPL and suitable for DIC measurements. This would reduce setup time and may mitigate measurement issues when using DIC. As mentioned above, Parker attempted such a feat using a MATLAB script [15], but it is easier to use the stereo camera setup for the existing ARAMIS setup. Note: A single third-party camera with use on the ARAMIS cannot capture three-dimensional deformations; and the use of a third-party camera will also require nontrivial innovation to interface the IPL, camera, and ARAMIS systems.

Third, consider laying the IPL on its side similar to the first-generation IPL. This would likely be better suited for an entirely new in-plane machine. Even with the new ‘out-of-plane constrainers’, maintaining proper cross-head alignment is difficult especially during any compression test. One of the ideas discussed was mounting the cross-head to a large air-bearing similar to what is used for three-axis machining with a large slewing

bearing to allow for rotation. This would give the proper degrees of freedom with only the tolerances of the bearings, compliances, and joints to account for out-of-plane displacements. The other (lower) part of the IPL would be fixed to the same planar surface as the air-bearing.

Fourth, consider using other technologies in tandem with multiaxial testing. Technologies that are readily available at MSU but have not been integrated into multiaxial testing include but aren't limited to: acoustic emission (AE), scanning electron microscopy (SEM), CT scans, and ultrasound. These measurement technologies all provide different means to quantify damage either during or post-test.

Digital Image Correlation (ARAMIS) Recommendations

The GOM ARAMIS digital image correlation system performs well when used properly. However, since the system is about 8 years old, the software and hardware have many expected performance issues. There are only several recommendations that should be considered for any lengthy study involving the use of any digital image correlation system.

Computer Resources

Computer resources including RAM, hard drive space, graphics cards, and CPU are limited on this older system. These are listed with primary concerns first. RAM occasionally poses a problem with processing large amounts of data and for the use of "Fast-Measurement Mode". Without an expansion of RAM, the system is limited on its

processing and measuring capabilities since much of the data is stored in RAM for processing.

Second, hard drive space is an issue that should be handled if any large data sets are desired. Stored tests require approximately 8 GB of storage space for 300 stages. For the purpose of this study, most tests performed were stored as 150 stages to reduce this storage cost but at a loss of data resolution. Finally, graphics cards, CPU, and perhaps software limitations prevent the processing of large data sets. Each test may take approximately 2 hrs. to process fully using this system. Much of this time spent is due to a computer-only processing time that may be reduced with more efficient hardware.

Software Limitations

For this study, GOM ARAMIS v6.3 was used for the collecting and processing of data. This version of the software limits users in some ways to automate tests and has many limitations on processing abilities. It is highly recommended that, for future use with this type of work, the latest software be used. The latest software boasts better automation capabilities, exporting, and direct comparison within the software to finite element model data. This can be used to correlate test data directly to a finite element model without the use of a third-party software.

Camera Hardware

For this section, there are only a few recommendations. First, it is highly recommended that calibration and setup remain the same as much as possible. Keeping the cameras in a single location without moving them helps to reduce calibration issues. Secondly, for the use of the existing cameras, additional well-filtered lighting should be

sought. The more light on the sample, the more closed the camera apertures can be which increases depth of field and decreases shutter time. This will result in sharper images especially for high frame-rates and high strain-rates.

Finally, new camera hardware should eventually be sought. This system has very high-quality resolution; however, the latest models have more sensitive sensors that perform better in low-light situations as well as record higher-resolution images. The higher the image resolution, the better the strain field computation. The more sensitive the sensor, the less light required and can therefore have increased shutter speed – ultimately, this may allow for high strain-rate testing with the use of 3D digital image correlation.

REFERENCES CITED

[1] T. Palucka and B. Bensaude-Vincent, "Composites Overview," California Technical Institute, 19 October 2002. [Online]. Available: http://authors.library.caltech.edu/5456/1/hrst.mit.edu/hrs/materials/public/composites/Composites_Overview.htm. [Accessed 06 January 2017].

[2] National Materials Advisory Board, "Accelerating Utilization of New Materials," NMAB, Washington D.C., 1971.

[3] E. J. Barbero, Introduction to Composite Materials, 2nd ed., Boca Raton, FL: Taylor and Francis Group, 2011.

[4] U.S. Department of Defense, MIL-HDBK-17-1F: Composite Materials Handbook, Polymer Matrix Composites: Materials Usage, Design, and Analysis, vol. 17, Department of Defense, 2002.

[5] Federal Aviation Administration, "de Havilland DH-106 Comet 1," U.S. Department of Transportation, Washington, DC, 2016.

[6] T. L. Anderson, Fracture Mechanics - Fundamaentals and Applications 2nd Edition, Boca Raton, Florida: CRC Press LLC, 1995.

[7] M. Hinton, A. S. Kaddour and P. D. Soden, Failure Criteria in Fibre Reinforced Polymer Composites: The World-Wide Failure Exercise, Oxfod, UK: Elsevier, 2004.

[8] R. M. Christensen, "Failure Criteria," Stanford University, 9 June 2017. [Online]. Available: http://www.failurecriteria.com/theworldwidefail.html.

[9] P. W. Mast, G. E. Nash, J. G. Michopoulos, R. Thomas, R. Badaliance and I. Wolock, "Characterization of strain-induced damaged in composites based on the dissipated energy density," *Theoretical and Applied Fracture Mechanics,* Vols. I, II, III, no. 22, pp. 71 - 125, 1995.

[10] E. Booth, K. Higgins and M. Schaff, "In-plane loader, a multi-axis composite testing machine 'Senior Design Project'," Montana State University, Bozeman, 2001.

[11] A. B. Collett, ""A Validation Study of the Montana State University In-Plane Loader" MSME thesis," Montana State University, Bozeman, 2006.

[12] W. Ritter, ""Application of Energy Methods to Modeling Failures in Composite Materials and Structures" MSME thesis," Montana State University, Bozeman, 2004.

[13] J. D. Smith, ""Internal Damage Characterization for Composite Materials Under Biaxial Loading Configuration" MSME Thesis," Montana State University, Bozeman, 2007.

[14] J. T. Schmitt, ""Damage Initiation and Post-Damge Response of Composite Laminates by Multi-Axial Testing and Nonlinear Optimization" MSME thesis," Montana State University, Bozeman, 2008.

[15] J. W. Parker, ""Development and Implementation of a Low cost Image Correlation System to Obtain Full-Field In-Plane Displacement and Strain Data" MSME thesis," Montana State University, Bozeman, 2009.

[16] F. Hild, A. Bouterf and S. Roux, "Damage Measurements via DIC From Physical to Mechanical Damage," *International Journal of Fracture,* pp. 1-38, 2015.

[17] GOM mbH, *ARAMIS v6.1 and higher User Manual,* Braunschweig, Germany, 2007.

[18] Wichita State University, "Hexcel 8552 IM7 Unidirectional Prepreg 190 gsm & 35%RC Qualification Material Property Data Report," National Intitute for Aviation Research, Wichita, KS, 2011.

[19] "McMASTER-CARR," McMASTER-CARR, [Online]. Available: https://www.mcmaster.com/#.

[20] N. E. Dowling, Mechanical Behavior of Materials 'Engineering Methods for Deformation, Fracture, and Fatigue', Fourth Edition ed., Upper Saddle River, New Jersey: Pearson, 2013.

[21] GOM Aramis, *a non-contact and material-independent measuring software/hardware system based on digital image correlation. 49 531 390290,* www.gom.com.

[22] MATLAB, *a mathematics and programming software available from Mathworks. 508 647 7000,* www.mathworks.com.

[23] Instron, *materials testing hardware and software available from INSTRON. 800 564 8378,* www.instron.us/en-us/.

[24] NI LabVIEW, *a commercial control software package available from National Instruments. 877 388 1952,* www.ni.com.

[25] ANSYS, *a commercial finite element software package available from ANSYS Inc. 844 462 6797,* www.ansys.com.

APPENDICES

APPENDIX A:

TEST MATRICES

Table 6. Test Matrix for MSU-11. [-45/90/45/0]s laminate with IM7/8552 material system. Comp. abbreviation for compression

Test Name	Test Speed (in/min)	Control Displacements			Damage Initiation Stage	Comments
		dx (in)	dy (in)	dθ (deg)		
11_003	0.1	-0.50	0.09	33.93	101	Preliminary test
11_004	0.1	-0.50	-0.03	44.30	72	Preliminary test
11_005	0.1	-0.50	0.09	33.93	90	Preliminary test
11_006	0.1	0.50	-0.19	-25.09	42	Preliminary test
11_007	0.1	-0.50	0.03	38.90	58	Preliminary test
11_008	0.1	-0.50	-0.03	44.30	62	Preliminary test
11_009	0.1	0.50	-0.19	-25.09	58	Preliminary test
11_010	0.05	-0.50	0.00	0.00	80	
11_011	0.05	0.50	0.00	0.00	72	
11_012	0.05	0.00	0.50	0.00	35	
11_013	0.05	0.00	-0.50	0.00		Comp.- Not Used
11_014	0.2	0.00	0.00	-10.00	134	
11_015	0.5	0.00	0.00	10.00	60	
11_016	0.05	-0.50	0.50	0.00	44	
11_017	0.05	0.50	0.50	0.00	62	
11_018	0.2	-0.50	0.00	-10.00	104	
11_019	0.2	0.50	0.00	-5.00	98	
11_020	0.2	0.00	0.50	-10.00	69	
11_021	0.2	0.00	0.50	10.00	68	
11_022	0.4	-0.50	0.50	-10.00	56	
11_023	0.4	0.50	0.50	-10.00	41	
11_024	0.4	-0.50	0.50	10.00	32	
11_025	0.4	0.50	0.50	10.00	63	

Table 7. Test Matrix for MSU-13. [0/90/0/90]s laminate with IM7/8552 material system. Comp. abbreviation for compression. NFF abbreviation for No Final Failure. GS abbreviation for Grip Slippage

Test Name	Test Speed (in/min)	Control Displacements			Damage Initiation Stage	Comments
		dx (in)	dy (in)	dθ (deg)		
13_008	0.05	0.50	0.00	0.00	105	Preliminary test
13_009	0.05	0.50	0.02	0.00	86	Preliminary test
13_010	0.1	-0.50	0.00	0.00	30	
13_011	0.1	0.50	0.00	0.00	84	
13_012	0.1	0.00	0.50	0.00	18	NFF - GS
13_013	0.1	0.00	-0.50	0.00		Comp.- Not Used
13_014	0.4	0.00	0.00	-10.00	54	
13_015	0.8	0.00	0.00	10.00	41	
13_016	0.1	-0.50	0.50	0.00	14	
13_017	0.1	0.50	0.50	0.00	44	
13_018	0.8	-0.50	0.00	-5.00	35	
13_019	0.4	0.50	0.00	-5.00	45	
13_020	0.5	0.00	0.50	-10.00	137	NFF - GS
13_021	0.8	0.00	0.50	10.00	23	
13_022	0.6	-0.50	0.50	-10.00	22	
13_023	0.6	0.50	0.50	-10.00	29	
13_024	0.6	-0.50	0.50	10.00	20	
13_025	0.6	0.50	0.50	10.00	43	

Table 8. Test Matrix for MSU-14. [-45/45/-45/45]s laminate with IM7/8552 material system. Comp. abbreviation for compression. NFF abbreviation for No Final Failure. GS abbreviation for Grip Slippage. IPL Lim. Abbreviation for IPL Limit Reached

Test Name	Test Speed (in/min)	Control Displacements			Damage Initiation Stage	Comments
		dx (in)	dy (in)	dθ (deg)		
14_010	0.1	-0.50	0.00	0.00	24	
14_011	0.05	0.50	0.00	0.00	67	
14_012	0.1	0.00	0.50	0.00	19	
14_013	0.1	0.00	-0.50	0.00		Comp.- Not Used
14_014	0.5	0.00	0.00	-10.00	28	NFF - IPL Lim.
14_015	1	0.00	0.00	10.00	60	Buckle Failure
14_016	0.5	-0.50	0.50	0.00	12	
14_017	0.1	0.50	0.50	0.00	44	
14_018	0.1	-0.50	0.00	-10.00	42	NFF - IPL Lim.
14_019	0.5	0.50	0.00	-5.00	46	NFF - GS
14_020	0.5	0.00	0.50	-10.00	28	
14_021	0.5	0.00	0.50	10.00	41	
14_022	0.4	-0.50	0.50	-10.00	51	
14_023	0.4	0.50	0.50	-10.00	58	
14_024	0.4	-0.50	0.50	10.00	30	
14_025	0.6	0.50	0.50	10.00	27	

Table 9. Test Matrix for MSU-1. [-45/90/45/0]s laminate with Toray material system. Comp. abbreviation for compression. NFF abbreviation for No Final Failure. GS abbreviation for Grip Slippage

Test Name	Test Speed (in/min)	Control Displacements			Damage Initiation Stage	Comments
		dx (in)	dy (in)	dθ (deg)		
1_005	0.05	0.00	0.50	0.00	53	Preliminary test
1_006	0.03	0.00	0.50	0.00	46	Preliminary test
1_009	1	0.13	0.13	5.00	31	Preliminary test
1_010	0.05	-0.50	0.00	0.00	43	
1_011	0.05	0.50	0.00	0.00	121	NFF - GS
1_012	0.05	0.00	0.50	0.00	41	Noisy Data
1_013	0.05	0.00	-0.50	0.00		Comp.- Not Used
1_014	0.2	0.00	0.00	-10.00	175	
1_015	0.5	0.00	0.00	10.00	26	
1_016	0.05	-0.50	0.50	0.00	36	
1_017	0.1	0.50	0.50	0.00	56	
1_018	0.2	-0.50	0.00	-5.00	89	
1_019	0.2	0.50	0.00	-5.00	31	
1_020	0.5	0.00	0.50	-10.00	226	NFF - GS
1_021	0.5	0.00	0.50	10.00	34	
1_022	0.4	-0.50	0.50	-10.00	54	
1_023	0.4	0.50	0.50	-10.00	63	
1_024	0.4	-0.50	0.50	10.00	23	
1_025	0.4	0.50	0.50	10.00	46	
1_026	0.1	0.50	0.50	0.00	58	

Table 10. Test Matrix for MSU-3. [0/90/0/90]s laminate with Toray material system. Comp. abbreviation for compression. NFF abbreviation for No Final Failure. GS abbreviation for Grip Slippage. IPL Lim. Abbreviation for IPL Limit Reached

Test Name	Test Speed (in/min)	Control Displacements			Damage Initiation Stage	Comments
		dx (in)	dy (in)	dθ (deg)		
3_007	0.08	0.00	0.50	0.00	32	Preliminary test
3_008	0.04	0.00	0.50	0.00	34	Preliminary test
3_009	1	-0.25	0.25	10.00	26	Preliminary test
3_010	0.1	-0.50	0.00	0.00	43	
3_011	0.1	0.50	0.00	0.00	61	
3_012	0.1	0.00	0.50	0.00	28	NFF - GS
3_013	0.1	0.00	-0.50	0.00		Comp.- Not Used
3_014	0.8	0.00	0.00	-10.00	65	
3_015	0.8	0.00	0.00	10.00	97	
3_016	0.1	-0.50	0.50	0.00	20	
3_017	0.1	0.50	0.50	0.00	16	NFF - GS
3_018	0.8	-0.50	0.00	-5.00	7	Fast Test
3_019	0.4	0.50	0.00	-5.00	65	
3_020	0.8	0.00	0.50	-10.00	44	NFF - IPL Lim.
3_021	0.8	0.00	0.50	10.00	24	
3_022	0.6	-0.50	0.50	-10.00	46	NFF - IPL Lim.
3_023	0.6	0.50	0.50	-10.00	33	NFF - IPL Lim.
3_024	0.6	-0.50	0.50	10.00	24	
3_025	0.6	0.50	0.50	10.00	45	

Table 11. Test Matrix for MSU-3. [-45/45/-45/45]s laminate with Toray material system. Comp. abbreviation for compression. NFF abbreviation for No Final Failure. GS abbreviation for Grip Slippage. IPL Lim. Abbreviation for IPL Limit Reached

Test Name	Test Speed (in/min)	Control Displacements			Damage Initiation Stage	Comments
		dx (in)	dy (in)	dθ (deg)		
4_005	0.06	0.00	0.50	0.00	48	Preliminary test
4_006	0.06	0.00	0.50	0.00	16	Preliminary test
4_007	0.06	0.00	0.50	0.00	43	Preliminary test
4_008	0.06	0.00	0.50	0.00	58	Preliminary test
4_009	1	-0.25	0.25	10.00	64	Preliminary test
4_010	0.05	-0.50	0.00	0.00	36	
4_011	0.05	0.50	0.00	0.00	56	
4_012	0.2	0.00	0.50	0.00	9	
4_013	0.2	0.00	-0.50	0.00		Comp.- Not Used
4_014	1	0.00	0.00	-10.00	3	NFF - IPL Lim.
4_015	1	0.00	0.00	10.00	87	NFF - IPL Lim.
4_016	0.2	-0.50	0.50	0.00	14	
4_017	0.1	0.50	0.50	0.00	39	
4_018	0.5	-0.50	0.00	-5.00	33	
4_019	0.5	0.50	0.00	-5.00	71	NFF - GS
4_020	0.5	0.00	0.50	-10.00	42	
4_021	0.5	0.00	0.50	10.00	47	
4_022	0.4	-0.50	0.50	-10.00	31	NFF - IPL Lim.
4_023	0.5	0.50	0.50	-10.00	30	
4_024	0.5	-0.50	0.50	10.00	40	
4_025	0.5	0.50	0.50	10.00	35	

APPENDIX B:

LAMINATE-LEVEL FAILURE

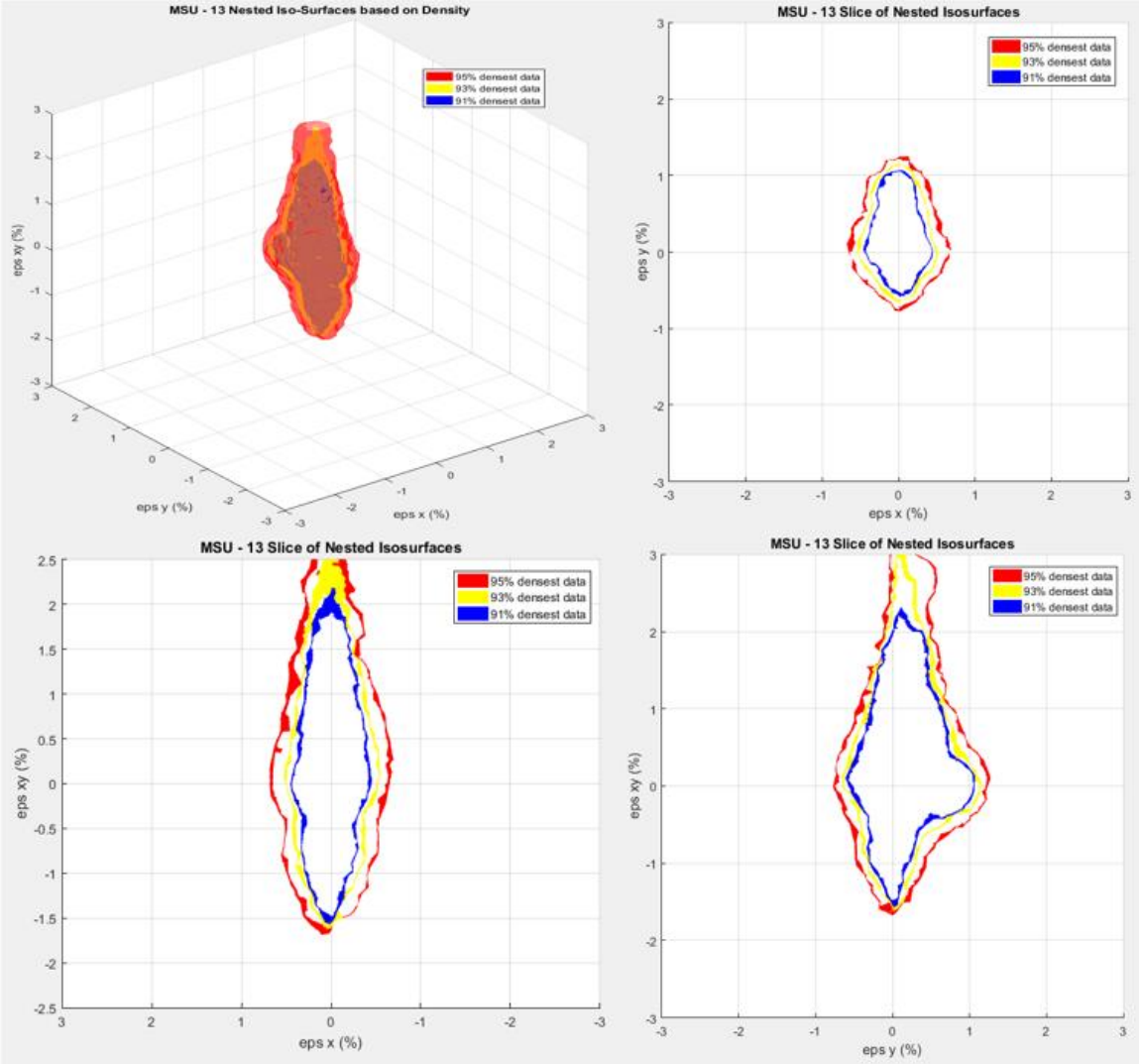

Figure 51. Nested isosurfaces for MSU - 13 displayed on each primary plane. Original nested isosurfaces (top-left). Primary plane eps xy = 0 (top-right). Primary plane eps y = 0 (bottom-left). Primary plane eps x = 0 (bottom-right)

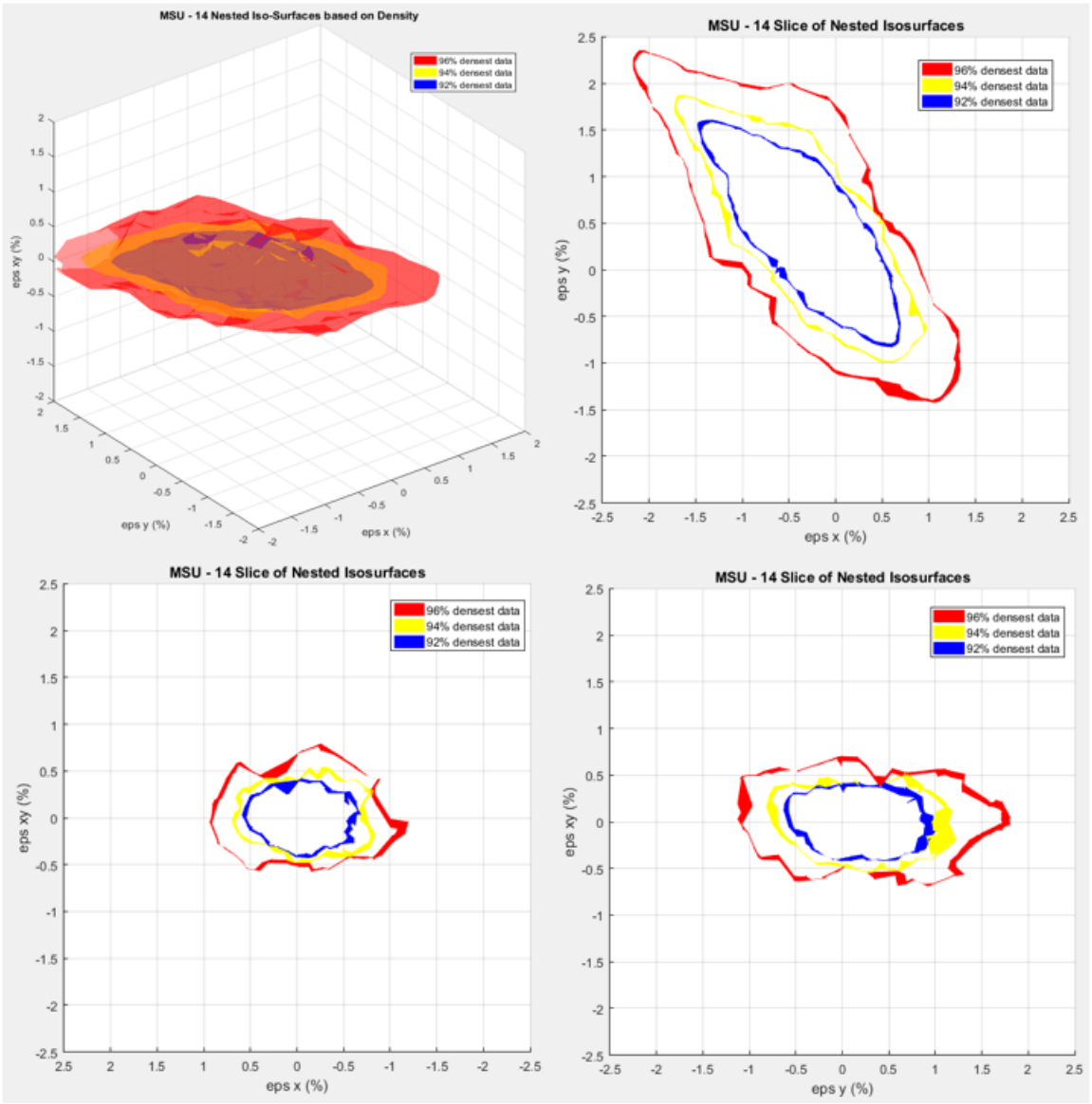

Figure 52. Nested isosurfaces for MSU - 14 displayed on each primary plane. Original nested isosurfaces (top-left). Primary plane eps xy = 0 (top-right). Primary plane eps y = 0 (bottom-left). Primary plane eps x = 0 (bottom-right)

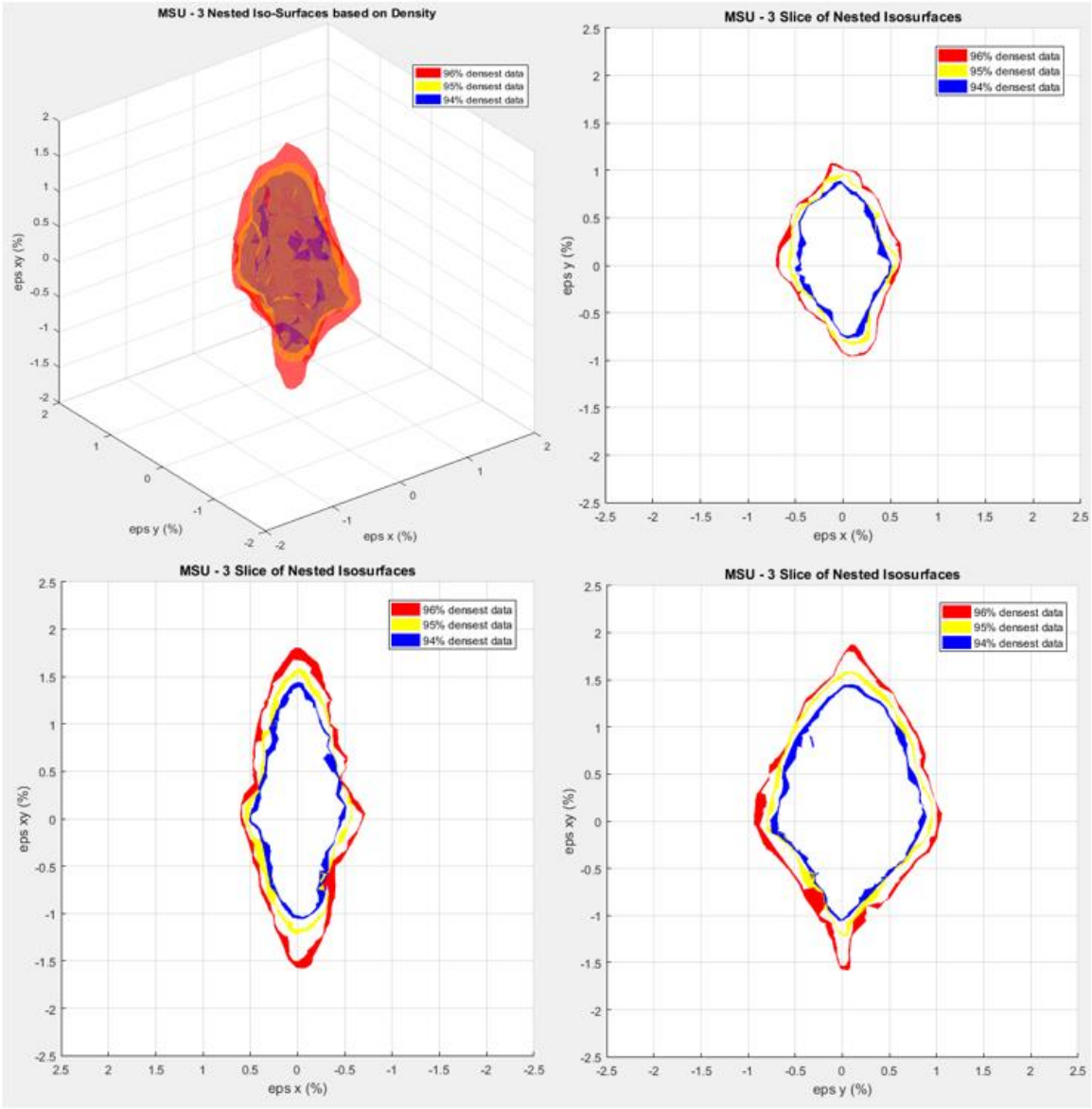

Figure 53. Nested isosurfaces for MSU - 3 displayed on each primary plane. Original nested isosurfaces (top-left). Primary plane eps xy = 0 (top-right). Primary plane eps y = 0 (bottom-left). Primary plane eps x = 0 (bottom-right)

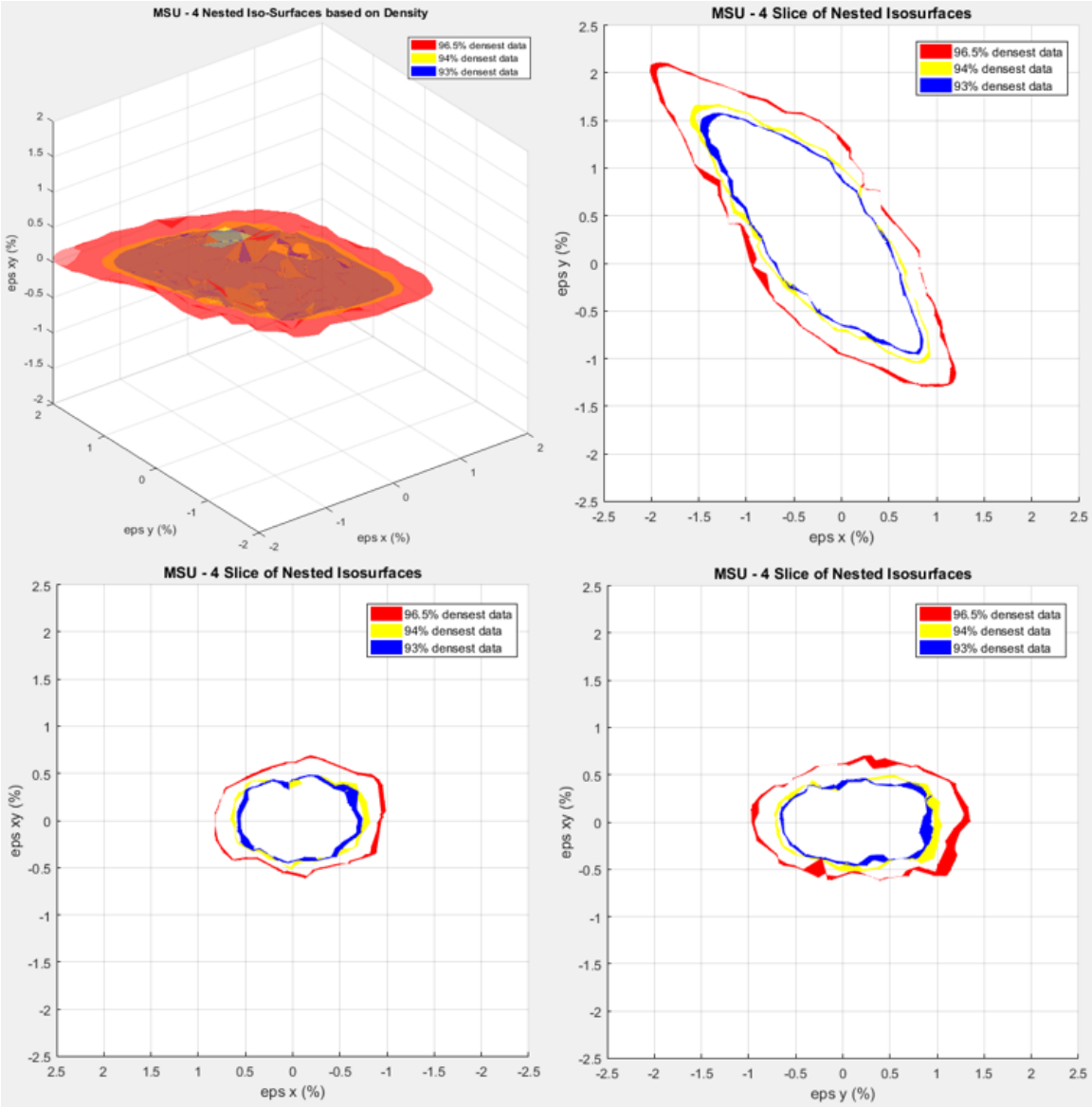

Figure 54. Nested isosurfaces for MSU - 4 displayed on each primary plane. Original nested isosurfaces (top-left). Primary plane eps xy = 0 (top-right). Primary plane eps y = 0 (bottom-left). Primary plane eps x = 0 (bottom-right)

APPENDIX C:

PROGRESSIVE DAMAGE TABLE

Each damage mode in the following tables is determined solely based on ARAMIS calculations such as major strain (maximum principal strain) direction and the observation of failed samples. The data was then interpreted analytically using the finite element model. All damage modes included are only damage modes that could be directly observed from the data. For this reason, some listed failure modes were broad and not specifically defined. Abbreviations for the interpretation of the tables are as follows:

- MC – Matrix Cracking
  - Cracks begin in the matrix, propagates, and leaves fibers intact. Typically observed as the first damage. High strains and maximum principal strain directions provide information regarding this type of damage. Further details into this mode of failure (such as shear or tension) are not easily determined and therefore not included in the resultant tables.
- DL – Delamination
  - Often interpreted from out-of-plane displacements calculated by the DIC. This failure typically causes final failure for tests with large rotation components as fiber failure is observed for these displacements less often.
- FR – Fiber Rupture
  - Fibers incur damage directly causing fiber breakage. Typically, the "last straw" as stored energy suddenly released into the sample causes catastrophic failure.
- Buckle – Buckle Failure
  - Due to compression, typically causes large out-of-plane displacements, delaminations, and even kink-band formation.
- OA – Off Angle Plies
  - All non-zero and non-90 degree plies.
- LNT – Localized at Notch Tip
  - Damage location is confined primarily to the notch tip. If not specified, damage occurs multiple places.
- TG|BG – Top Grip or Bottom Grip
  - Damage is occurring locally at the top grip or bottom grip.

Table 12. Progressive damage table for MSU–11 tests. IM7/8552 Material: [-45/90/45/0]s

Test	Damage initiation			Intermittent Stage			Final Failure		
Name	stage	ply	mode	stage	ply	mode	stage	ply	mode
11_003	101	-45	MC - LNT	128	All	DL	143	0	FR - LNT
11_004	72	90	MC - LNT	84	45	MC - LNT	125	0	FR - LNT
11_005	90	-45	MC - LNT	95	90	MC	107	All	DL
11_006	42	-45	MC - LNT	61	90	MC	153	0	FR - LNT
11_007	58	0	MC	85	-45	MC - LNT	112	All	DL
11_008	62	90	MC - LNT	86	OA	MC - LNT	105	All	DL
11_009	58	45	MC	148	-45	DL	283	All	DL
11_010	80	90	MC - LNT	124	-45	DL	141	All	DL
11_011	72	45	MC - LNT	97	OA	MC - LNT	116	All	DL
11_012	35	90	MC - LNT	77	OA	MC	144	0	FR
11_014	134	90	MC	162	OA	MC	301	All	DL - LNT
11_015	60	90	MC	121	-45	MC - TG	204	All	Buckle
11_016	44	90	MC - LNT	125	OA	MC - LNT	175	0	FR - LNT
11_017	62	90|-45	MC - LNT	124	OA	MC - LNT	179	0	FR - LNT
11_018	104	90	MC	167	90	MC - LNT	220	All	DL - LNT
11_019	98	45	MC	180	OA	MC	208	All	DL
11_020	69	90	MC	163	OA	MC	301	0	FR
11_021	68	90	MC - LNT	145	OA	MC - LNT	212	0	FR - LNT
11_022	56	OA	MC - LNT	100	90	MC - LNT	130	0	FR
11_023	41	90	MC	75	-45	MC - LNT	126	0	FR
11_024	32	90	MC - LNT	56	OA	MC - LNT	154	0	FR - LNT
11_025	63	45	MC - LNT	69	-45	FR	74	All	DL

Table 13. Progressive damage table for MSU–13 tests. IM7/8552 Material: [0/90/0/90]s

Test	Damage initiation			Intermittent Stage			Final Failure		
Name	stage	ply	mode	stage	ply	mode	stage	ply	mode
13_008	105	90	MC - LNT	180	0	MC - LNT	218	0	FR
13_009	86	0	MC - LNT	178	0	FR	234	0	FR - BG
13_010	30	0	MC - LNT	113	0	FR	134	0	FR - TG
13_011	84	0	MC - LNT	116	90	MC	123	0	FR
13_012	18	90	MC - LNT	38	0	MC - LNT			
13_014	54	90	MC - LNT	137	0	MC - LNT	225	0	FR
13_015	41	90	MC	50	90	MC - LNT	63	0	FR - LNT
13_016	14	90	MC - LNT	72	90	MC	129	0	FR - LNT
13_017	44	90	MC	81	All	DL	164	0	FR
13_018	35	All	MC	55	0	FR	71	All	DL
13_019	45	90	MC - BG	69	0	MC - LNT	175	0	FR - BG
13_020	137	90	MC - LNT	159	0	MC - LNT			
13_021	23	90	MC	38	0	MC	73	0	FR - LNT
13_022	22	90	MC - LNT	88	0	MC - LNT	130	0	FR - LNT
13_023	29	0	MC	41	90	MC - LNT			
13_024	20	90	MC - LNT	31	0	MC - LNT	89	0	FR - LNT
13_025	43	0	MC	77	90	MC - LNT	92	0	FR

Table 14. Progressive damage table for MSU–14 tests. IM7/8552 Material: [-45/45/-45/45]s

Test	Damage initiation			Intermittent Stage			Final Failure		
Name	stage	ply	mode	stage	ply	mode	stage	ply	mode
14_010	24	45	MC - LNT	49	-45	MC	81	All	DL
14_011	67	-45	MC - LNT	108	-45	MC	150	45	FR
14_012	19	All	MC - LNT	63	-45	FR - LNT	98	All	DL
14_014	28	-45	MC - LNT	126	-45	MC - BG			
14_015	60	-45	MC - LNT	91	45	MC	126	All	Buckle
14_016	12	-45	MC	17	All	MC	22	All	DL
14_017	44	-45	MC - LNT	57	-45	MC	90	All	DL
14_018	42	-45	MC - LNT	65	45	MC - LNT			
14_019	46	All	MC - LNT	100	All	MC			
14_020	28	All	MC	100	-45	MC	152	All	DL
14_021	41	-45	MC - LNT	81	All	MC	129	All	DL
14_022	51	-45	MC - LNT	154	45	MC	194	All	DL
14_023	58	-45	MC	67	45	MC - LNT	132	All	DL
14_024	30	All	MC	98	All	DL	167	-45	FR
14_025	27	-45	MC	62	OA	MC - LNT	76	All	DL

Table 15. Progressive damage table for MSU–1 tests. Toray Material: [-45/90/45/0]s

Test	Damage initiation			Intermittent Stage			Final Failure		
Name	stage	ply	mode	stage	ply	mode	stage	ply	mode
1_005	53	90	MC	65	OA	MC	112	All	DL
1_006	46	90	MC - LNT	67	OA	MC - LNT	92	0	FR - LNT
1_009	31	90	MC - LNT	60	OA	MC - LNT	90	All	DL
1_010	43	-45	MC - LNT	106	45|90	MC	113	All	DL
1_011	121	90	MC - LNT	182	OA	MC - LNT			
1_012	41	-45	MC	83	All	DL - LNT	178	0	FR - LNT
1_014	175	90	MC - LNT	232	OA	MC - LNT	298	All	DL
1_015	26	90	MC - LNT	46	OA	MC - TG			
1_016	36	90	MC - LNT	117	OA	MC - LNT			
1_017	56	90	MC	70	OA	MC	192	0	FR
1_018	89	90	MC - LNT	111	OA	MC - LNT	124	All	DL - LNT
1_019	31	-45	MC	40	All	DL	290	45	FR
1_020	226	90	MC - LNT	281	OA	MC - LNT			
1_021	34	90	MC - LNT	62	45	MC - LNT	79	0	FR - LNT
1_022	54	90	MC	80	OA	MC	195	All	DL
1_023	63	90	MC - LNT	97	OA	MC	166	0	FR - LNT
1_024	23	90	MC - LNT	55	OA	MC	103	All	DL
1_025	46	90	MC - LNT	62	OA	MC	101	0|45	FR
1_026	58	90	MC - LNT	72	OA	MC	94	0	FR - LNT

Table 16. Progressive damage table for MSU–3 tests. Toray Material: [0/90/0/90]s

Test	Damage initiation			Intermittent Stage			Final Failure		
Name	stage	ply	mode	stage	ply	mode	stage	ply	mode
3_007	32	90	MC	51	All	DL	82	0	FR - LNT
3_008	34	90	MC - LNT	62	0	MC	75	0	FR - LNT
3_009	26	90	MC - LNT	45	0	FR - LNT	68	0	FR
3_010	43	0	MC - LNT	105	90	MC - LNT	147	0	FR
3_011	61	0	MC - LNT	141	90	MC - BG	178	All	DL - LNT
3_012	28	90	MC - LNT	170	90	MC			
3_014	65	90	MC - LNT	100	0	FR - LNT	151	0	FR
3_015	97	90	MC	110	All	DL	122	0	FR
3_016	20	90	MC - LNT	80	All	MC	139	0	FR - LNT
3_017	16	90	MC	160	0	MC - LNT			
3_018	7	All	MC	21	0	FR - LNT	24	0	FR - TG
3_019	65	All	MC	152	All	DL	195	0	FR
3_020	44	90	MC - LNT	140	0	MC - LNT			
3_021	24	90	MC - LNT	62	0	MC - LNT	94	0	FR - LNT
3_022	46	0	MC - LNT	120	90	MC			
3_023	33	0	MC - LNT	127	90	MC			
3_024	24	90	MC - LNT	78	0	MC - LNT	128	0	FR - LNT
3_025	45	All	MC	85	All	DL	107	0	FR

Table 17. Progressive damage table for MSU–4 tests. Toray Material: [-45/45/-45/45]s

Test	Damage initiation			Intermittent Stage			Final Failure		
Name	stage	ply	mode	stage	ply	mode	stage	ply	mode
4_005	48	-45	MC - LNT	151	45	MC	209	All	DL
4_006	16	45	MC - LNT	120	-45	MC - LNT			
4_007	43	-45	MC - LNT	150	45	MC	200	All	DL
4_008	58	45	MC - LNT	148	-45	MC	205	All	DL
4_009	64	-45	MC - LNT	135	All	DL	149	-45	Buckle
4_010	36	45	MC - LNT	87	All	DL	109	-45	FR
4_011	56	-45	MC - BG	108	45	MC	121	All	DL
4_012	9	-45	MC - LNT	57	45	MC - LNT	65	All	DL
4_014	3	45	MC - LNT	114	-45	MC - LNT			
4_015	87	All	MC - LNT	206	All	MC			
4_016	14	All	MC	43	All	DL	59	All	DL
4_017	39	45	MC	88	-45	MC - LNT	136	All	DL
4_018	33	45	MC - LNT	56	45	MC	68	-45	FR
4_019	71	45	MC - LNT	131	All	MC			
4_020	42	All	MC - LNT	150	All	MC	206	All	DL
4_021	47	-45	MC - LNT	79	45	MC - LNT	171	All	DL
4_022	31	All	MC - LNT	184	All	MC			
4_023	30	-45	MC - LNT	121	All	MC	152	All	DL
4_024	40	All	MC - LNT	125	All	MC	173	All	DL
4_025	35	-45	MC - LNT	71	45	MC	110	All	DL